High Fidelity Coherent Pulse Stacking Amplification with Intelligent System Controls

by

Hanzhang Pei

A dissertation submitted in partial fulfillment
of the requirements for the degree of
Doctor of Philosophy
(Electrical and Computer Engineering and Scientific Computing)
in The University of Michigan
2021

Doctoral Committee:

Professor Almantas Galvanauskas, Chair
Professor Igor Jovanovic
Associate Research Scientist John A. Nees
Professor Herbert G. Winful

Hanzhang Pei

hpei@umich.edu

ORCID iD: 0000-0003-1012-0340

Dedicated to my wife Yao

ACKNOWLEDGEMENTS

I would like to thank all the people who have guided, supported and accompanied me during my academic journey at the University of Michigan.

First I would like to thank Professor Galvanauskas. I have been fortunate to be working with such a resourceful and devoted advisor who is always willing to closely engage and work with his students. You have inspired me with your incredibly sharp logic, engaging and top-down storytelling skills, deep passion for research, and family-centric virtues, and you have guided me through some very challenging phases in my research. Thank you for your support throughout my doctoral journey and your open-mindedness on my pursuit of alternative academic and career paths. The invaluable skills I have learned from you will be carried with me.

I would also like to thank my dissertation committee members. Thank you John Nees for constantly bringing in your unique perspectives and inspiring me with your creative ideas. I thank Professor Winful for all the brilliant derivations in your lectures and Professor Jovanovic for your collaboration with our group. Thank you all for your kind support to my dissertation.

My sincere appreciation goes to my current and former colleagues: Mathew Whittlesey, Alexander Rainville, Weizhi Du, Siyun Chen, Yifan Cui, Mingshu Chen, Lauren Cooper, Christopher Pasquale, John Ruppe, Morteza Sheikhsofla, Tong Zhou, Cheng Zhu and I-Ning Hu. Our research projects are so continuous and comprehensive, it wouldn't be possible to accomplish our goals without tremendous team effort, and I am grateful for working among a group of motivated, accountable and

fun researchers.

I would like to thank our collaborators: Russell Wilcox and Qiang Du from Lawrence Berkeley National Lab, Gengji Zhou and Professor Frantz Kärtner from DESY, Professor Zhigang Zhang from Peking University and Professor Henrik Tünnermann from the University of Electro-Communications for bringing your expertise and supporting our work.

I also thank my fellow board members at the Optics Society at the University of Michigan for serving our optics community together. Special thanks to Elizabeth Dreyer for your mentorship, and to my friends Jubilee Adeoye, Dakota Crisp, Kaiwen Guo, Feiran Li and Chunyi Zhao for your companionship. I thank all my friends for your accompany in the past few years.

Finally, deepest thanks to my families. I thank my parents for their unconditional love and support. To my beloved wife Yao, there is a life-long journey ahead of us, and I can't wait to march forward, with you.

TABLE OF CONTENTS

LIST OF FIGURES

Figure

LIST OF TABLES

Table

ABSTRACT

Emerging applications of laser plasma accelerators require next generation laser drivers with multi-kW average power and TW peak power. Our vision for delivering such performance is through the coherent spatial and temporal combining of femtosecond pulse fiber laser arrays. The time domain combining is implemented as coherent pulse stacking amplification (CPSA), where modulated pulses propagate through optical cavities to interfere and stack into a single pulse. This technique extends the energy scaling capabilities of chirped pulse amplification (CPA) by $\sim 10^2$.

This dissertation focuses on developing a high-precision CPSA system with high fidelity in three key aspects. First, stabilization of 81-pulse stacking in 4+4 multiplexed GTI cavities with high efficiency and long-term stability was achieved for the first time. With the collaborative effort, an FPGA-based control system was developed, and following several optical and electronics improvement to reduce system noise level to below theoretical tolerance level, the stochastic parallel gradient descent (SPGD) algorithm was implemented to control cavity phases and stack 81 pulses into a single pulse at $> 70\%$ efficiency and $\sigma_{peak} = 1.4\%$ peak power stability.

Second, theories on high fidelity stacking were developed, and real-time optimization was simulated and experimentally demonstrated. Equivalence of coherent pulse stacking to a deep recurrent neural network was presented. A mathematical description of coherent pulse stacking based on transfer matrices was developed to predict the effects of various errors on stacking performance. High-precision stacking techniques were developed accordingly for reducing alignment and control errors to enable theoretically expected CPSA performance. To compensate for CPSA system uncer-

tainties, adaptive optimization of pulse modulation that improves stacking fidelity over time was designed, simulated, and demonstrated in the experiment.

Last, near-complete stored energy extraction from fiber amplifiers in ultrashort high energy pulses was achieved using the CPSA technique. Extraction of ∼90% stored energy at $> 10mJ$ level at 1kHz from a single large-core Chirally-Coupled-Core (CCC) fiber was accomplished at low nonlinearity, setting record performance for a single-channel femtosecond pulse energy.

To summarize, long term stable and high fidelity coherent stacking of $\sim 10^2$ ultrashort pulses with adaptive optimization and energy scaling capabilities has been achieved. This opens a pathway to the practical implementation of multi-J pulsed systems and further intelligent control capabilities in the future.

CHAPTER I

Introduction

1.1 Background and motivation

As modern technologies of accelerators are being developed to push for higher energy, luminosity, and brightness, one promising contender is laser plasma accelerator (LPA) [1, 2], which could potentially deliver comparably high beam-electron energy as compared to an RF-driven counterpart while being orders of magnitude shorter in length and cheaper to build [3]. A conceptual design for an LPA-based TeV collider is shown in Fig.1.1.

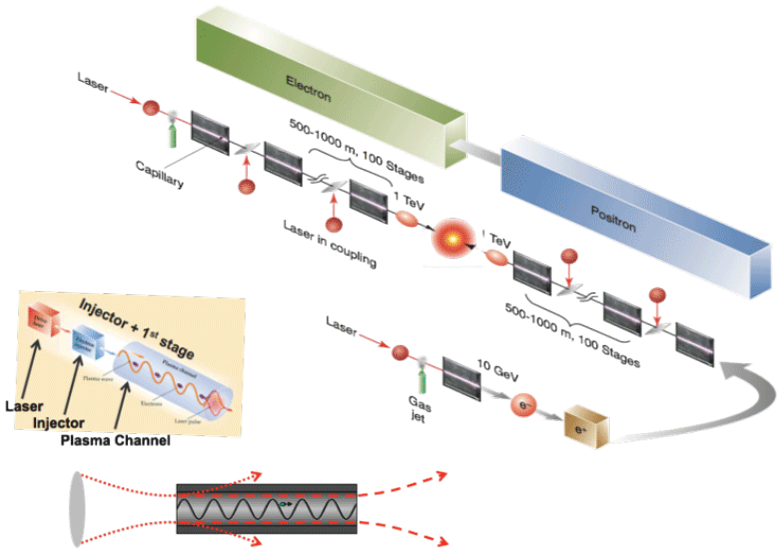

Figure 1.1: Conceptual design of a LPA collider [3].

Laser-plasma interactions can be utilized to drive secondary-radiation sources, including electron acceleration, X-ray [4], gamma-ray generation [5], neutron generation [6], etc, as shown in Fig.1.2. These sources enable numerous applications in medicine and biology, material science, security applications (e.g. active interrogation of nuclear materials) and fundamental science discoveries.

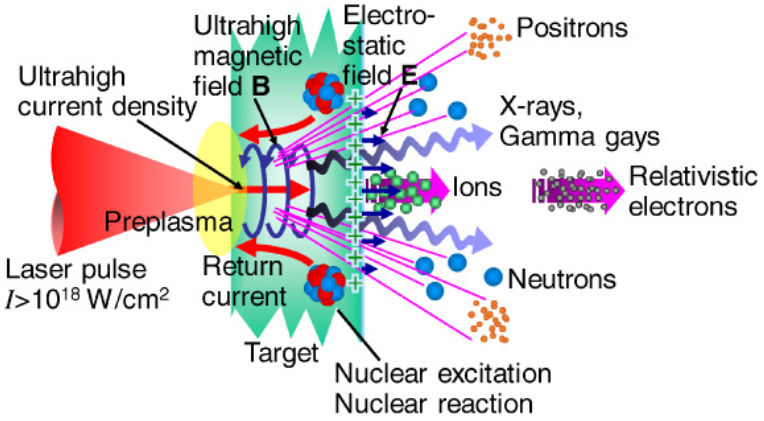

Figure 1.2: Ultra-high intensity laser interacts with a plasma and emits secondary radiation and particles [7].

In an LPA system, a properly shaped ultraintense laser pulse is guided by a confined plasma channel and excites a plasma wave, whose electric field accelerates particles. Emerging applications of LPA require that the next generation laser drivers should perform at multi-tens of TW peak and multi-kW average powers [8]. For example, as current experimental and numerical-simulation evidence suggests, future linear colliders could consist of cascaded 10 GeV LWPA cells, each driven by 6.5J and 100fs pulses at 50 kHz repetition rate (i.e. 355 kW of average power). This is very difficult to achieve with any current solid-state laser technology, particularly since such high-power performance also makes it imperative that these drivers should be very efficient, preferably exceeding 30% wall plug efficiency. It is a significant technological challenge, which calls for developing completely new approaches.

1.2 Coherent spatial and temporal combining

Our vision for delivering such performance for LPA laser drivers is through the coherent spatial and temporal combining of femtosecond pulse fiber laser arrays [9]. Fiber amplifiers bring a few key advantages to this architecture: they generally have high wall-plug efficiency (∼50%), compact monolithic integration, efficient and distributed head dissipation, and diffraction-limited beam output while being cost-effective, scalable and robust. With coherent spatial combining of parallel channels at the end of the power amplifier array, each channel is allowed to produce lower energy as long as the combined energy satisfies system requirement.

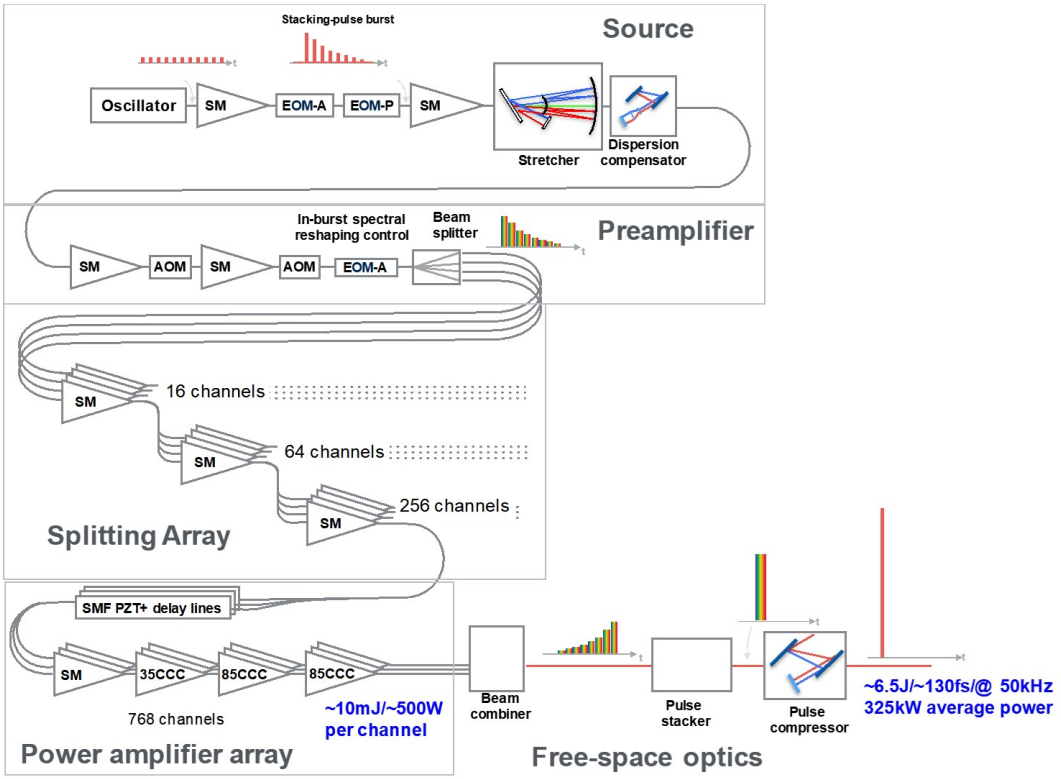

Figure 1.3: An LPA collider driver architecture based on coherent spatial and temporal combining of fiber arrays [9].

Multiple techniques of coherent spatial beam combining of femtosecond pulses have been used or developed. The simplest implementations are with intensity beam combiners that are partially reflective and transmissive [10], which requires accurate

phase control for individual channel. With polarization beam splitters (PBS) or thin-film polarizers (TFP), a beam can split into two beams with opposite polarizations and arbitrary power ratio and vice versa [11, 12, 13]. Using diffractive optical elements (DOE), two-dimensional combination of 8 channels was achieved via output intensity pattern analysis [14, 15]. By configuring parallel channels into tiled aperture and utilizing far field coherent beam recombination, 61 femtosecond fiber amplifiers are combined with a hexagonal micro-lens array [16, 17]. While coherent beam combining fulfills one key aspect of scalability in developing high peak power, high average power laser systems, the other aspect is to deliver as high energy and power per spatial channel as possible.

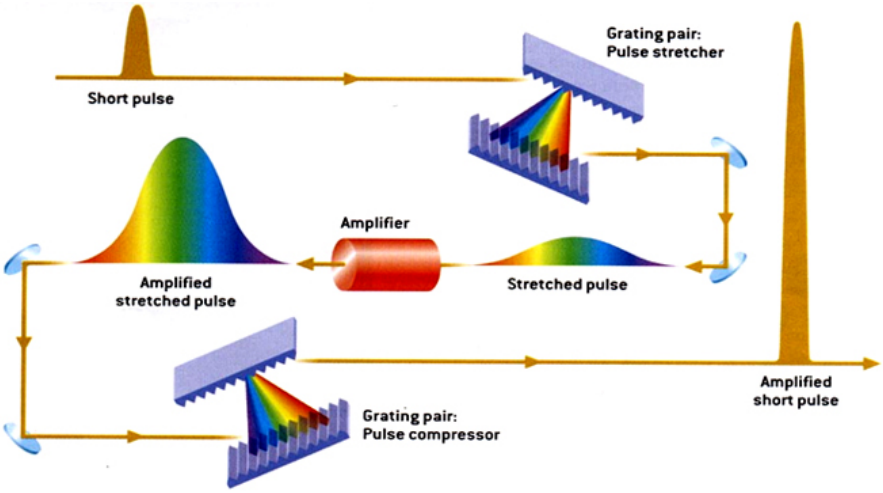

Figure 1.4: Schematic diagram of chirped pulse amplification [18]

Producing high energy pulses in fiber amplifiers requires lowering peak power in the gain medium to avoid accumulation of nonlinearity and material damage. Chirped pulse amplification (CPA) has been a breakthrough technique that reduces pulse peak power by $\sim 10^5$ and correspondingly increases energy by $\sim 10^5$ from pulse stretching [19]. In a solid-state CPA, further $10^1 - 10^2$ energy increase can be achieved through transverse crystal size scaling. In a fiber CPA, however, there is limited transverse aperture scaling, and consequently the achievable energies are $\sim$2 orders of magnitude below stored energy level. As a result of this energy limitation in a single fiber

amplifier, the aforementioned LPA collider driver would require $\sim 10^4 - 10^5$ parallel channels, which challenges the practical implementation of such design.

Therefore the pulse duration in each channel need to be further extended by effectively 2 orders of magnitude to increase per-channel pulse energy by a comparable amount and hence reduce the number of required parallel channels to $\sim 10^2 - 10^3$. This can be achieved via amplifying a series of chirped pulses instead of a single chirped pulse and coherently combine them in the time domain at the spatially combined output, i.e. coherent temporal combining.

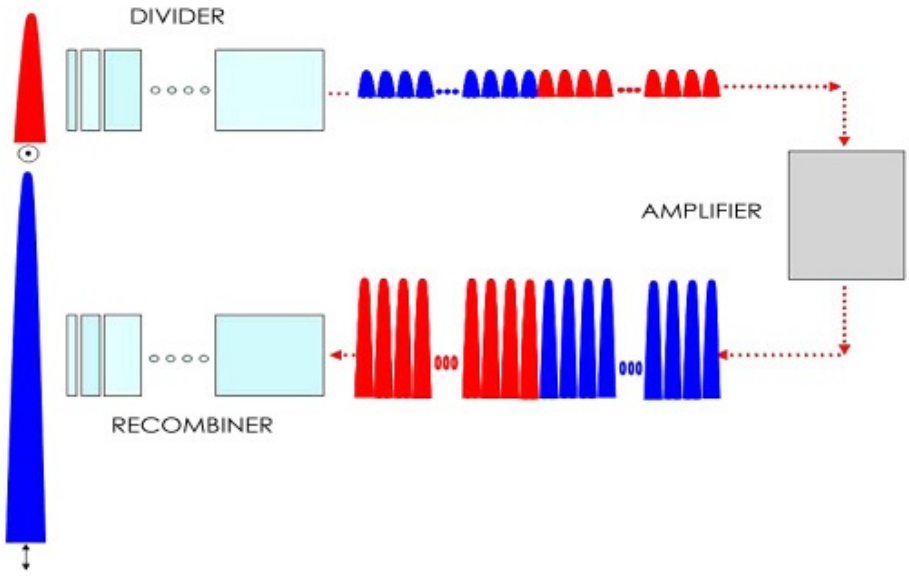

Figure 1.5: Principle operation of divided pulse amplification [20].

Using temporal multiplexing, a burst of pulses in the time domain are amplified together and then stacked back into a single pulse before compression. This allows scaling of the effective pulse duration, so also the pulse energy, by the number of pulses in the burst. Several techniques have been proposed that utilize this time domain multiplexing concept such as divided pulse amplification (DPA) [20], stack and dump [21, 22], and coherent pulse stacking (CPS) [23].

The DPA technique first divides an initial pulse longitudinally into a sequence of lower-energy pulses that are otherwise identical to the original, except for the

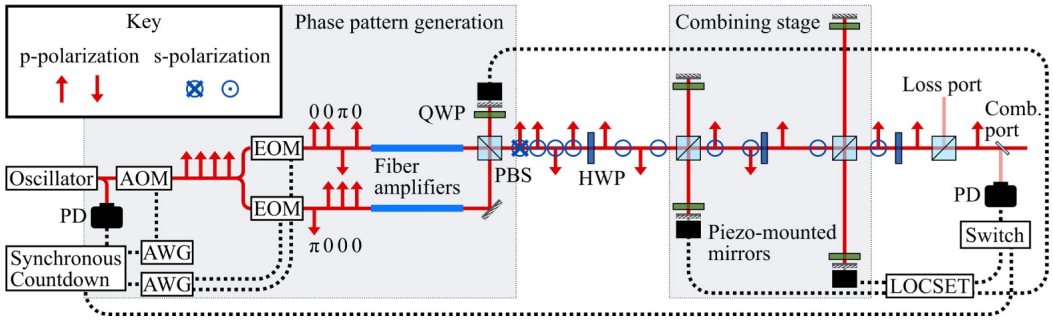

Figure 1.6: Schematic illustration of electro-optically controlled divided pulse amplification [12].

polarization. The low-intensity pulses are then amplified and recombined to create a single intense pulse, as shown in Fig. 1.5. The alternating light and dark colors refer to the two perpendicular polarizations, and the crystals are aligned in such a way that the optical axes of neighbor crystals are rotated 45° about the direction of propagation. The final combined output pulse has its polarization perpendicular to the input polarization. Currently DPA has only been demonstrated with up to 8 total pulse replicas due to a limited number of degrees of freedom in the splitting stages [20, 12].

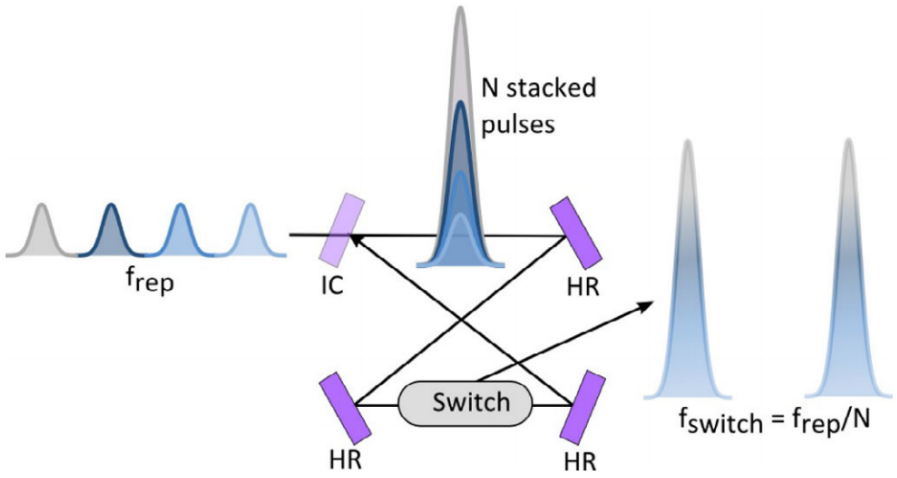

Figure 1.7: Principle operation of stack and dump enhancement cavity [22].

Stack and dump utilizes a passive enhancement cavity to stack a pulse train emitted from a high repetition rate femtosecond laser system, as shown in Fig. 1.7. It

requires a fast, purely reflective switching element that allows for the dumping of the enhanced pulse out of the cavity. The primary limitation on stack and dump is that when scaling to high pulse energies, transmissive optical switches such as electro-optic and acousto-optic modulators will distort the beam and intra-cavity pulse upon successive roundtrips due to nonlinearities in these devices (assuming damage thresholds are not reached first). A reflective optical switch would be necessary for this technique to be scalable to large pulse energies, but such a device does not exist at the present time to the best of our knowledge.

The technique we are developing is coherent pulse stacking (CPS) [23], which bypasses the limitations imposed by both DPA and stack and dump and can allow for large enhancement factors with large pulse energies. Coherent pulse stacking is a two-step process that starts by amplitude and phase modulating a burst of pulses directly from a femtosecond pulse source, e.g. a mode-locked oscillator. The modulations are chosen so that after amplification, this burst of pulses can be temporally stacked into a single pulse by using a sequence of Gires-Tournois interferometers (GTIs) [24]. Owing to the lack of a splitting stage and the resonant cavity nature of the GTIs, this technique is more compact than DPA while maintaining scalability to arbitrarily large numbers of pulses and large pulse energies with no active intra-cavity elements.

1.3 Coherent pulse stacking amplification

Our implementation of time domain combining is coherent pulse stacking amplification (CPSA), where modulated pulses propagate through optical cavities to interfere and stack into a single pulse. It consists of the following key steps: pulse burst formation, chirped pulse amplification, and coherent pulse stacking and compression. Femtosecond pulses generated from a pulse source, e.g. a mode-locked oscillator, are sent through amplitude and phase EOMs to be carved into bursts of modulated pulses. The bursts of pulses are stretched to pulsewidths comparable to

pulse separation such that these pulses overlap into each other, forming an effectively long pulse, then propagates through serial fiber amplifiers to boost pulse burst energy. The amplified pulse burst then propagates through a set of Gire-Tournois interferometers (GTIs) where pulses interfere and coherently stack into a single pulse, and is compressed to femtosecond pulsewidth, as illustrated in Fig. 1.8.

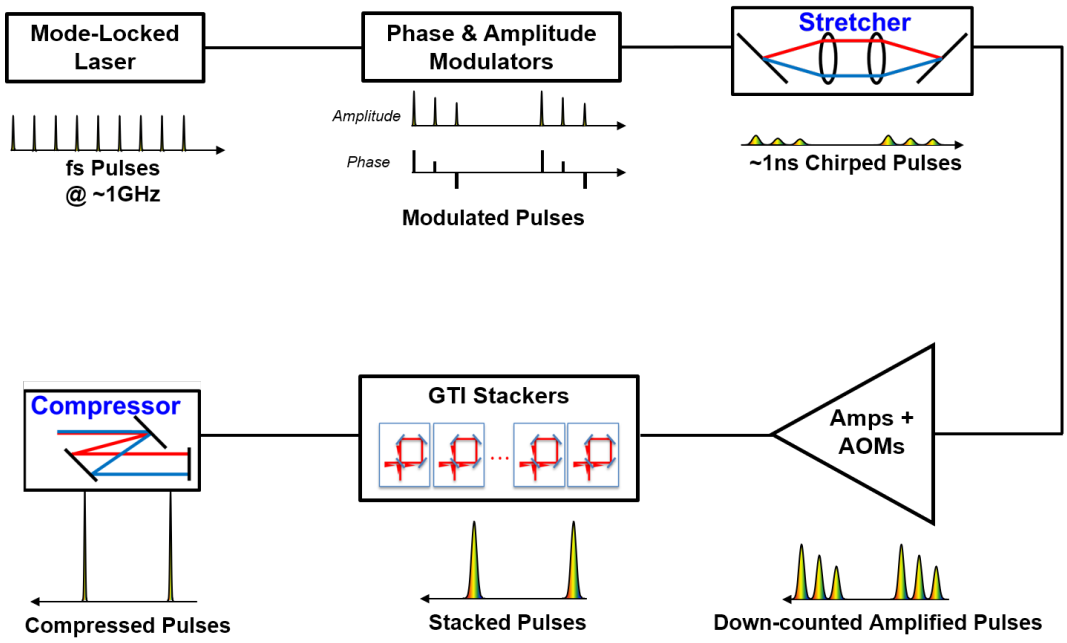

Figure 1.8: Schematic diagram of coherent pulse stacking amplification

CPSA has a few major advantages over other existing temporal combining solutions in scalability, flexibility and energy tolerance. We will show later in the dissertation that CPSA can coherently combine $10^2 - 10^3$ pulses into a single pulse with just $\sim 10^1$ multiplexed optical cavities, and the design of the cavities are so flexible that high efficiency combining can be obtained even without precisely prescribing parameters like cavity front mirror partial reflectivities up front. Because the only temporal combine element is partial-reflecting mirrors and there is no other medium or optical devices involved, the beam otherwise propagates in free space and reflects off of full-reflecting mirrors in the combiner, which increases the energy tolerance to J-level. We will also show later in this dissertation that large number of combinable

pulses further enables high efficiency energy extraction in power amplifier arrays.

1.4 CPSA fully enables fiber array based LPA driver

Since laser wakefield acceleration requires ultrashort, ultraintense laser pulses with high pre-pulse contrast to avoid the formation of plasma by the prepulse [25], certain requirements must be met by the laser driver system. A non-exhaustive issue tree that explores the implications of ultrashort, ultraintense, high contrast laser pulses and their posed system requirements is shown in Fig. 1.9.

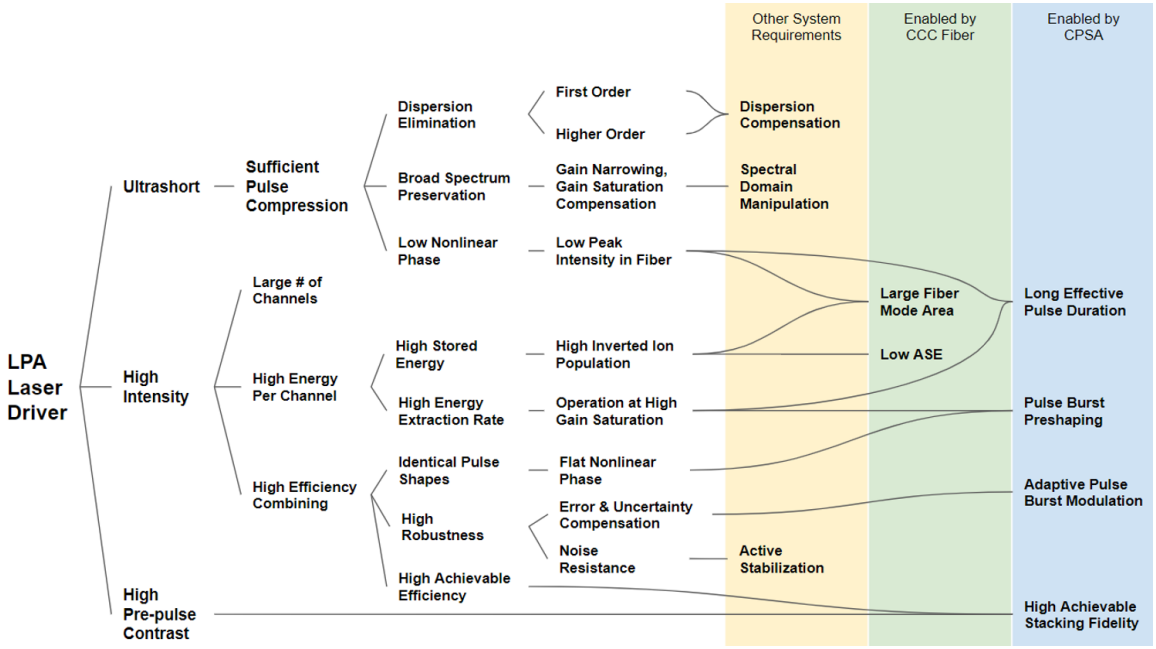

Figure 1.9: A non-exhaustive issue tree of system requirements for a fiber array-based LPA laser driver.

First, to obtain an ultrashort pulse at the end via pulse compression, the system should compensate for higher orders of dispersion, preserve wide spectral bandwidth and accumulate low nonlinear phase. This requires spectral-domain manipulation to compensate for gain narrowing and saturation effects in the amplifiers and higher order dispersion in the system, as well as effectively extending the pulse duration in the fiber amplifiers to reduce peak intensity and hence nonlinear phase. Since CPSA

technique amplifies a burst of pulses that are stretched such that they overlap into each other, they form an effectively long pulse $\sim 10^2 - 10^3$ longer than that achievable with a reasonable size grating using just CPA [19], thus low peak intensity in the gain medium is possible even at high energies.

Second, to achieve high peak power, the pulses need to be sufficiently amplified and coherently combined to a single pulse with high efficiency. With a pulse burst, high extraction rates of stored energy in the fiber amplifiers can be achieved, but the energy scaling also involves significant saturation effect that must be compensated to maintain the effectively long pulse duration. Since the temporal combining of the amplified pulses is achieved through interference, to obtain high visibility constructive and destructive interference, the pulses need to have the same temporal and spectral shape, which requires a flat nonlinear phase distribution across the burst to ensure identical pulse shapes. This requires the CPSA system to carefully modulate the pulse burst amplitudes up front to specifically adapt to the fiber amplifier conditions and provide equal nonlinear phases at the output.

Now that we have discussed how the CPSA system can produce a burst of high energy pulses with the same shape, what remains to be achieved is the coherently combining of these pulses to a single pulse while maintaining a high pre-pulse contrast. This needs to be proven to be theoretically possible and practically feasible in CPSA, and we will discuss in greater detail later in this thesis.

CHAPTER II

Principle and Stabilization of Coherent Pulse Stacking Amplification

2.1 Introduction and background

Fiber laser systems have proven to be capable of producing high quality output beams with very high average power (>1kW); however, obtaining optical pulses with high peak power (>1TW) has proven challenging. The peak power limitations occur due to nonlinear effects that build up during propagation through the fiber since the relatively small mode area ($\sim 2000 \mu m^2$ for flexible fibers) causes the peak intensity to be quite large. The chirped pulse amplification (CPA) technique [19] can allow for a substantial increase in the extractable pulse energy, and therefore also the peak power, by stretching the optical pulses in the time domain by a factor of $\sim 10^4$ so as to reduce the peak power in the fiber amplifier by a similar factor, thus leading to a similar increase in the pulse energy. However, practical size limitations on grating based pulse stretchers and compressors limit the stretched pulse duration to ~1ns, which correspondingly limits the pulse energy to $\sim 100 \mu J$ for these flexible fibers. However, this is only a small fraction of the total energy stored in these fibers, which has been shown to be >10mJ [26]. The only issue is that in order to extract all this stored energy solely using grating based stretchers and compressors would require

stretching the pulses to ∼100ns, thus requiring impractical diffraction gratings that are ∼10m long.

In this chapter we report a demonstration of coherent pulse stacking utilizing a sequence of 4 + 4 multiplexing GTIs which enables a burst of 81 equal amplitude pulses to be stacked into a single output pulse. We also report stabilization of these 4 + 4 GTIs based on the stochastic parallel gradient descent (SPGD) method [27].

2.2 Principle of Operation for Coherent Pulse Stacking Amplification

The coherent pulse stacking amplification (CPSA) technique is a two-step process designed to extend CPA-provided stretched pulse durations by orders of magnitude. This is accomplished by amplifying a burst of modulated and stretched pulses in an amplifier chain and then temporally stacking those pulses after amplification, thus reducing the peak power in the amplifiers proportional to the number of pulses in the burst. First, a burst of amplitude and phase-modulated pulses is pre-shaped from a femtosecond pulse source using fast electro-optic modulators, which yields the ideal pulse burst for stacking after amplification, with any saturation effects being pre-compensated for by the modulators. Then, the amplified pulses in this burst stack into an effectively single output pulse using a sequence of GTIs, which are optical interference cavities compactly arranged in free space and thus can handle the large peak powers that will be achieved.

The quality of stacking, or stacking fidelity, can be characterized by stacking efficiency and pre-pulse contrast. In this dissertation, stacking efficiency is defined as the ratio of stacked pulse energy to pulse burst energy at and before the stacked pulse $\eta_{stacking} = E_{stacked}/(E_{stacked} + E_{pre-pulse})$. Pre-pulse contrast is defined both in terms of ratio in peak power $\chi_{peak} = P_{pre-pulse}/P_{stacked}$ and in terms of ratio to leaked

energy $\chi_{energy} = E_{pre-pulse}/E_{stacked}$ in Fig. 2.1.

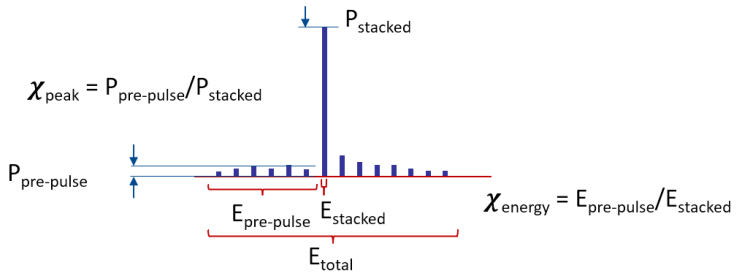

Figure 2.1: Definition of pre-pulse contrast in terms of peak power and energy [9].

The free space pulse stacking arrangement consists of a sequence of Gires-Tournois Interferometers (GTIs), in which the incident pulse burst is coherently combined in the time domain into a single output pulse containing all the energy of the incident burst. For this to happen it is necessary that the roundtrip length of each GTI is either equal to the laser oscillator roundtrip length or is an integer times longer. Furthermore, each GTI in the sequence is characterized by its front mirror reflectivity R and its roundtrip phase ϕ, defined as a fractional wavelength difference (in radians) between the exact GTI roundtrip length and the laser oscillator roundtrip length. Therefore, an m-GTI stacker arrangement is characterized by 2m parameters, permitting the selection of these parameters such that the arrangement would stack 2m equal amplitude pulses in the incident burst. To ensure stable coherent pulse combining in the time domain, it is necessary to actively stabilize the prescribed cavity roundtrip phases due to random perturbations occurring in the system and the environment.

2.2.1 Coherent pulse stacking in equal-length GTI cavities

First, let's consider coherent pulse stacking in a single GTI cavity with front mirror partial reflectivity of R_{front} and cavity roundtrip phase ϕ_{cav}. A single pulse input gives a "ring-down" output pulse train, each pulse with certain amplitudes and phases, where the GTI cavity amplitude response (for the first two pulses) is defined

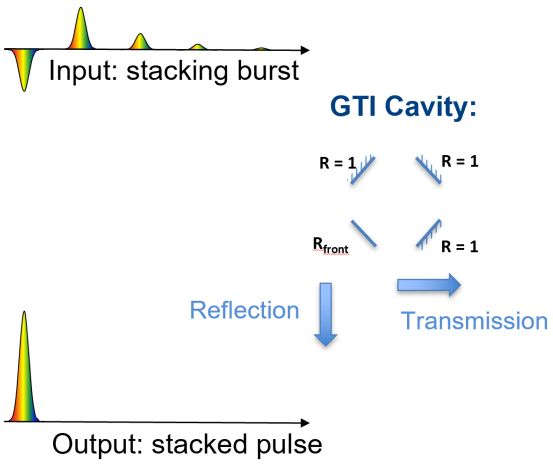

Figure 2.2: Reverse impulse response of a single GTI cavity [9]

by R_{front}, and their relative phases are determined by the cavity phase ϕ_{cav}. Assuming no loss, this impulse response is reversible such that the reversed output pulses form a pulse train that stacks into a single pulse, defined as a stacking sequence. The stacking sequence of a single GTI satisfies $L_{sep} = L_{cav}$, where L_{sep} is the stacking sequence pulse separation, and L_{cav} is the GTI cavity roundtrip length.

Now consider coherent pulse stacking in m equal-length GTIs, with the input pulse train satisfying $L_{sep} = L_{cav}$ for each cavity, as shown in Fig. 2.3. It has been established that a multi–GTI stacker arrangement is a linear time-invariant (LTI) system[28]. Therefore, as it is well known from the LTI system theory [29], the GTI stacker output can be calculated for any input train using the system's impulse response function. Since the input pulses are identically shaped and equally spaced, it is most convenient to define this LTI system as a discrete-time system, which allows us to define an individual pulse with complex amplitudes denoted as $Ae^{i\phi}$, with A and ϕ denoting the electric field amplitude and phase respectively.

The impulse response of a discrete-time system is defined as the system's response to a single unit-amplitude incident pulse [29]. For a properly designed m-GTI stacker this impulse response consists of a sequence of 2m equal amplitude pulses and a rapidly decaying pulse-burst tail. An ideal loss-free stacker should be completely reversible.

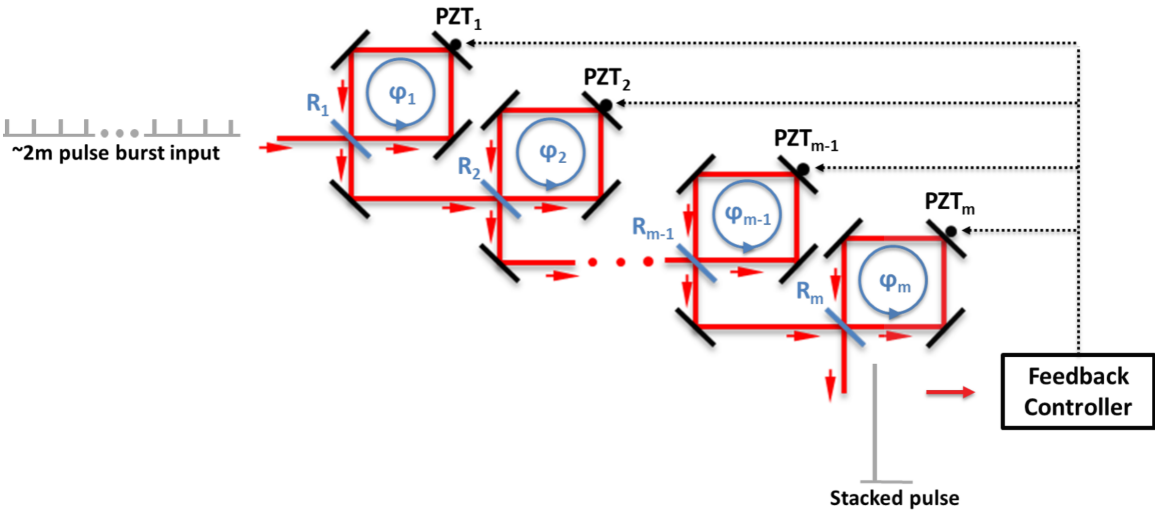

Figure 2.3: m-GTI sequential cascade with representing the set of m front mirror reflectivities, and representing the set of m roundtrip phases. The cavity roundtrip phases are controlled using a feedback system that adjusts the roundtrip phase by applying a voltage to the corresponding PZT mirror [28].

Therefore, the pulse-order reversed and complex conjugated m-GTI stacker impulse response function represents the ideal stacking pulse sequence for producing a single time-combined output pulse. Since in real stackers some losses are unavoidable due to the finite reflectivity of the high reflectivity mirrors in each GTI cavity, this is only approximately true, and the actual stacking-burst sequence needs to be "tuned-up" to account for the actual losses.

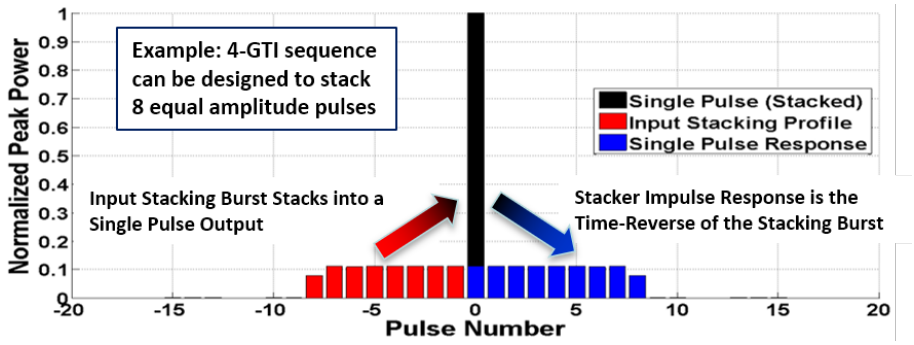

Figure 2.4: A sequence of N equal-length GTI cavities can stack 2N pulses with precisely prescribed amplitudes. Input peak power profile (red) being stacked into a single pulse (black) using the sequence of 4 GTIs with mirror reflectivities and phases shown inset. Also shown is the single pulse response of that system (blue), so these GTIs represent a linear system with time reversal symmetry [28].

The typical design procedure for an m-GTI stacker is a search for a set of m reflectivities and m round-trip phases, which produces the desired system's impulse response function with the first 2m pulses (approximately) equal. The simulated example in Fig. 2.3 shows a specific design of a 4-GTI sequence, which can stack an incident burst containing 8 equal amplitude pulses. This is not a unique design, and multiple design options for each m-GTI sequence with m>1 are possible.

2.2.2 Coherent pulse stacking in multiplexed GTI cavities

It has been established so far that a sequence of N equal-length GTI cavities with $L_{cav} = L_{sep}$ can stack 2N pulses with precisely prescribed amplitudes. When the stacking sequence is sufficiently long, the implementation of equal-length cavity design faces scalability challenges. A multiplexed GTI cavity set, which involves GTI cavities with roundtrip length $L_{cav} = lL_{sep}$ where $l \geq 1$ is an integer defined as multiplexing factor, can be configured to stack 2N pulses with approximately prescribed amplitudes with $M << N$ multiplexed-length GTIs. An example of multiplexed GTI design with 4 sets of $l = 1$ GTIs and 4 sets of $l = 9$ GTIs in shown in Fig. 2.5, where the 81 pulses first stack into 9 pulses through 4 sets of $l = 1$ cavities and then into a single pulse through 4 sets of $l = 9$ cavities.

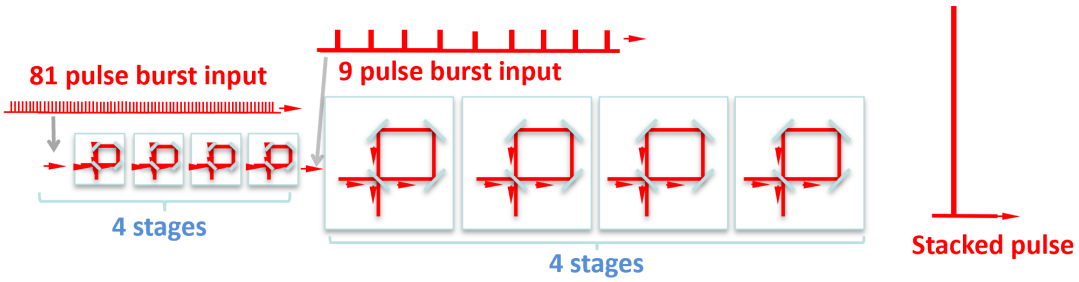

Figure 2.5: Example of a multiplexed 4+4 GTI cavity set stacking 81 pulses first into 9 pulses then into a single pulse [9].

A multiplexed configuration can significantly reduce the number of required cav-

ities, where a sequence of $M << N$ multiplexed-length GTIs can stack 2N pulses, at the cost of approximating the prescribed amplitudes due to reduced degrees of freedom, as shown in Fig. 2.6. It has also been established in previous work that the the total roundtrip length of all GTI cavities combined should equal to half of stacking sequence length, and a GTI cavity with multiplexing factor $l = k$ can be reduced to k equal-length GTI cavities each with multiplexing factor of $l = 1$ [28]. In later sections, we will show that extending the length of stacking sequence can compensate for the lack of degrees of freedom and yield an accurate and smooth profile while only sacrificing a few percent of stacking efficiency.

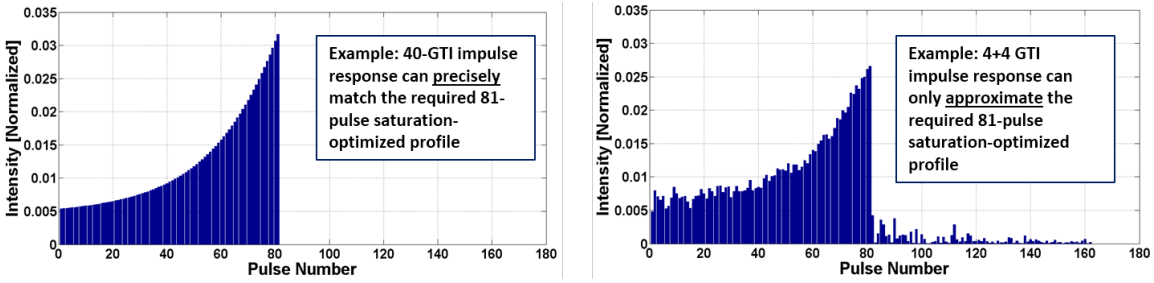

Figure 2.6: A sequence of M << N multiplexed-length (e.g. k+k+..., k+m+n+..., etc.) GTI cavities can stack 2N pulses with approximately prescribed amplitudes. 81-pulse stacking profile produced by (Left) 40 equal-amplitude GTIs and (Right) 4+4 multiplexed GTIs [28].

Since cavity phases, mirror reflectivities and multiplexed lengths are all variables, CPSA features a wide range flexibility in stacker and stacking designs, with a continuum of possible design solutions. Nearly every configuration essentially works, with the only differences between different designs being the achievable stacking efficiency and in contrast. Therefore, the design objective is to maximize contrast, while also maximizing stacking efficiency for a given (and smooth) stacking profile. The ultimate design target would be 40-60dB pre-pulse contrast and ~97-99% stacking efficiency. This flexibility is critical for practical implementation of the CPSA technique, as it allows to accommodate large fabrication tolerances (e.g. mirror reflectivity inaccuracies) and other system uncertainties in amplitude and phase modulation and in

amplifiers.

To summarize, coherent pulse stacking was enabled by two key discoveries. First, a sequence of N equal-length GTI cavities can stack 2N pulses with precisely prescribed amplitudes, as shown in Fig. 2.4. Second, a sequence of M << N multiplexed-length (e.g. k+k+..., k+m+n+..., etc.) GTI cavities can stack 2N pulses with approximately prescribed amplitudes, as shown in Fig. 2.6. Due to lack of degrees of freedom, a set of M << N GTI cavities does not have an impulse response that matches precisely with a saturation-optimized pulse burst shape, but this gives potential for pulse number scalability given a limited number of GTI cavities, which will be covered later in this chapter.

2.3 Noise tolerances in coherent pulse stacking

As presented in the previous section, coherent pulse stacking can be achieved with a set of GTI cavities with cascading and multiplexed cavity configuration. In practice, errors and noises in cavity phases, pulse phases, and pulse intensities affect stacking fidelity, and noise tolerances in stacking shall be analyzed.

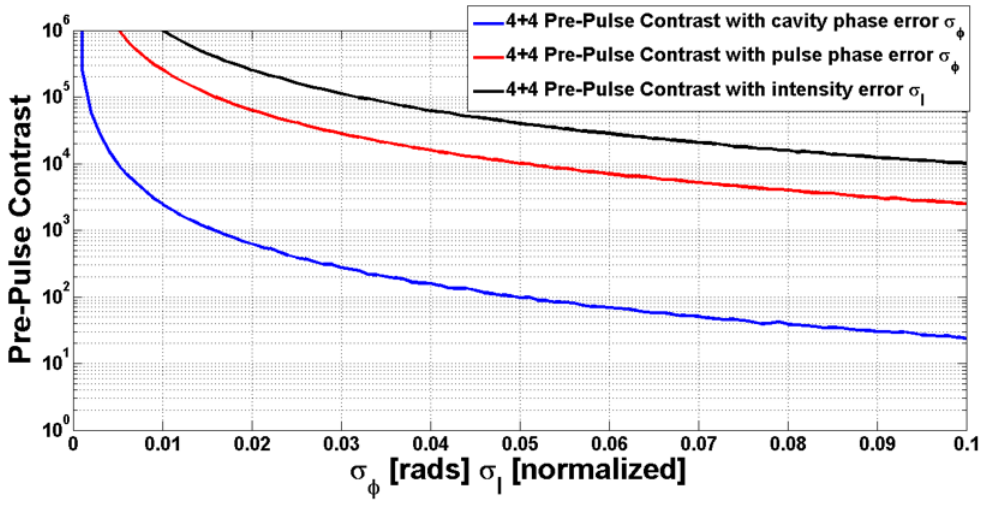

Figure 2.7: Simulations illustrating the tolerances of the coherent pulse stacking parameters for 4+4 GTIs. Achievable pre-pulse contrast degrades in the presence of cavity phase errors, pulse phase errors, or pulse intensity errors [28].

Analysis on the tolerances on these stacking parameters in stacking of N pulses in a 4+4 cascaded and multiplexed GTI set has been established [28]. The errors were simulated by making Gaussian random perturbation with zero mean and a specified standard deviation (σ_ϕ for the cavity phases and pulse phases and σ_I for the pulse intensities). Either all the cavity phases, all the pulse phases, or all the pulse intensities were perturbed using these Gaussian perturbations and averaged over 10,000 samples of the pre-pulse contrast, as depicted in Fig.2.7.

These results indicate that the primary bottleneck in achieving a high fidelity coherent pulse stacking result is cavity phase error, which deteriorates pre-pulse contrast 2 orders of magnitude more than either pulse phase error or intensity error at the same absolute error values. As a typical example, for a pre-pulse contrast of $40dB$, cavity phase must be accurate within $4mrad$, while pulse phases are not nearly as sensitive and only need to be accurate within $50mrad$ to achieve a similar level of performance; the errors in pulse intensities have the least impact on the stacking performance and only need to be accurate within $100mrad$.

2.4 Cavity stabilization Using SPGD

Due to the presence of perturbations and drifting in the system, both the cavities and the pulse train are constantly perturbed, modifying cavity phase and pulse phase values, thus active stabilization is required to maintain coherent pulse stacking.

First we derive the cavity stabilization requirement to achieve steady stacking and interference at the output, in an $l = 1$ non-multiplexed cavity setting. Assuming all input pulses are defined by their amplitudes and phases and are otherwise identical, the input pulse train can be expressed as

$$P_n^{in}(t) = A_n^{in} p(t - nT_R) e^{i(\omega_c t + n\Delta\phi_{CEO})} \tag{2.1}$$

where A_n^{in} is the complex electric field amplitude, $p(t)$ is the pulse envelope, T_R is the pulse period, ω_c is the carrier frequency, and $\Delta\phi_{CEO}$ is the carrier envelope offset phase. For a noise-free GTI cavity, its impulse response is $(H_0, H_1, \cdots)$ where $H_0 = r$ and $H_k = -r^k(1/r - 1)e^{ik\phi_{GTI}}\alpha^k$ for $k \geq 1$. Here r denotes front mirror electric field reflectivity, ϕ_{GTI} denotes cavity phase, and α is cavity roundtrip loss. The derivation of GTI cavity impulse response and GTI-pulse train interaction will be given in the next chapter. Assuming identical pulse envelopes, The m-th output pulse is given by

$$\begin{aligned} E_m^{out} &= H_m E_0^{in} + H_{m-1} E_1^{in} + \cdots + H_{m-k} E_k^{in} + \cdots + H_0 E_m^{in} \\ &= \sum_{k=0}^{m} -r^{m-k}(1/r - 1)\alpha^{m-k} A_k^{in} e^{i((m-k)\phi_{GTI} + k\Delta\phi_{CEO})} e^{i\omega_c t} \\ &= A_m e^{c_1(\phi_{GTI} + c_2\Delta\phi_{CEO})} e^{i\omega_c t} \end{aligned}$$

where the phase term $c_1(\phi_{GTI} + c_2\Delta\phi_{CEO})$ must remain constant to maintain interference relation and hence stacking, where c_1, c_2 are constants determined by the cavity and pulse burst configuration. Hence the steady-phase requirement is

$$\phi_{GTI} + c_2\Delta\phi_{CEO} = const. \tag{2.2}$$

In the presence of phase noise and active phase control, the cavity phase

$$\phi_{GTI} = \phi_{GTI_0} + \Delta\phi_{GTI}(t) + d\phi_{control}(t) \tag{2.3}$$

consists of three terms: initial cavity phase ϕ_{GTI_0}, cavity phase drift $\Delta\phi_{GTI}(t)$ and cavity phase adjustment from PZT control $d\phi_{control}(t)$; the pulse source phase

$$\Delta\phi_{pulse} = \Delta\phi_{CEO} + \Delta\phi_{source}(t) \tag{2.4}$$

consists of two terms: initial carrier envelope offset phase $\Delta\phi_{CEO}$ and pulse source

phase noise $\Delta\phi_{source}(t)$. Plugging in Eq.2.3 and Eq.2.4 into Eq.2.2 gives:

$$\phi_{GTI_0} + \Delta\phi_{GTI}(t) + d\phi_{control}(t) + c_2(\Delta\phi_{CEO} + \Delta\phi_{source}(t)) = const. \tag{2.5}$$

Since cavity phase control is achieved via PZT mirrors, their response speed is physically limited to $\sim 1kHz$ due to intrinsic PZT properties and mass loads on the mirror mount. Therefore for further derivation, we break down cavity phase control into two terms:

$$d\phi_{control}(t) = d\phi_{control-slow}(t) + d\phi_{control-fast}(t) \tag{2.6}$$

where the slow term $d\phi_{control-slow}(t)$ and the fast term $d\phi_{control-fast}(t)$ is defined with above or below the control speed limit. Assuming that pulse source phase noise $\Delta\phi_{source}(t)$ varies at $>$ 1kHz and cannot be fully compensated via PZT adjustments, while cavity phase drift and carrier envelope phase varies at $<<$ 1kHz speed which is within the PZT control speed bandwidth, we further assume that they can be fully compensated by the slow cavity phase control term, i.e.

$$\phi_{GTI_0} + \Delta\phi_{GTI}(t) + d\phi_{control-slow}(t) + c_2\Delta\phi_{CEO} = const. \tag{2.7}$$

can be satisfied. Subtracting Eq.2.7 from Eq.2.5 gives:

$$d\phi_{control-fast}(t) + c_2\Delta\phi_{source}(t) = const. \tag{2.8}$$

which is the stabilization condition that cannot be fully satisfied, yielding stabilization noise to pulse stacking.

For an $l-$multiplexed GTI, its impulse response is given by$(H_0, 0, \cdots, 0, H_1, 0, \cdots)$ with $l-1$ zeros between non-zero elements (derivation given in the next chapter),

hence the output pulse is expressed as:

$$\begin{aligned} E_m^{out} &= H_m E_0^{in} + H_{m-1} E_l^{in} + \cdots + H_{m-k} E_{kl}^{in} + \cdots + H_0 E_{ml}^{in} \\ &= \sum_{k=0}^{m} -r^{m-k}(1/r-1)\alpha^{m-k} A_{kl}^{in} e^{i((m-k)\phi_{GTI}+kl\Delta\phi_{CEO})} e^{i\omega_c t} \\ &= A_m e^{c_1(\phi_{GTI}+c_2 l\Delta\phi_{CEO})} e^{i\omega_c t} \end{aligned}$$

Following the same derivation above, we can obtain stabilization for an l-multiplexed GTI cavity:

$$d\phi_{control-fast}(t) + c_2 l\Delta\phi_{source}(t) = const. \tag{2.9}$$

The stabilization requirement shows that the noise sensitivity grows linearly with GTI cavity multiplexing factor, i.e. cavity length. In order for the coherent pulse stacking method to work robustly, the above stabilization condition must be met in all GTI cavities, in other words, the cavity phases of the GTIs must be accurate to within a small fraction of 2π and compensate for the fast pulse source noise, in our particular example oscillator phase noise.

In order to achieve this, we implemented a stabilization scheme based on the stochastic parallel gradient descent (SPGD) method [27]. Also since the SPGD method is based on local optimization, we need to ensure that the GTI cavity phases are relatively close to the optimized point before the SPGD algorithm is run. This is accomplished using a Lissajous search over the multi-dimensional space comprised of the cavity roundtrip phases, as shown in Fig. 2.8. To achieve stabilization we also need a metric function that is dependent on the cavity roundtrip phases, so we chose to use a time integrated second harmonic signal which is defined as $J_{SHG} = \int_0^T I(t)^2 dt$, where T is a time sufficiently long to include all the necessary post pulses from the cavity ring down, and $I(t) = A^2(t)$ is the output intensity from the sequence of cascaded GTIs. Assuming identical intensity envelope function of each of the output

pulses, which is experimentally valid when the propagation of a pulse one roundtrip through a GTI produces negligible distortions, but needs to be revisited once gain saturation effect kicks in and changes pulse shape across the burst, this equation can be put into discrete time form, and the second harmonic signal can be written as $J_{SHG} = \int_0^T I(t)^2 dt = \sum_{n=0}^{N} CI[n]^2$, where I[n] is the peak intensity of the nth output pulse and C is a constant that can be set to 1 without loss of generality. Using this metric function, we define our Lissajous scan − SPGD algorithm as follows:

Algorithm 1: Lissajous scan and SPGD algorithm for CPSA stabilization

specify perturbation depth d, gain g, tolerance tol;

repeat

  run Lissajous scan on cavity phases ${}^{i}\vec{\delta}_{Lissajous}$;

  measure peak power $J({}^{i}\vec{\delta}_{Lissajous})$;

until *full round complete*;

record $J^{max} = max_i[J({}^{i}\vec{\delta}_{Lissajous})]$;

repeat

  run Lissajous scan on cavity phases ${}^{i}\vec{\delta}_{Lissajous}$;

  measure peak power $J({}^{i}\vec{\delta}_{Lissajous})$;

until $J({}^{i}\vec{\delta}_{Lissajous}) \geq tol * J^{max}$;

initialize cavity phases ${}^{0}\vec{\delta} = {}^{i}\vec{\delta}_{Lissajous}$;

repeat

  measure peak power $J({}^{n}\vec{\delta})$;

  perturb cavity phases randomly by ${}^{n}\Delta\vec{\delta} = \Delta\delta_{random} d$;

  measure peak power $J({}^{n}\vec{\delta} + {}^{n}\Delta\vec{\delta})$;

  change cavity phase to ${}^{n+1}\vec{\delta} = {}^{n}\vec{\delta} + g\frac{J({}^{n}\vec{\delta}+{}^{n}\Delta\vec{\delta}) - J({}^{n}\vec{\delta})}{J({}^{n}\vec{\delta}+{}^{n}\Delta\vec{\delta})}{}^{n}\Delta\vec{\delta}$;

  n++

until *system stops*;

Here we utilize the measured error signal for the nth iteration along with a gain term g and a perturbing signal ${}^{n}\vec{\delta}$ that has perturbation depth d with the direction of the perturbation chosen randomly in order to update the vector of cavity phases after each iteration. The intuition for how this algorithm works can be obtained by examining how the error signal and the perturbation depth work together to move the metric function to a maximum. First it can be shown that for a sufficiently small perturbation depth d, upon each successive iteration the algorithm statistically moves in the direction of the gradient of the SHG function. Then further analysis reveals that the algorithm statistically increases the SHG signal until the derivative of the SHG signal approaches 0. So if the SHG signal is in the vicinity of a local maximum, this algorithm will work to increase the SHG signal until it reaches that local maximum, and then it will continue to work to ensure that the SHG signal stays at that maximum. This also means (and simulations confirm) that if the vector of cavity phases is in the vicinity of the optimized values, then the algorithm will converge to those optimized values.

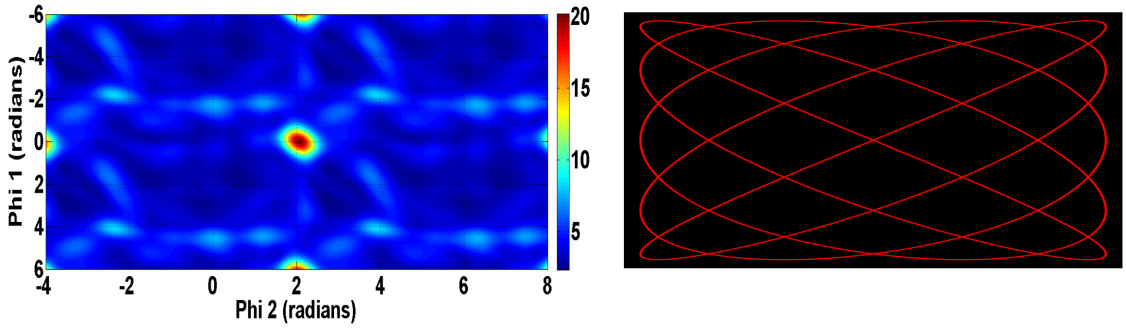

Figure 2.8: Lissajous scan of a 4-GTI cavity set, projected onto a 2-dimensional phase space. Left graph shows the peak power landscape in cavity phase space as measured by a SHG detector, and the cavity phase trajectory in a Lissajous pattern is shown on the right. Multiple Lissajous scans will locate a local optimum and release the cavity phases for active stabilization in the vicinity of a local peak [28].

However, during experiments the initial values of the cavity phases are effectively random due to random fluctuations. So in order to overcome this limitation, we

initially do a Lissajous search over the multi-dimensional space of the cavity phases. This places the cavity phases sufficiently close to the optimized values that the SPGD algorithm will converge to the optimum location. This algorithm is ignorant of the designed cavity phases, but through the optimization procedure it will find them automatically.

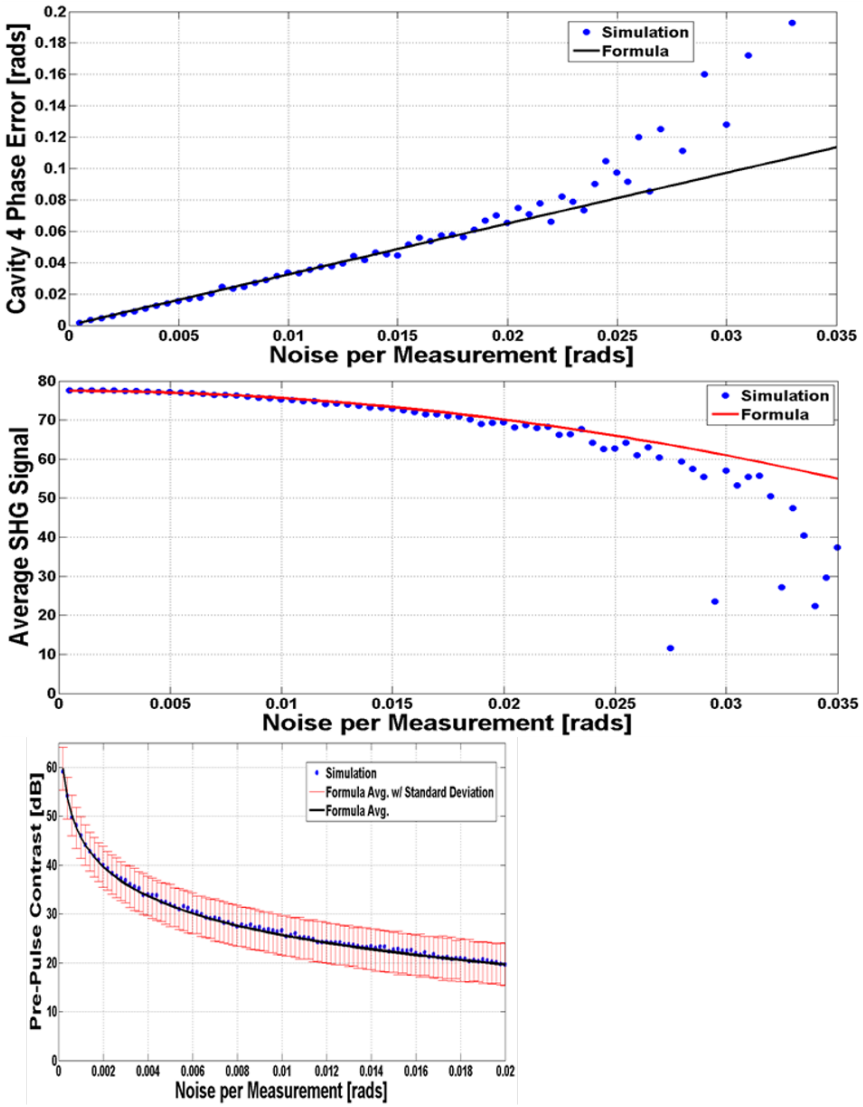

Figure 2.9: Cavity phase error, average SHG signal and achievable pre-pulse contrast using the SPGD algorithm with optimal parameters in a 4-GTI pulse stacking setting. A break down at noise values beyond ∼25mrad is predicted [28].

Analytic and numerical models for system-control level description of SPGD based stabilization has been developed [28]. As shown in Fig.2.9, both the stacked pulse peak

power, characterized by SHG signal proportional to peak power squared, and the pre-pulse contrast degrades with increased cavity noise, where the noise per measurement on the x axis is defined as the cavity phase noise standard deviation value in each simulated event. It was also shown in Fig.2.9 that for noise values beyond ∼25mrad, the simulation results significantly deviated from the analytically-derived curve, since the parabolic approximation used for deriving steady-state SPGD solution breaks down at cavity phase deviation larger than ∼25mrad. Preliminary comparison with the experiments indicate agreement with the predicted stabilization breakdown, and the predicted system stability.

2.5 Noise Characterization and Reduction in CPSA system

We use Allan deviation to quantify and characterize system amplitude and phase noise. The system phase noise information is retrieved through interference in the following steps. A burst of modulated pulses that can stack into one pulse in a single GTI cavity is created by loading appropriate amplitude and phase modulation signal onto EOMs, defined as a 1-cav stacking sequence. The pulse burst then propagates through the amplifier stages and a GTI cavity, and its peak power is collected after pulse compression. A cavity phase scanning with $> 2\pi$ range is performed to yield a SHG-cavity phase curve, and then the cavity is released on a linear segment of SHG-cavity phase curve to kick off SHG measurement under free drifting condition. The measured SHG signal amplitude noise is then projected to phase space via the SHG-cavity phase curve, and thus phase noise information is retrieved. An Allan deviation of the phase noise gives the time-domain noise distribution. Note that the measurable phase noise is limited by the amplitude noise floor using this method.

According to previous simulations, <25mrad cavity phase noise in GTI cavities is required to stabilize 4-GTI stacking. And it was derived that 9-ns GTI are 9-times more sensitive to phase noise than 1-ns GTI. According to the measurement in Fig.

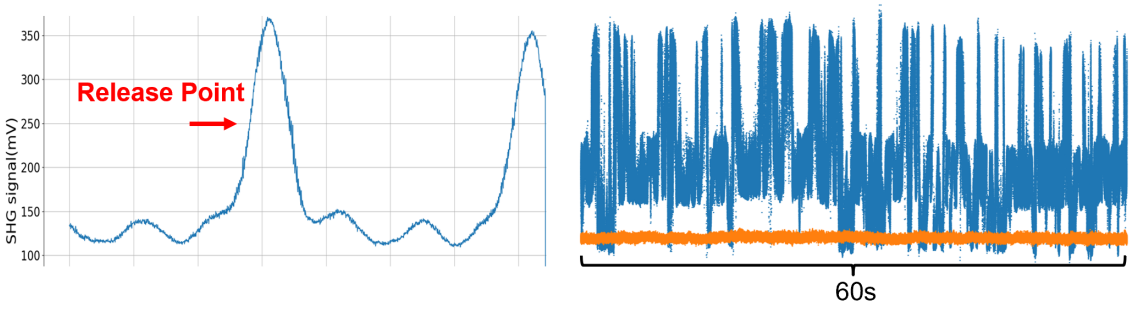

Figure 2.10: System phase noise characterized with a single GTI cavity.

2.10, 9-ns GTI cavity had 98mrad phase noise, and stabilization cannot be achieved. Therefore the phase noise must be reduced to within stabilization tolerance range.

The search for high phase noise origin was initiated, which can be summarized by the road map shown in Fig. 2.11. The initial hypothesis was that the phase noise originated from cavity phases noise, which was later proven to be false. A snapshot of the many unsuccessful attempts to dig out the noise source is shown in Fig. 2.12.

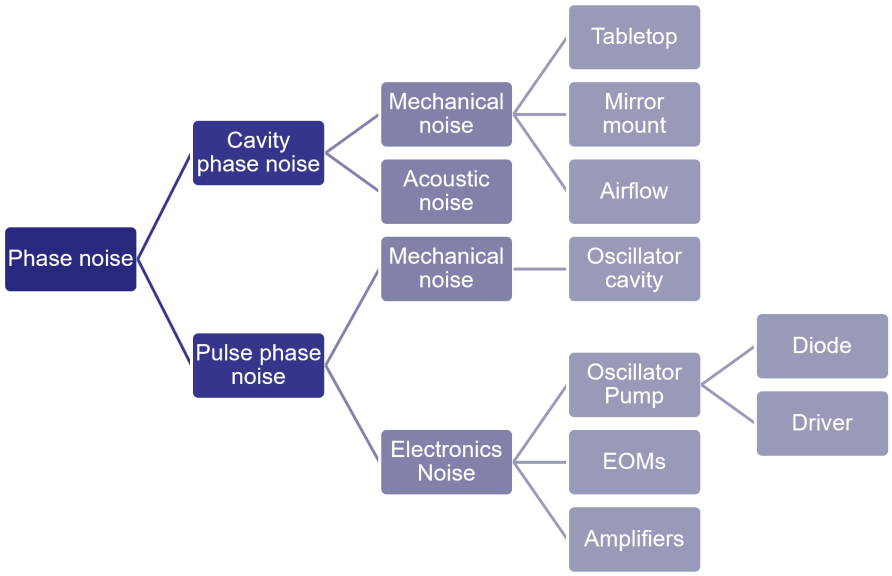

Figure 2.11: Road map for discovering the origin of high measured phase noise.

The root cause of high phase noise turns out to be coming from the electronics. The laser diode drivers used to pump the 4 sets of oscillator pump diodes have been proven to be imprinting 9dB white phase noise on the oscillator output pulse train,

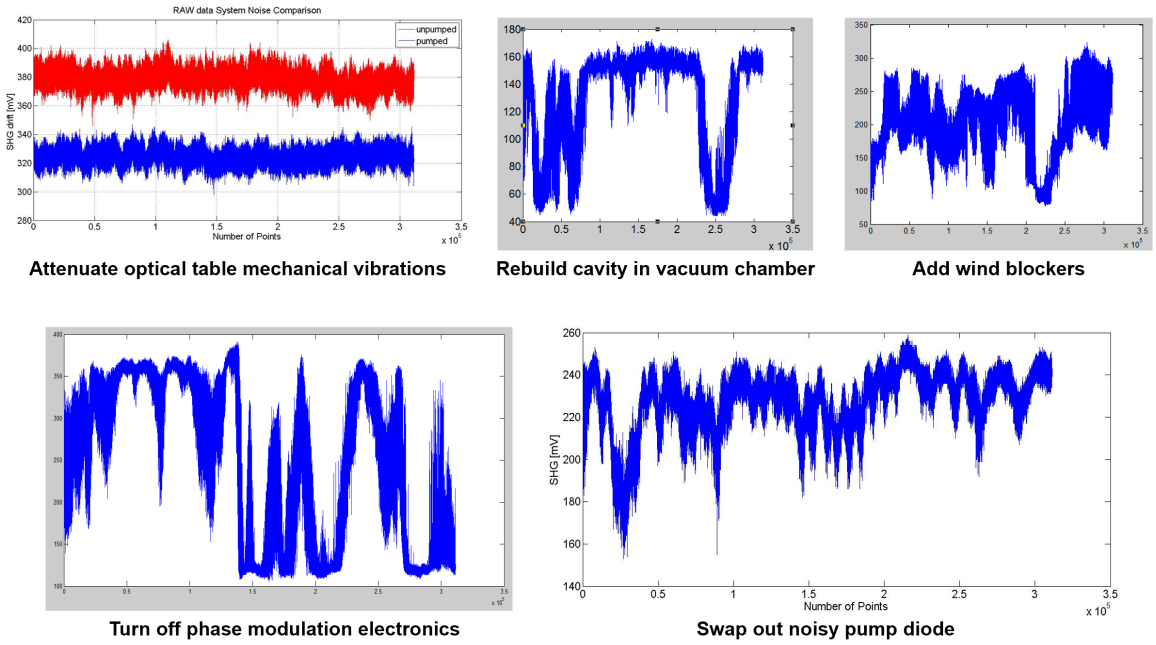

Figure 2.12: Multiple attempts of reducing phase noise yields little to no improvement.

as shown in Fig. 2.13. Such phase noise cannot be compensated otherwise and had to be removed by replacing them with quieter driver modules.

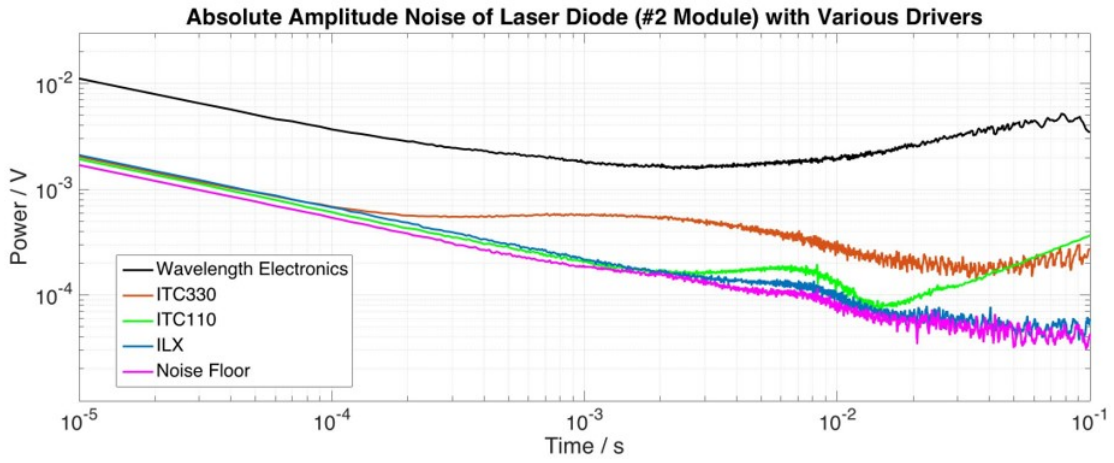

Figure 2.13: Allan deviation plot of laser diode amplitude noise driven by various laser driver modules.

The installation of quieter pump drivers deliver immediate improvement on phase noise, as depicted in Fig. 2.14. The measured phase noise dropped to within SPGD tolerance range, and dispatch of SPGD algorithm is enabled for 9-ns GTI cavities,

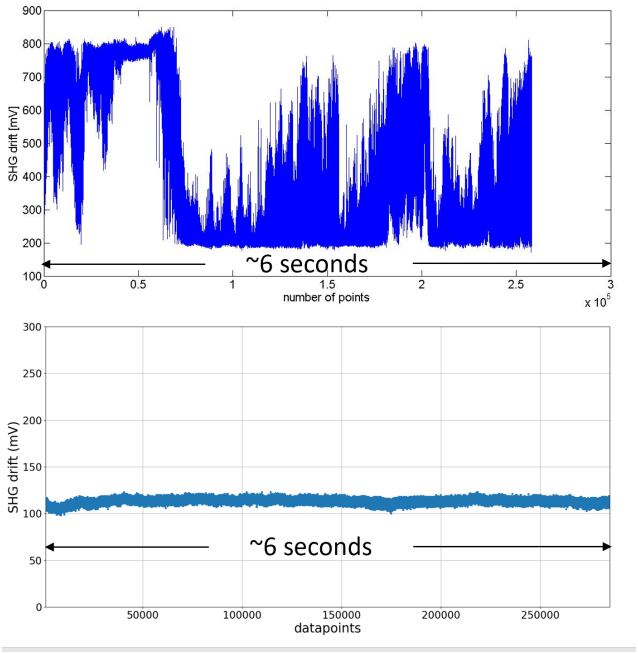

Figure 2.14: Phase noise in a 9-ns GTI cavity is reduced from 98mrad to 12mrad, which is within SPGD noise tolerance range.

initiating multiplexed GTI stacking of longer pulse train.

While most of the other attempts did not yield fast phase noise improvement, they provided valuable experience and insight on how the CPSA system interacts with internal and external noise sources, and the findings lead to the full enclosure of the entire GTI cavity set, which largely eliminates airflow-driven cavity phase drifts and enabled passive long-term stability of the interference system.

With significant system noise reduction, stacking phase noise is now oscillator, not stacker, limited. Note that achieved stacker phase noise levels (after oscillator stabilization) are close to the laser oscillator amplitude noise level, as shown in Fig.2.15. It will be discussed later in the dissertation that further stabilization of the oscillator is required to reach higher fidelity stacking, but GTI cavity stabilization has been fully enabled in absence of oscillator stabilization [30].

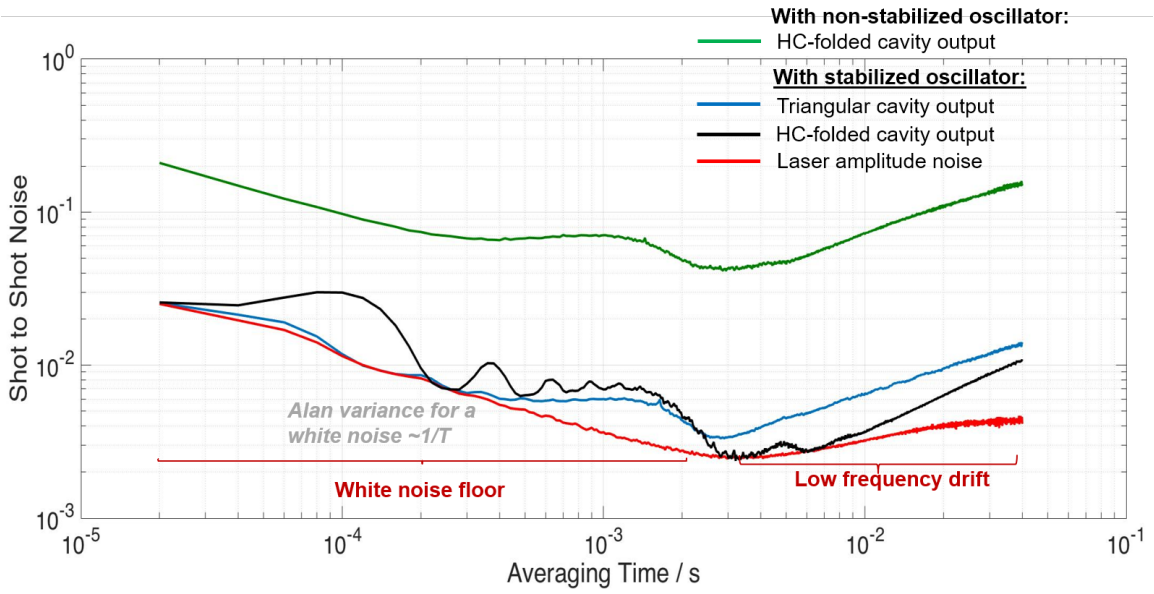

Figure 2.15: Allan-variance characteristics of measured stacking phase noise levels under various conditions.

2.6 Experimental Setup

In our experimental implementation we start with a ∼1 GHz repetition rate NPE mode-locked fiber oscillator that produces slightly chirped output pulses with a FWHM bandwidth of 23nm centered at 1032nm and a compressible pulse duration of 68fs. The pulses from the oscillator are amplitude and phase modulated using electro-optic modulators (EOMs) to produce bursts of 81 pulses at a repetition rate of 1MHz. The pulse bursts are amplified in a chain of single-mode fiber pre-amplifiers, where AOM gates between the stages suppress the ASE buildup, and control the burst repetition rate down to 100kHz.

The coherent pulse stacking setup consists of two sets of cascading 4 GTIs with partial reflectors 59%, 59%, 69%, and 69% and with roundtrip lengths of roughly 0.31m and 2.79m to match with integer times the roundtrip length of the oscillator. These mirror reflectivities are far from the optimal values and were just the measured reflectivity values from the vendor; however, this deviation from the ideal reflectivities is not predicted to have a significant impact on the stacking performance. Each GTI

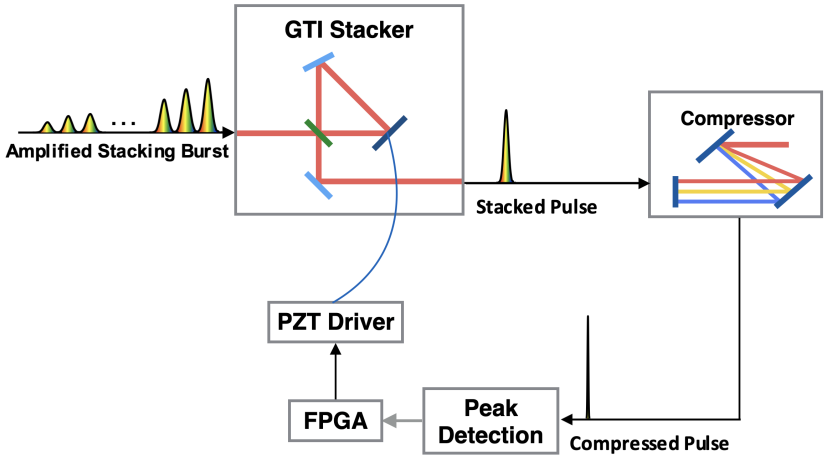

Figure 2.16: Experimental setup of coherent pulse stacking with active stabilization.

is arranged with all flat mirrors.

The amplified burst of 81 pulses is coherently stacked into one pulse in 4+4 multiplexed GTI cavities consisting of 4 sets of 1ns-roundtrip cavities followed by 4 sets of 9-ns roundtrip cavities, as shown in Fig.2.17. A fraction of the compressed output is then sent through a beta barium borate (BBO) doubling crystal to generate the second harmonic signal which is measured using a GaAsP photodiode from Thorlabs. The maximum speed of the photodiode is 2.7MHz, and since the burst of pulses only lasts for 81ns, the photodiode effectively integrates the second harmonic signal to produce the SHG metric signal that is used for stabilization. The feedback control for the cavity phases is achieved using FPGA hardware along with piezo-electric actuated mirror mounts. This type of digital stabilization scheme is scalable to arbitrary channel counts with speed up to the physical limitation of PZT response. Given the resonance frequency and the response time of the PZTs which are dampened by the load mass, the control system is currently running at up to ∼1kHz loop speed. The cavities are stabilized using FPGA-based SPGD algorithm, which maximizes the stacked-pulse peak power by constantly adjusting cavity phases via PZT mirrors.

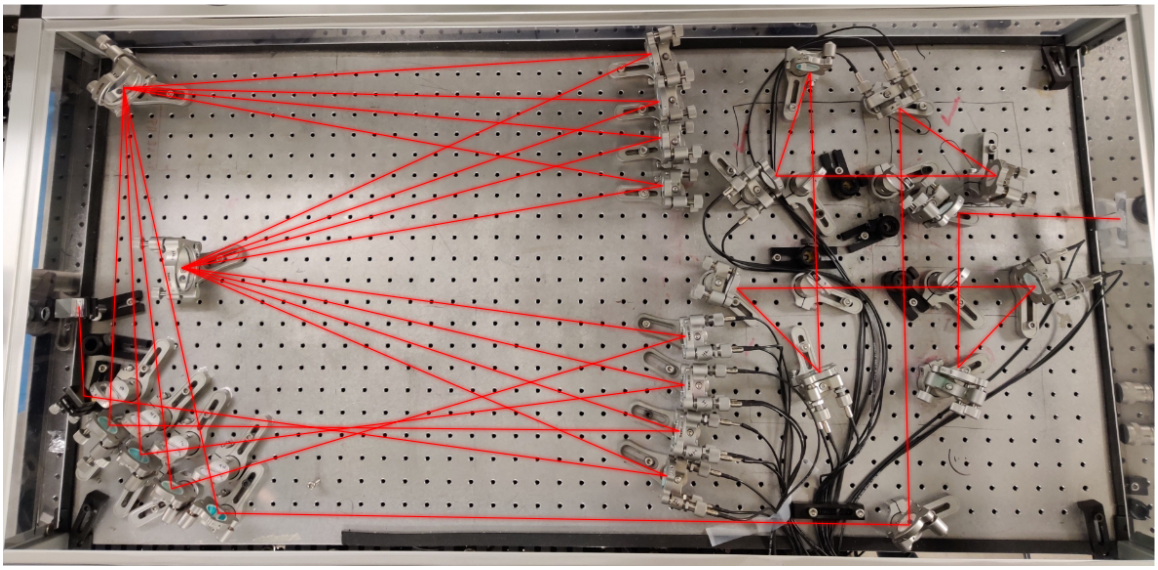

Figure 2.17: 4+4 GTI cavity configuration in experiment featuring all flat-mirror design and full enclosure. The cable-connected mirror mounts have PZTs in all three knobs to adjust the cavity phases, controlled by FPGA.

2.7 Experimental Results

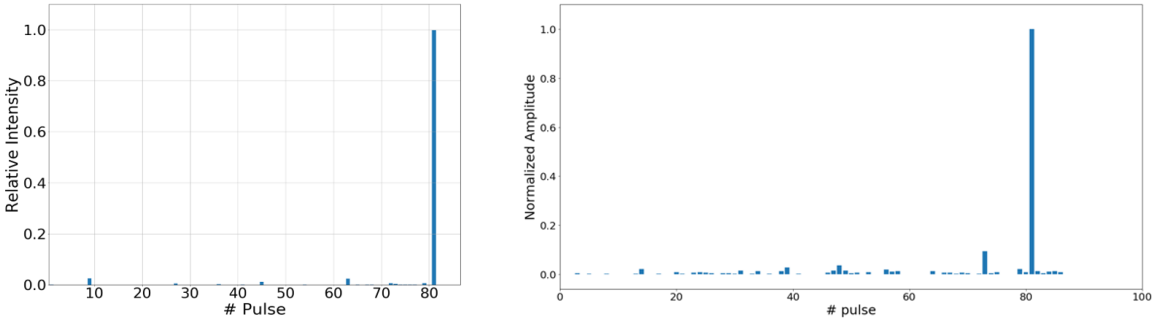

(a) Simulation

(b) Experiment

Figure 2.18: 81-pulse stacking using 4+4 multiplexed GTI cavities in (left) simulation that predicts 91% achievable stacking efficiency in absence of any cavity alignment errors and (right) experimental result with 66.5% achieved stacking efficiency

The experimental traces for the normalized input and output pulse trains are shown in Fig. 2.18 along with a simulation of the experimental conditions. Here normalized means setting the sum of the input peak powers equal to the sum of the output peak powers. This is necessary since both the input and output pulse trains were measured after the GTIs, with the input trains being measured with all of the

cavities blocked. The small pre and post pulses that appear only in the experimental train are most likely attributed to the phases of the input pulses being imperfect. The discrepancies between the simulated and the experimental stacking fidelity are due to existence of pulse modulation and cavity alignment errors that requires adaptive optimization and high-precision stacking techniques, which will be discussed in the next chapter. In order to further suppress these unwanted satellite pulses, a closed loop optimization of the input pulse phases and amplitudes is needed, together with precise control of cavity alignment errors.

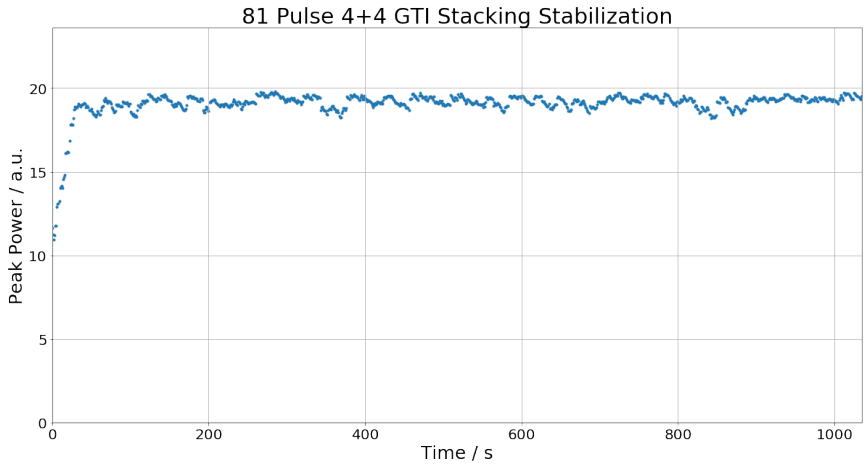

Figure 2.19: Stabilization of the 81-pulse stacking with σ=1.4% peak power stability over >15min.

In the experimental implementation, the output pulse train was measured to be stable for over 1 hour, after which the experiment was turned off. A 15 minute portion of this data is shown in Fig. 2.19, which shows the SHG signal vs. time over this period. This data shows that the SHG signal has a standard deviation of σ_{SHG} = 2.8%, corresponding to a standard deviation of the peak of the pulse train of σ_{Iout} = 1.4%.

CHAPTER III

High Fidelity Coherent Pulse Stacking Amplification

3.1 Introduction

3.1.1 High fidelity and high contrast stacking

High efficiency combining requires identical pulse shapes in the burst, thus requiring an equal nonlinear phase across the pulse burst. Therefore, the amplitude envelope of the burst should not only compensate for gain saturation in high power amplifiers, but also be smooth enough to avoid pulse-to-pulse nonlinearity variation, as illustrated in Fig. 3.1. Since the exact profile shape depends on the energy extraction level, an adaptively and yet precisely prescribed profile is necessary.

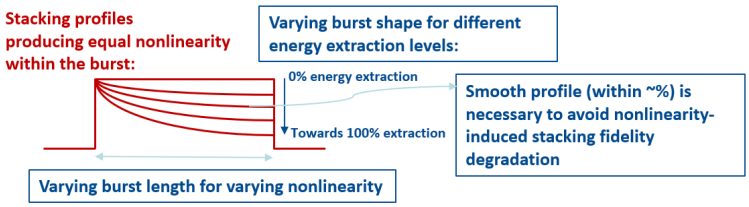

Figure 3.1: Demonstration of stacking pulse burst smoothness requirements to reach high stacking fidelity [9].

Meanwhile, the accelerator community calls for high pre-pulse contrast in the next generation LPA driver, as the plasma channel shall remain uninterrupted until the

ultraintense main pulse drives the particle acceleration in its wake. Since in this particular application of laser plasma acceleration it is required to have a 30-40dB contrast in peak intensity, pre-pulse contrast is defined in terms of ratio in peak power $\chi_{peak} = P_{pre-pulse}/P_{stacked}$. It can also be defined in terms of ratio of stacked pulse energy to totally leaked energy of all pre-pulses $\chi_{energy} = E_{pre-pulse}/E_{stacked}$, which might be useful for other applications. In the rest of this dissertation, pre-pulse contrast is defined as ratio of stacked pulse peak power to the peak power of the highest pre-pulse.

3.1.2 Practical challenges

The implementation of CPSA system faces a few key practical challenges.

First, CPSA system parameter uncertainty exists in multiple aspects. Since the temporal combining in the GTI cavities require very specific pulse amplitudes and phases as its input burst, the pulse burst modulation has to propagate through the collective transfer function of all the upstream system components to deliver those exact parameters, and this leads to the challenge of CPSA system parameter uncertainty.

The amplitude and phase modulation starts as digital number arrays in the FPGA that are translated to analog RF signals to be amplified and posed on top of oscillator output pulses through EOMs. The transfer function from FPGA to EOMs brings the first level of uncertainty. The modulated pulses then propagate through several stages of amplifiers to further go through amplitude and phase changes, which are dependent on the pumping conditions that might change over time. Furthermore, even the mirror reflectivities in the GTI cavities cannot be specified beyond 0.5% precision, which fundamentally brings uncertainty to its corresponding optimum pulse envelope shape and phases. As the net consequence of these system uncertainties, an optimum stacking profile cannot be fully specified up front with a simple analytical approach.

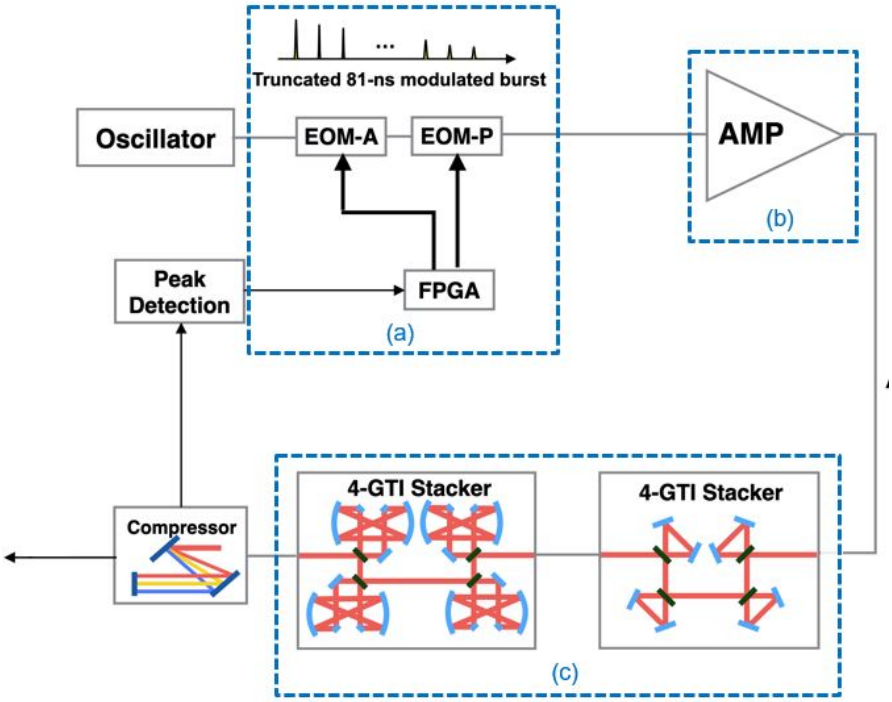

Figure 3.2: CPSA System Parameter Uncertainties exist in 3 aspects: (a) amplitude & phase modulation uncertainty, (b) amplitude & phase changes through amplifiers, and (c) GTI mirror reflectivities cannot be specified beyond 0.5% precision.

Second, depending on the layout design of GTI cavities, there are physical limitations that must be taken into consideration. The number of mirrors and their reflectivities determine the cavity round-trip loss, which will affect the stacking fidelity and overall system transmission. If the GTI cavity design involves beam folding, e.g. Herriott cells, then cavity round-trip polarization rotation might occur that degrades the interference. The compatible beam size is limited by clear apertures and ratio of Rayleigh range of cavity roundtrip length, which together with mirror coating damage threshold limits the energy tolerance of the system.

Another major practical challenge is the pulse errors generated by GTI cavity misalignment. These errors include angular error (affects beam angle), piston error (affects round-trip cavity length) and transversal error (affects beam overlap). These errors either randomly occur as the mirrors are aligned, or systematically accumulate as some key system components drift. The identification and elimination of these

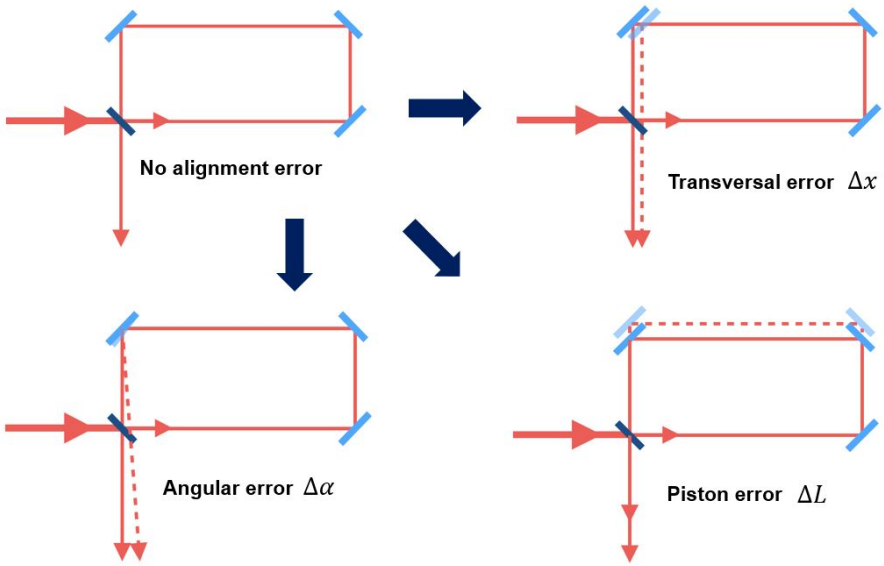

Figure 3.3: Three types of alignment errors can occur in a GTI cavity.

errors is limited by the detection metrics and resolutions, and a comprehensive theory must be established to quantify the effect of these alignment errors on stacking.

3.2 Transfer Matrix Description of Coherent Pulse Stacking

Given the existence of uncertainties and errors in the CPSA system, it is critical to establish a theoretical framework that accounts for the interaction among these errors and their impact on coherent combining. It has been established that a sequence of GTI cavities can be described by linear time invariant system theory that can be written in the transfer matrix format, which we will apply throughout this section.

3.2.1 Transfer matrix of GTI cavity set

An input pulse train to the GTI cavity set was defined in Eq.2.1. Since in this section we assume all input pulses have identical pulse shapes and are only differentiated by their amplitudes and phase, we simplify the expression of an individual pulse down to a complex electric field denoting the pulse's amplitude and phase $E^{in(i)} = A_i e^{i\phi_i}$.

Denote $\vec{E}^{in} = (E^{in(0)}, E^{in(1)}, E^{in(2)}, \cdots)$ as the input pulse train, where each el-

ement $E^{in(k)}$ is the electric field of the kth input pulse. The pulse train is discrete, since it is produced by a mode-locked oscillator whoso repetition rate f_{rep} determines the separation between these pulses $\Delta t = 1/f_{rep}$.

First let's consider a single GTI cavity with electric field reflectivity r, cavity phase δ_i, roundtrip loss α, and cavity roundtrip length $L_{cav} = L_{sep}$. Its impulse response, neglecting any alignment or control errors and only consider the amplitude and phase, is $(H^{(0)}, H^{(1)}, H^{(2)}, H^{(3)}, \cdots)$, where $H^{(0)} = r$, $H^{(i)} = -r^i(\frac{1}{r} - r)e^{i\delta_i}\alpha^i$ for $i \geq 1$, where i denotes the number of roundtrips a pulse propagates in the GTI before it exits the cavity. Therefore, the output pulse train of a single GTI with a single input pulse is:

$$(E^{out(0,0)}, E^{out(0,1)}, E^{out(0,2)}, \cdots) = (H^{(0)}, H^{(1)}, H^{(2)}, \cdots)E^{in(0)} \tag{3.1}$$

or in matrix form:

$$\begin{pmatrix} E^{out(0,0)} \\ E^{out(0,1)} \\ E^{out(0,2)} \\ \vdots \end{pmatrix} = \begin{pmatrix} H^{(0)} \\ H^{(1)} \\ H^{(2)} \\ \vdots \end{pmatrix} E^{in(0)} = \begin{pmatrix} H^{(0)} & 0 & 0 & \cdots \\ H^{(1)} & 0 & 0 & \cdots \\ H^{(2)} & 0 & 0 & \cdots \\ \vdots & \vdots & \vdots & \vdots \end{pmatrix} \begin{pmatrix} E^{in(0)} \\ 0 \\ 0 \\ \vdots \end{pmatrix} \tag{3.2}$$

Since $L_{cav} = L_{sep}$, the n-th input pulse has a time delay of n, and the output pulse train is:

$$(E^{out(n,0)}, E^{out(n,1)}, E^{out(n,2)}, \cdots) = (0, \cdots, 0, H^{(0)}, H^{(1)}, H^{(2)}, \cdots)E^{in(n)} \tag{3.3}$$

or in matrix form:

$$\begin{pmatrix} E^{out(n,0)} \\ E^{out(n,1)} \\ E^{out(n,2)} \\ \vdots \end{pmatrix} = \begin{pmatrix} 0 \\ \vdots \\ 0 \\ H^{(0)} \\ H^{(1)} \\ \vdots \end{pmatrix} E^{in(0)} = \begin{pmatrix} 0 & \cdots & 0 & 0 & 0 & \cdots \\ \vdots & \vdots & \vdots & \vdots & \vdots & \vdots \\ 0 & \cdots & 0 & 0 & 0 & \cdots \\ 0 & \cdots & 0 & H^{(0)} & 0 & \cdots \\ 0 & \cdots & 0 & H^{(1)} & 0 & \cdots \\ \vdots & \vdots & \vdots & \vdots & \vdots & \vdots \end{pmatrix} \begin{pmatrix} 0 \\ \vdots \\ 0 \\ E^{in(n)} \\ 0 \\ \vdots \end{pmatrix} \tag{3.4}$$

Since it was established that a GTI cavity is a LTI system, the LTI system responses from all input pulses linearly add up. Summing Eq.3.4 for all input pulses yields:

$$\vec{E}^{out} = \begin{pmatrix} E^{out(0)} \\ E^{out(1)} \\ E^{out(2)} \\ \vdots \end{pmatrix} = \begin{pmatrix} H^{(0)} & 0 & 0 & \cdots \\ H^{(1)} & H^{(0)} & 0 & \cdots \\ H^{(2)} & H^{(1)} & H^{(0)} & \cdots \\ \vdots & \vdots & \vdots & \vdots \end{pmatrix} \begin{pmatrix} E^{in(0)} \\ E^{in(1)} \\ E^{in(2)} \\ \vdots \end{pmatrix} = \mathcal{H}\vec{E}^{in} \tag{3.5}$$

and therefore the single GTI transfer matrix is:

$$\mathcal{H} = \begin{pmatrix} H^{(0)} & 0 & 0 & \cdots \\ H^{(1)} & H^{(0)} & 0 & \cdots \\ H^{(2)} & H^{(1)} & H^{(0)} & \cdots \\ \vdots & \vdots & \vdots & \vdots \end{pmatrix} \tag{3.6}$$

Note that it is a lower-triangular matrix, which means $E^{in(k>n)}$ input pulses have no contribution to $E^{out(k\leq n)}$ due to causality.

Now consider a single GTI cavity with $L_{cav} = mL_{oscillator}$ where m is an integer greater than 1. Following the above derivation, as after n roundtrips the output pulse would interfere with the $m * n$th input pulse, it is a sparse matrix:

$$\mathcal{H} = \begin{pmatrix} H^{(0)} & 0 & 0 & \cdots \\ 0 & H^{(0)} & 0 & \cdots \\ \vdots & 0 & H^{(0)} & \cdots \\ 0 & \vdots & 0 & \cdots \\ H^{(1)} & 0 & \vdots & \cdots \\ 0 & H^{(1)} & 0 & \cdots \\ \vdots & \vdots & \vdots & \vdots \end{pmatrix} \tag{3.7}$$

For multiple cascading and multiplexed GTIs, denote $\vec{E}_m^{out}$ and $\vec{E}_m^{in}$ as the output and input pulse train of the mth GTI cavity. Since the output of the $m-1$th GTI is exactly the input of the mth GTI, we have $\vec{E}_m^{in} = \vec{E}_{m-1}^{out}$, and thus:

$$\vec{E}_m^{out} = \mathcal{H}_m \mathcal{H}_{m-1} \cdots \mathcal{H}_0 \vec{E}_0^{in} \tag{3.8}$$

Thus we obtain the transfer matrix of m cascading GTIs:

$$\mathcal{H} = \mathcal{H}_m \mathcal{H}_{m-1} \cdots \mathcal{H}_0 \tag{3.9}$$

3.2.2 Transfer matrix of GTI cavity set with errors

If a pulse propagates free of any errors, then its amplitude and phase can be expressed by a single complex number $E_i = A_i e^{i\phi_i}$, where A_i is the electric field amplitude and ϕ_i is the phase. However, a pulse not only has a temporal envelope $a(t)$, it also propagates as a Gaussian beam, and therefore considering all these factors we have:

$$E_i(x,y,z,t) = A_i a(t) e^{i(\phi_i+\omega t)} \frac{w_0}{w(z)} e^{-\frac{x^2+y^2}{w^2(z)}} e^{-i\frac{k(x^2+y^2)}{2R(z)}} e^{i\psi(z)} e^{-ikz} \tag{3.10}$$

It has been established in [28, 31] that combining Gaussian beams with spatial errors has combining efficiency measured in power as the following:

$$\eta_{\Delta\delta} = 1 - \frac{(\frac{kw_0\Delta\delta}{2})^2}{4}$$
$$\eta_{\Delta x} = 1 - \frac{(\frac{\Delta x}{w_0})^2}{4}$$
$$\eta_z = 1 - \frac{(\frac{z_1-z_2}{\sqrt{2}z_R})^2}{4}$$

Since all the errors are defined relative to the reference path P_1, the spatial-domain combining efficiencies can be combined via the above equations with the amplitude term of $E_i(x,y,z,t)$ as $\tilde{A}_i = \sqrt{\eta_{\Delta\delta}\eta_{\Delta x}\eta_z}A_i$. Now consider the time-domain combining of pulses $E_i(t) = \tilde{A}_i a(t-\tau_i)cos(\phi_i+\omega t)$, where $a(t)$ is the normalized temporal envelope, τ_i is the time delay, and pulse phase is determined by the time delay by $\phi_i = \omega\tau_i$. Here we use the cosine function to express phase information as only the real part of the complex form has physical meaning. The total field of n pulses is

$$E_{total} = \sum_i^n E_i(t) = \sum_i^n A_i a(t-\tau_i)cos(\phi_i+\omega t)$$

. The optical detector measures the total transmitted power, which is the integration of the optical intensity of the total field over time:

$$
\begin{aligned}
I_{total} &= \int_{-\infty}^{+\infty} [\sum_{i}^{n} A_i a(t-\tau_i) cos(\phi_i + \omega t)]^2 dt \\
&= \int_{-\infty}^{+\infty} [\sum_{i=1}^{n} A_i^2 a^2(t-\tau_i) cos^2(\phi_i + \omega t) \\
&\quad + 2\sum_{i=1}^{n}\sum_{j=i+1}^{n} A_i A_j a(t-\tau_i) a(t-\tau_j) cos(\phi_i + \omega t) cos(\phi_j + \omega t)] dt \\
&= \sum_{i=1}^{n} A_i^2 + 2\sum_{i=1}^{n}\sum_{j=i+1}^{n} A_i A_j \int_{-\infty}^{+\infty} [a(t-\tau_i) a(t-\tau_j) cos(\phi_i + \omega t) cos(\phi_j + \omega t)] dt \\
&= \sum_{i=1}^{n} A_i^2 + 2\sum_{i=1}^{n}\sum_{j=i+1}^{n} A_i A_j cos(\phi_i - \phi_j) \int_{-\infty}^{+\infty} a(t-\tau_i) a(t-\tau_j) dt \\
&= \sum_{i=1}^{n} A_i^2 + 2\sum_{i=1}^{n}\sum_{j=i+1}^{n} A_i A_j cos(\omega(\tau_i - \tau_j)) \int_{-\infty}^{+\infty} a(t) a(t-(\tau_i - \tau_j)) dt
\end{aligned}
\tag{3.11}
$$

Here we have some observations. If there are no relative delays among pulses, $\int_{-\infty}^{+\infty} a(t)a(t-(\tau_i-\tau_j))dt = \int_{-\infty}^{+\infty} a^2(t)dt = 1$, the expression reduces to the standard interference equation where pulses perfectly interfere with each other. If the relative delays are much larger than the coherence time such that these pulses incoherently combine, $\int_{-\infty}^{+\infty} a(t)a(t-(\tau_i-\tau_j))dt \longrightarrow 0$, the interference term is eliminated and the measured total power is only the simple sum of the power of each individual pulse. This derivation provides the critical tool to account for the effect of piston errors and relative pulse delays in stacking.

As a typical example, if we assume that the normalized pulse temporal envelope function $a(t)$ is Gaussian, i.e. $a^2(t) - N(0, \tau_{coh})$, where τ_{coh} is the coherence time,

then we have

$$a^2(t) = \frac{1}{\sqrt{2\pi}\tau_{coh}} e^{-\frac{t^2}{2\tau_{coh}^2}}$$

, then

$$\begin{aligned}
\int_{-\infty}^{+\infty} a(t-\tau_i)a(t-\tau_j)dt &= \int_{-\infty}^{+\infty} \frac{1}{\sqrt{2\pi}\tau_{coh}} e^{-\frac{t^2}{4\tau_{coh}^2}} e^{-\frac{(t-(\tau_i-\tau_j))^2}{4\tau_{coh}^2}} dt \\
&= \int_{-\infty}^{+\infty} \frac{1}{\sqrt{2\pi}\tau_{coh}} e^{-\frac{1}{4\tau_{coh}^2}(2t^2-2t(\tau_i-\tau_j)+(\tau_i-\tau_j)^2)} dt \\
&= \int_{-\infty}^{+\infty} \frac{1}{\sqrt{2\pi}\tau_{coh}} e^{-\frac{1}{2\tau_{coh}^2}[(t-\frac{\tau_i-\tau_j}{2})^2+\frac{1}{4}(\tau_i-\tau_j)^2]} dt \\
&= e^{-\frac{(\tau_i-\tau_j)^2}{8\tau_{coh}^2}} \int_{-\infty}^{+\infty} \frac{1}{\sqrt{2\pi}\tau_{coh}} e^{-\frac{1}{2\tau_{coh}^2}[(t-\frac{\tau_i-\tau_j}{2})^2]} dt \\
&= e^{-\frac{(\tau_i-\tau_j)^2}{8\tau_{coh}^2}}
\end{aligned} \tag{3.12}$$

Thus we have:

$$I_{total} = \sum_{i=1}^{n} A_i^2 + 2\sum_{i=1}^{n}\sum_{j=i+1}^{n} A_i A_j cos(\phi_i - \phi_j) e^{-\frac{(\tau_i-\tau_j)^2}{8\tau_{coh}^2}} \tag{3.13}$$

3.3 Coherent pulse stacking as a Deep Recurrent Neural Network

Given the mathematical description of a coherent pulse stacking system in Eq. 3.8, it is equivalent to a deep recurrent neural network (DRNN) [32]. Its input layer and output layer are input pulse time series and output pulse time series respectively, and each recurrent hidden layer is a GTI cavity, as shown in Fig. 3.4. Forward propagation of a time series through the network is equivalent to sending an input pulse burst through the GTIs, and backpropagation from a single normalized output node yields the impulse response of the GTI cavity set.

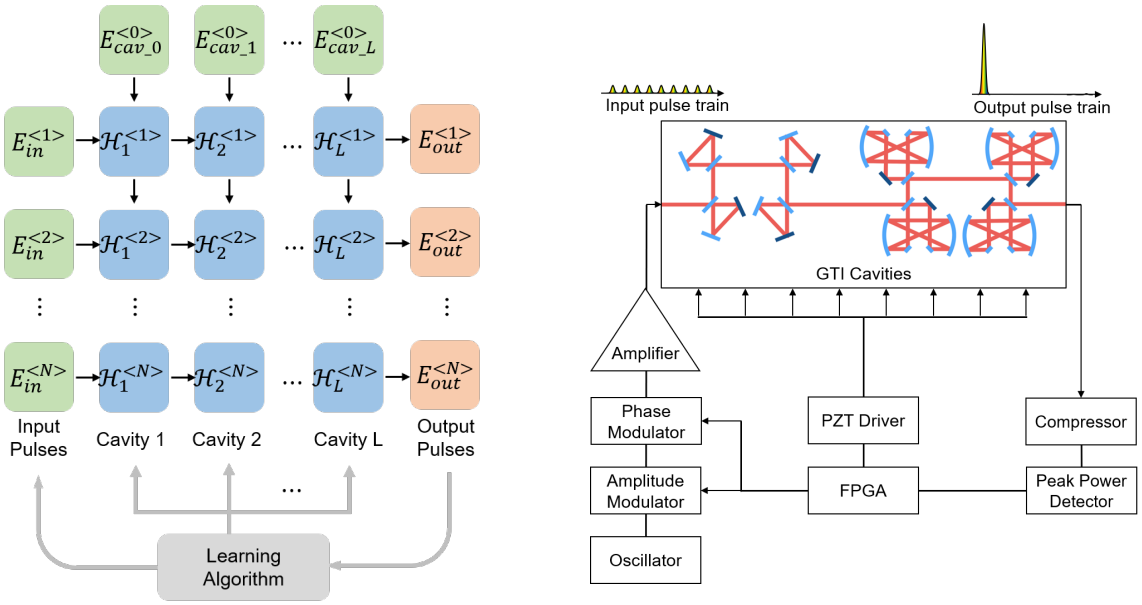

Figure 3.4: (Left) Deep recurrent neural network description of coherent pulse stacking; (Right) system schematic of a coherent pulse stacking amplification system.

The input layer is a time series of modulated pulses defined as $E_{in}^{<t>} = A_{in}e^{i\phi_{in}}$, and $E_{cav}^{[l]<t>}$ denotes the stored electric field that recurrently propagates in the l-th GTI cavity. The output of the t-th node in the l-th layer is the input of the t-th node in the $l+1$-th layer. The structure of a hidden layer node is illustrated in Fig. 3.5, with weights defined as $W_\delta = \alpha e^{i\delta}, W_r = r, W_t = it$, where r is the electric field reflectivity of the cavity front mirror, $t = \sqrt{1-r^2}$ is the electric field transmission of the cavity front mirror, δ is the cavity phase, and α is the cavity roundtrip loss.

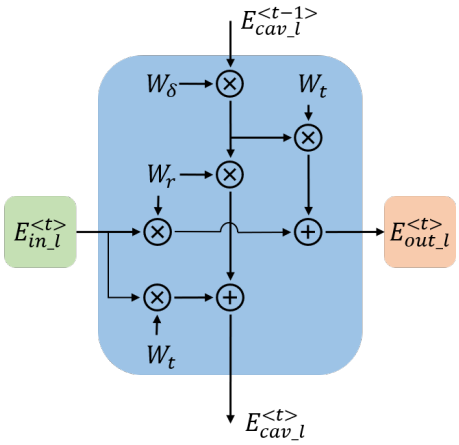

Figure 3.5: Structure of a recurrent node in the l-th hidden layer at time step t.

This DRNN framework can be used to design and operate a coherent pulse stacking system. To design the physical layout of a cavity set, backpropagation of a single stacked output pulse is used to train the neural network until a desirable input pulse burst shape is obtained, which yields an optimal number of layers and their key cavity parameters including front mirror reflectivities and cavity phases. The GTI cavity set is then built accordingly, where the number of cavities and front mirror reflectivities are fixed, but cavity phases are controllable via PZT mirrors. Input pulses are sent through the cavity set, whose output feeds back into the neural network to learn the optimal combination of cavity and input parameters that allows the cavity set to stack the input pulses into a single pulse with high stacking efficiency and pre-pulse contrast. Note that while cavity stored electric fields are initialized as zero in truncated pulse burst stacking, they can be set as non-zero trainable parameters to retrieve a corresponding burst-tail that enables high pre-pulse contrast coherent pulse stacking.

In operation, system noises and parameter uncertainties cannot be explicitly specified, but they can be learned and compensated by the neural network to achieve high fidelity stacking. Active stabilization of the GTI cavities compensates for phase noises and drifts, and real-time learning on the input pulse burst optimizes pulse stacking.

3.4 Coherent pulse stacking with alignment errors

As the burst of modulated, stretched and amplified pulses exits the fiber amplifier and starts propagating in free space as a Gaussian beam, it is quite literally a "pulse train" moving at the speed of light following the same path, where each carriage is a stretched pulse. In an alignment error-free coherent pulse stacking scenario, all pulses are only differentiated by their amplitudes and phases and are identical otherwise, and pulses interfere with perfect spatial and temporal overlap. However, as these pulses propagate through the GTI cavities, they can accumulate 3 types of alignment

errors: transversal error Δx, angular error $\Delta\alpha$ and piston error Δd. These errors will prevent pulses from overlapping perfectly in space and in time, therefore causing degradation in coherent combining performance. This section will discuss in detail how a pulse burst accumulate alignment errors as it propagates through GTI cavities, how it affects stacking performance and how to control and eliminate these errors.

3.4.1 Definition of alignment errors in GTI cavities

To start with, we set our foundation of analysis and give definition of alignment errors. Since the beam path is determined by the front mirrors of the GTI cavities, we define it as the reference path P_1 along which all beams exiting GTIs are overlapped. All spatial and temporal errors are defined with respect to this reference path. Therefore, by definition, the refence path does not contain any errors, and GTI front mirrors do not incur any alignment errors.

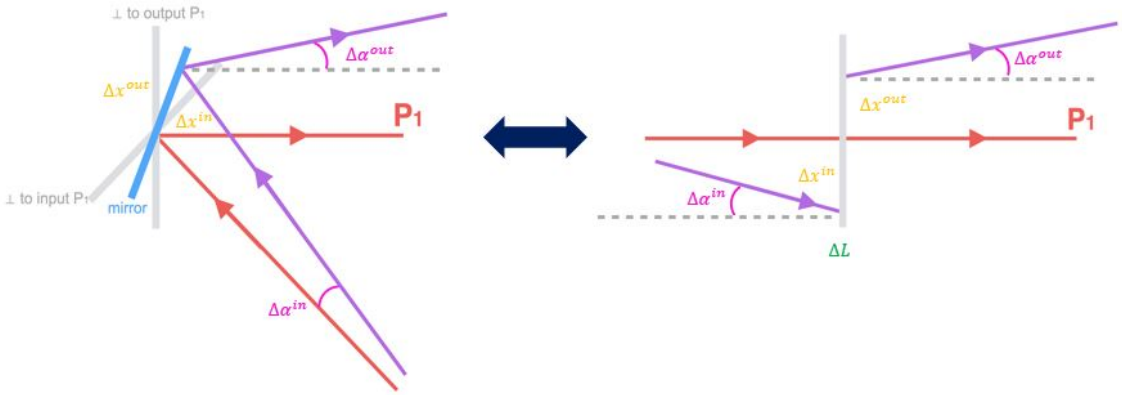

Figure 3.6: The equivalent layout to the actual ring-cavity mirror layout has effective mirrors perpendicular to the beam path.

To characterize how mirror misalignment deviates a beam from the reference path and how a deviated beam propagates in optical cavities, we need to analytically derive the interaction between a beam and a mirror. With the pre-defined reference path, one straightforward approach would be pure geometrical analysis based on positioning of individual mirror surfaces, but such method becomes cumbersome with increasing

number of mirrors. Instead, we adopt a method that tracks wavefront planes which are always perpendicular to the reference path, and with this method, a reflecting mirror is equivalent to two "effective mirrors" perpendicular to the input and the reflecting reference path, as shown in Fig. 3.6.

We also set a few sign conventions:

1. If $\Delta\alpha_i$ is measured clockwise from the reference path P_1, then $\Delta\alpha_i > 0$.
2. If the mirror is tilted clockwise from the ideal position, then $\Delta\beta_i > 0$.
3. If the beam transversely shifts to the left of the reference path, then $\Delta x > 0$.

3.4.2 Propagation of alignment errors in GTI cavities

Now consider the scenario where a beam with input angular error $\Delta\alpha^{in}$ and input transversal error Δx^{in} hits the mirror. All errors are considered small, and small-value approximation will apply to eliminate all higher-order infinitesimals. If the mirror itself is fully aligned and does not produce any additional alignment errors, then upon reflection from the mirror surface, the alignment errors change to:

$$\begin{aligned} \Delta x^{out} &= -\Delta x^{in} \\ \Delta\alpha^{out} &= -\Delta\alpha^{in} \\ \Delta L^{mir} &= 0 \end{aligned} \tag{3.14}$$

Here we observe that Δx, $\Delta\alpha$ change signs upon reflection under our defined sign convention.

Now if the mirror is tilted by $\Delta\beta$ such that it brings both tilt and piston error to the pulse train, we have:

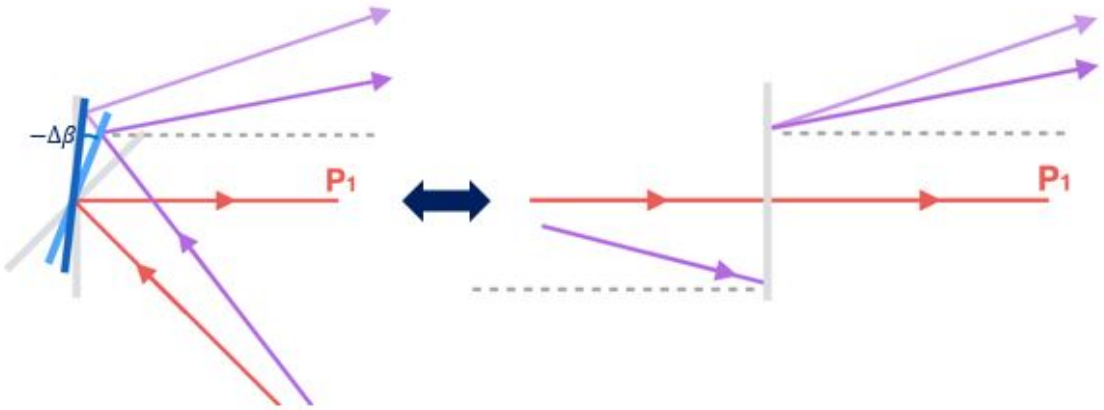

Figure 3.7: The alignment errors caused by tilting a mirror by $\Delta\beta$

$$\Delta\alpha^{out} = -(\Delta\alpha^{in} + 2\Delta\beta)$$

$$\frac{\Delta L^{in}}{\sin(\alpha_i + \Delta\beta)} = \frac{\Delta x^{in}}{\sin(\pi/2 - \alpha_i - \Delta\alpha^{in} - \Delta\beta)} = \frac{\Delta x^{mir}}{\sin(\pi/2 + \Delta\alpha^{in})}$$

$$\frac{\Delta L^{out}}{\sin(\alpha_i - \Delta\beta)} = \frac{-\Delta x^{out}}{\sin(\pi/2 - \alpha_i - \Delta\alpha^{in} - \Delta\beta)} = \frac{\Delta x^{mir}}{\sin(\pi/2 + \Delta\alpha^{in}) + 2\Delta\beta}$$

$$\Delta x^{out} = -\Delta x^{in}\frac{\cos(\Delta\alpha^{in})}{\cos(\Delta\alpha^{in} + 2\Delta\beta)} \approx -\Delta x^{in}$$

$$\Delta L^{mirror} = \Delta L^{out} - \Delta L^{in} \approx 0.$$

To summarize, for a tilt error of $\Delta\beta$ on the mirror:

$$\begin{aligned} \Delta\alpha^{out} &= -(\Delta\alpha^{in} - 2\Delta\beta) \\ \Delta x^{out} &= -\Delta x^{in} \\ \Delta L^{mir} &= 0 \end{aligned} \tag{3.15}$$

Now the mirror can also be misaligned piston-wise to create transversal and piston errors with respect to the perfect path.

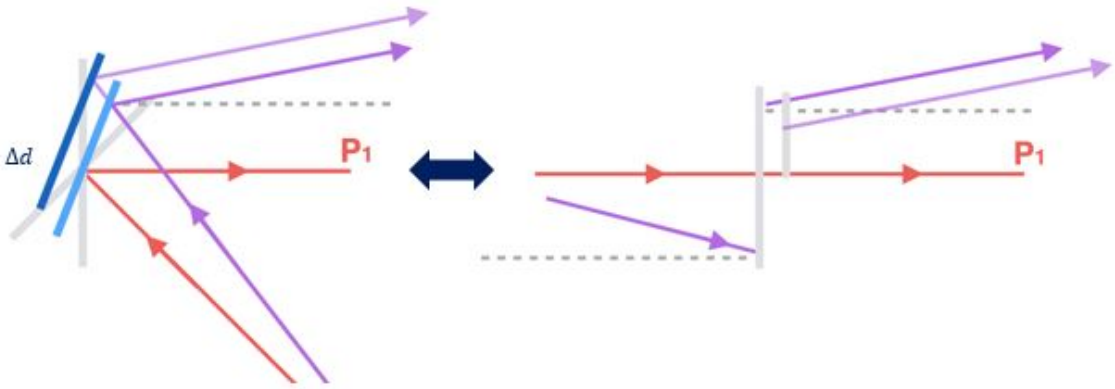

Figure 3.8: The alignment errors caused by retracting a mirror by Δd

$$\begin{aligned}
\Delta L^{in}|_{\Delta d} &= \Delta L^{in}|_{\Delta d=0} + \frac{\Delta d}{\cos\alpha_i} \\
\Delta L^{out}|_{\Delta d} &= \Delta L^{out}|_{\Delta d=0} - \frac{\Delta d}{\cos\alpha_i} \cdot \frac{\sin(\pi/2 - 2\alpha_i - \Delta\alpha^{in})}{\sin(\pi/2 - \Delta\alpha^{in})} \\
\Delta L^{mir} &= \Delta L^{in}|_{\Delta d=0} + \frac{\Delta d}{\cos\alpha_i}
\end{aligned}$$

Following the same geometrical derivation we have:

$$\begin{aligned}
\Delta\alpha^{out} &= -\Delta\alpha^{in} \\
\Delta x^{out} &= -\Delta x^{in} + 2\Delta d \sin\alpha_i \\
\Delta L^{mir} &= 2\Delta d \cos\alpha_i
\end{aligned} \tag{3.16}$$

It can be proven that all errors add together independently under small angle approximation. Proof is omitted. Therefore in general, when a beam with input angular error $\Delta\alpha$, transversal errorΔx and piston error ΔL reflects from a mirror M_1 with tilt error $\Delta\beta_i$ and piston error Δd_i, the resulting alignment errors upon reflection is:

$$\begin{aligned}
\Delta\alpha^{out} &= -(\Delta\alpha^{in} - 2\Delta\beta_i) \\
\Delta x^{out} &= -\Delta x^{in} + 2\Delta d \sin\alpha_i \\
\Delta L^{mir} &= 2\Delta d \cos\alpha_i
\end{aligned} \tag{3.17}$$

Free space propagation between two mirrors M_{i-1} and M_i is trivial under small-angle approximation as the following:

$$\begin{aligned}
&\Delta\alpha_i = \Delta\alpha_{i-1} \\
&\Delta x_i = \Delta x_{i-1} - L_{i-1,i}\ tan\Delta\alpha_{i-1} \approx \Delta x_{i-1} - L_{i-1,i}\Delta\alpha_{i-1} \\
&\Delta L_{i-1,i} = \frac{L_{i-1,i}}{cos\Delta\alpha_{i-1}} - L_{i-1,i} \approx \frac{1}{2} L_{i-1,i}(\Delta\alpha_{i-1})^2 \approx 0.
\end{aligned} \tag{3.18}$$

Figure 3.9: The beam propagation errors caused by free space propagation.

Now that we derived how alignment errors are generated and carried from a misaligned mirror and how they propagate in free-space, we can calculate the full roundtrip propagation in a N-mirror GTI cavity by breaking it down into N segments of propagation, where a single segment consists of propagating through 1 free space segment $L_{i-1,i}$ and reflecting from 1 mirror M_i. Combining [e.q.1] and [e.q.2] we have:

$$\begin{aligned}
\Delta\alpha_i &= -(\Delta\alpha_{i-1} - 2\Delta\beta_i) \\
\Delta x_i &= -\Delta x_{i-1} + L_{i-1,i}\Delta\alpha_{i-1} + 2\Delta d \sin\alpha_i \\
\Delta L_i &= 2\Delta d \cos\alpha_i
\end{aligned}$$

After roundtrip where the beam propagates back into the cavity, we have:

$$\Delta\alpha_N^{(1)} = (-1)^N[\Delta\alpha_N^{(0)} + 2\sum_{i=1}^{N-1}\Delta\beta_i(-1)^i]$$
$$\Delta x_N^{(1)} = (-1)^N[\Delta x_N^{(0)} - L_{cav}\Delta\alpha_N^{(0)} - \sum_{i=1}^{N-1}(-1)^i(2\Delta\beta_i L_{i,N} + 2\Delta d_i \sin\alpha_i)]$$
$$\Delta L_N^{(1)} = 2\sum_{i=1}^{N-1}\Delta d_i\cos\alpha_i + \Delta L_N^{(0)}$$

If after n rountrips, the beam propagates back into the cavity, then we have:

$$\Delta\alpha_N^{(n)} = (-1)^{nN}\Delta\alpha_0^{(0)} + 2\sum_{j=1}^{n}(-1)^{jN}\sum_{i=1}^{N-1}\Delta\beta_i(-1)^i$$
$$\begin{aligned}\Delta x_N^{(n)} &= (-1)^{nN}(\Delta x_0^{(0)} - nL_{cav}\Delta\alpha_0^{(0)}) \\ &\quad - \sum_{j=1}^{n}\sum_{i=1}^{N-1}(-1)^{jN}(-1)^i[2\Delta\beta_i(L_{i,N} + (j-1)L_c av) + 2\Delta d_i\sin\alpha_i)]\end{aligned}$$
$$\Delta L_N^{(n)} = 2n\sum_{i=1}^{N-1}\Delta d_i\cos\alpha_i + \Delta L_0^{(0)}$$

If the beam exits the cavity after n rountrips instead, then it goes through 1 less reflection at the partial reflecting mirror, which according to our definition of reference path has no alignment errors of any kind, therefore, compared with previous set of equations, $\Delta\alpha$ and Δx only switches sign:

$$\begin{aligned}\Delta\alpha_N^{out(n)} &= -(-1)^{nN}\Delta\alpha_0^{in} - 2\sum_{j=1}^{n}(-1)^{jN}\sum_{i=1}^{N-1}\Delta\beta_i(-1)^i \\ \Delta x_N^{out(n)} &= -(-1)^{nN}(\Delta x_0^{in} - nL_{cav}\Delta\alpha_0^{in}) \\ &\quad + \sum_{j=1}^{n}\sum_{i=1}^{N-1}(-1)^{jN}(-1)^i[2\Delta\beta_i(L_{i,N} + (j-1)L_{cav}) + 2\Delta d_i\sin\alpha_i)] \\ \Delta L_N^{out(n)} &= 2n\sum_{i=1}^{N-1}\Delta d_i\cos\alpha_i + \Delta L_0^{(0)}\end{aligned} \tag{3.22}$$

We can clearly observe that there are 3 contributions of error: input error, tilt error and piston error.

3.4.3 Optimization of computational speed

With the full mathematical description, a model is built and it has the following structure that close resembles that of a neural network in Fig. 3.10.

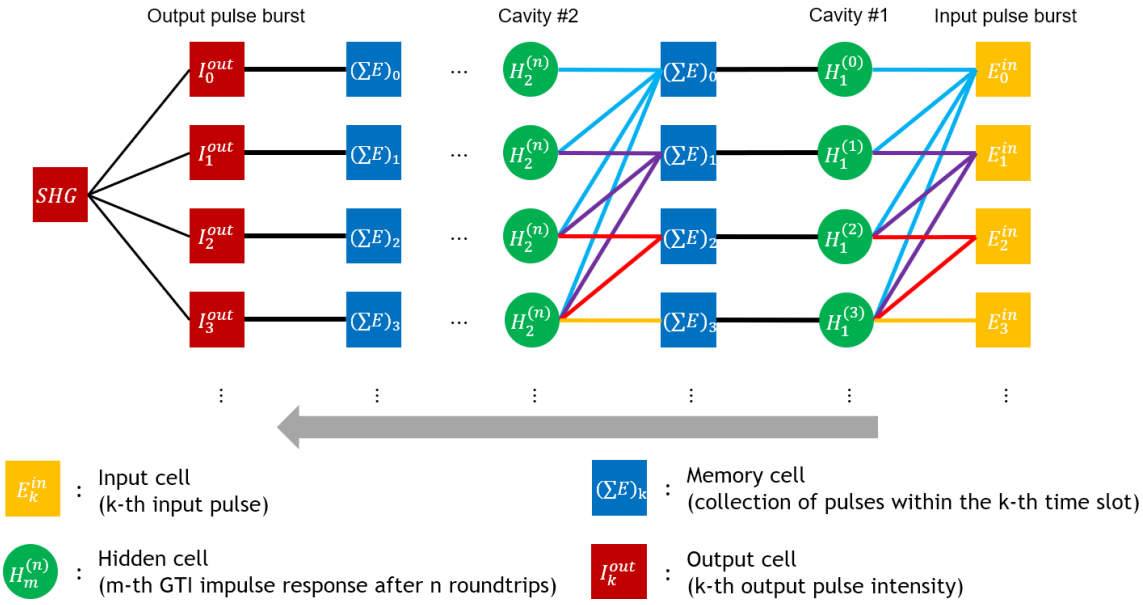

Figure 3.10: Mathematical model of coherent pulse stacking casted in a neural network form.

The input pulse burst can be expressed in a series of input cells that propagates through multiple layers of hidden cells, where each layer corresponds to a physical GTI cavity, and each node in a given hidden layer corresponds to different integer number of roundtrips in the GTI cavity. In between hidden layers, memory cells are placed to collect all pulses that falls into the same time slot, and as its size grows exponentially deeper in the network, memory cell size reduction need to take place to only carry the principal information forward. At the output of all hidden layers, each memory cell containing large number of subpulses each with their own amplitudes, phases, tilt errors, piston errors, transversal errors, and diffraction lengths shall be

integrated over time and space to obtain the collective intensity that is read by the photodetector. These intensities are further integrated into a single peak power read in the form of SHG, which is used to evaluate system performance and feed back into control parameters for the input cells and each hidden layer.

An order-of-magnitude analysis on time cost of the model quickly reveals the bottleneck in computational speed. Denote k as total number of output pulses, and m as total number of GTI cavities. The total number of operations required to propagate through all hidden and memory layers is $\mathcal{O}(k\binom{k+m-1}{m-1}m)$, and that of the last step of integration across all output memory cells is $\mathcal{O}(k\binom{k+m-1}{m-1}^2)$. Without any form of truncation or approximation, the last step alone takes an astronomical amount of time to calculate, up to 10,000 years for a single 81-pulse stacking simulation!

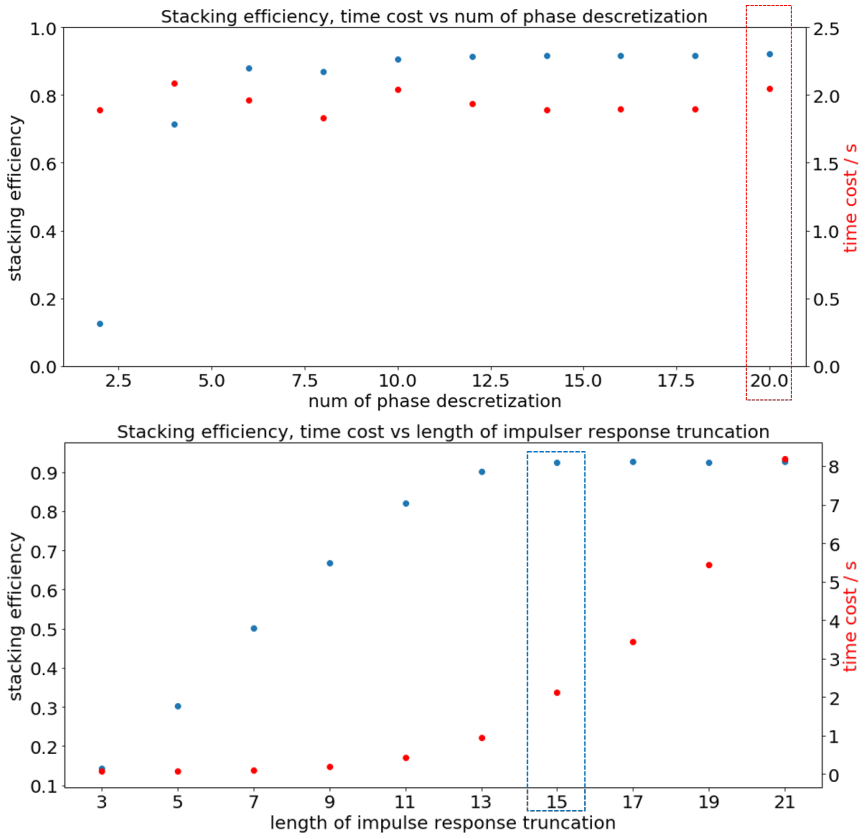

Figure 3.11: Time cost reduction via (up) reduction of memory cell size by discretizing phase space and (down) truncation of impulse response length. The dashed rectangles highlight the choice of discretization and truncation parameters that increases calculation speed by orders of magnitude at a cost of efficiency error of $< 1\%$.

With effort on discretization of phase space and temporal segments, truncation of impulse response and migration from scripting language to compiled language, a total time cost improvement of $\sim 10^{10}$ has been achieved, enabling an average time cost of $\sim 10s$ per simulation that scales roughly linearly with number of pulses instead of factoral.

3.4.4 Effect of alignment errors on stacking fidelity

Combining the theory of error propagation in GTI cavities with transfer matrix approach of coherent pulse stacking, we can now simulate the effects of alignment errors on stacking fidelity. Simulations on effects of tilt and piston errors on truncated 81-pulse stacking in 4+4 GTI cavities is demonstrated in Fig.3.12.

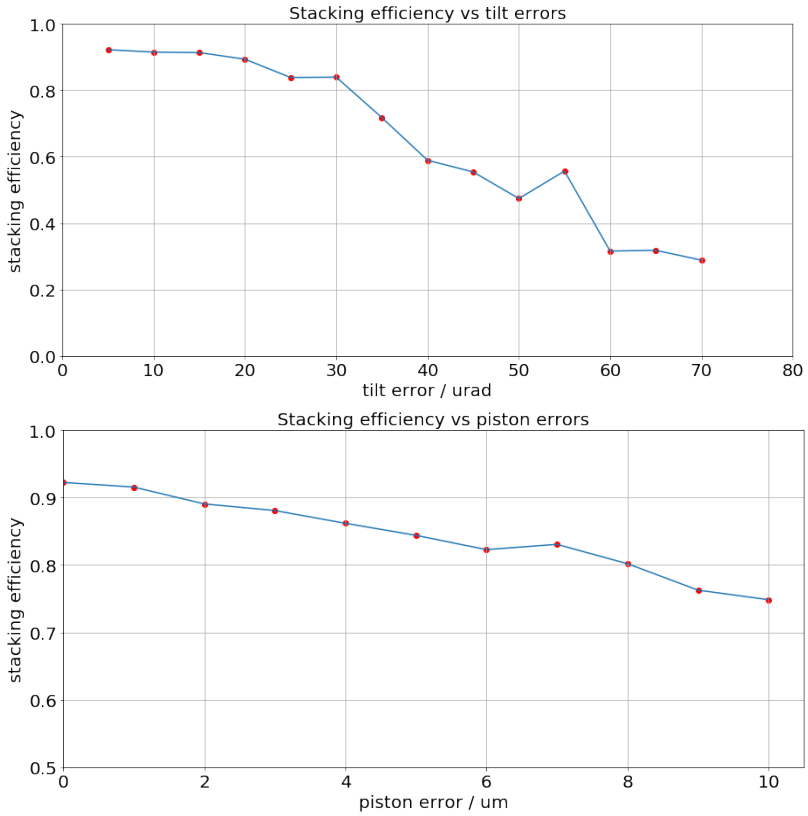

Figure 3.12: The stacking efficiency of truncated 81-pulse stacking in 4+4 cascade and multiplexed GTI cavities degrade with (up) tilt errors and (down) piston errors in GTI mirrors, averaged over 10 simulations for each condition.

The simulations show that in truncated setting, an optimal stacking efficiency of 91% can be obtained with a tilt error of $< 10\mu rad$ and a piston error of $< 1\mu m$. Note that the full-range cavity phases adjustment corresponds to a piston adjustment range of $1.03\mu m$, therefore if the piston error is controlled down to $< 1\mu m$, it will be considered completely eliminated. For ultra-broad bandwidth stacking, even cavity phase changes will result in measurable piston error effect that needs to considered both in simulation and in experiments.

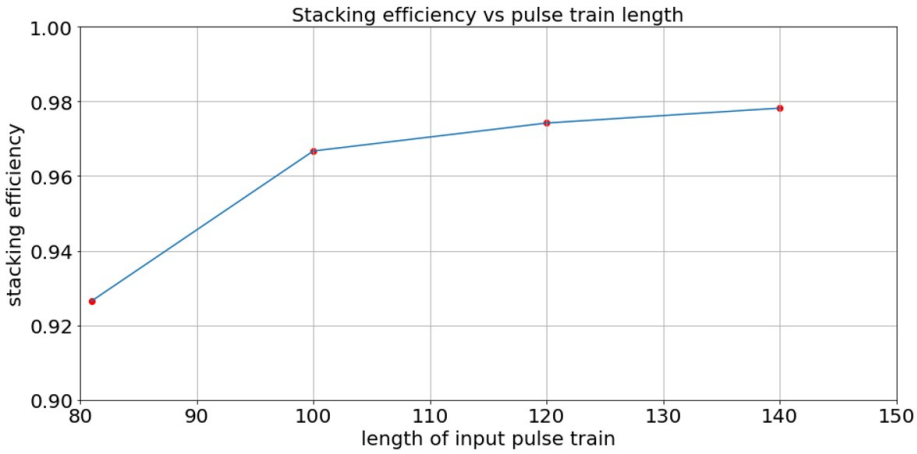

Figure 3.13: By launching longer reverse impulse response pulse train of 4+4 GTI, achievable stacking efficiency increases from 92.6% to 97.8%.

Extending the length of reverse impulse response pulse burst and sending it through 4+4 GTI set can increase achievable stacking efficiency limited by truncation, as shown in Fig. 3.13. It will be covered in the next section that it also allows for significant improvement of theoretically possible pre-pulse contrast from $15dB$ to up to $\sim 40dB$. While at the current stage the focus is on improving stacking efficiency and the CPSA system itself, the pre-pulse contrast detection and optimization is on the horizon, and the error analysis and optimization algorithms will serve as critical tools to develop a robust, high fidelity coherent combining system.

The impact of tilt errors and pistons errors on coherent stacking of an extended pulse train in 4+4 GTI cavities is depicted in Fig. 3.14. The degradation is comparable to that of the truncated stacking, and the requirements of controlling tilt errors

to $< 10\mu rad$ and piston error of $< 1\mu m$ remains valid.

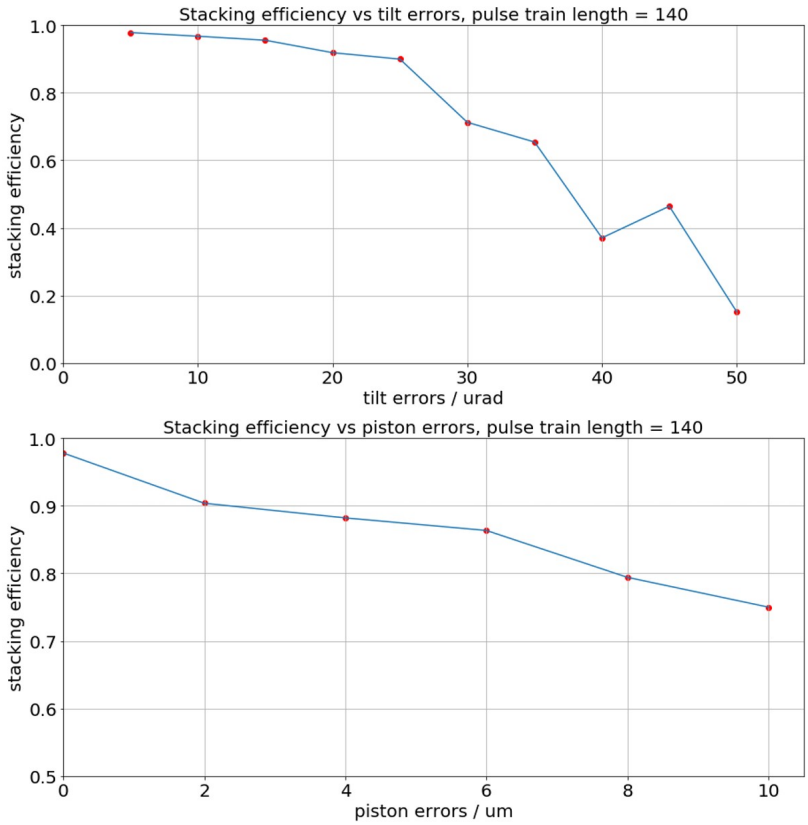

Figure 3.14: With an extended stacking sequence, fidelity degradation from tilt (middle) and piston (bottom) errors is comparable to truncated stacking scenario.

Experimentally, the alignment precision is determined by the alignment method and detection device resolution. The experimental conditions and their detection limits are presented in Table 3.1.

Cavity error type	Tilt error	Piston error
Criteria of alignment	Maximize beam overlap	Maximize spectral beating
Detection device	IR camera	Spectrometer
Detection limit	$10\mu m$	$20nm$
Corresponding error	$\sim 20\mu rad$	$\sim 5\mu m$
Achievable stack efficiency	87%	84%

Table 3.1: Experimental conditions for manual alignment of cavity mirrors

Given manual alignment limits, the model predicts that 81-pulse stacking effi-

ciency can only reach <75%. Experimentally, 81-pulse stacking efficiency can only be repeatedly achieved at <70%. The simulation also reveals that piston error is the biggest bottleneck, and its elimination is at top priority. A high-precision stacking technique is required to improve from here.

3.4.5 High-precision stacker alignment procedure

To meet the demand of controlling piston errors and tilt errors to obtain at least 90% stacking efficiency, a high-precision stacking technique has been developed based on the error analysis. The main procedure breaks down to two aspects. Piston error is eliminated by scan broad range of PZT motion in each GTI cavity to retrieve spectral beating and peak detection curve and find the optimal piston position accordingly. Tilt error is reduced by self-optimizing individual knob controls on top of manual alignment, and potentially adaptively control during stacking stabilization to further optimize mirror tilts.

To start with, each GTI cavity is manually aligned using CMOS camera, spectrometers and sampling oscilloscopes, using an iterative approach to align for mirror tilt and piston until the manual adjustment precision limit is reached. At this stage, given the tilt error precision of $\sim 20\mu rad$ and piston error precision of $\sim 5\mu m$, these two types of errors are still coupled.

Following manual alignments, individual cavities are further fine tuned using FPGA-controlled algorithms. GTI cavities are unblocked one at a time, 1-cav stacking sequence is released to launch a pulse burst into the cavity. First, tilt-optimizer algorithm is released to correct for tilt errors based on feedback signal from peak detection, as shown in Fig. 3.15. Mirror center of mass spatial position was maintained unmoved by cancelling out tilt-induced piston motion in the algorithm.

Then, a long-range PZT scanning in each GTI cavity is performed while a 1-cav stacking sequence is in place. This creates the full peak power vs cavity piston curve,

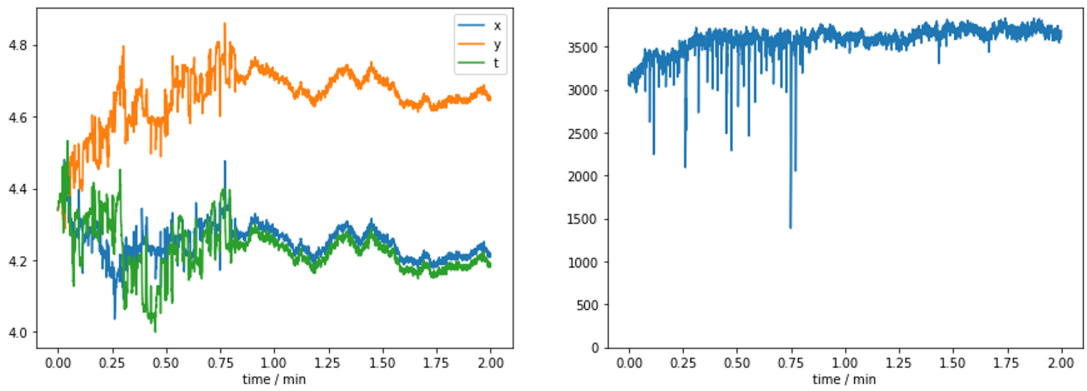

Figure 3.15: Experimental illustration of mirror tilt self-alignment in a single GTI cavity. (Left) voltages applied to each PZT mirror knob; (Right) convergence to optimized mirror position as characterized by stacked peak power.

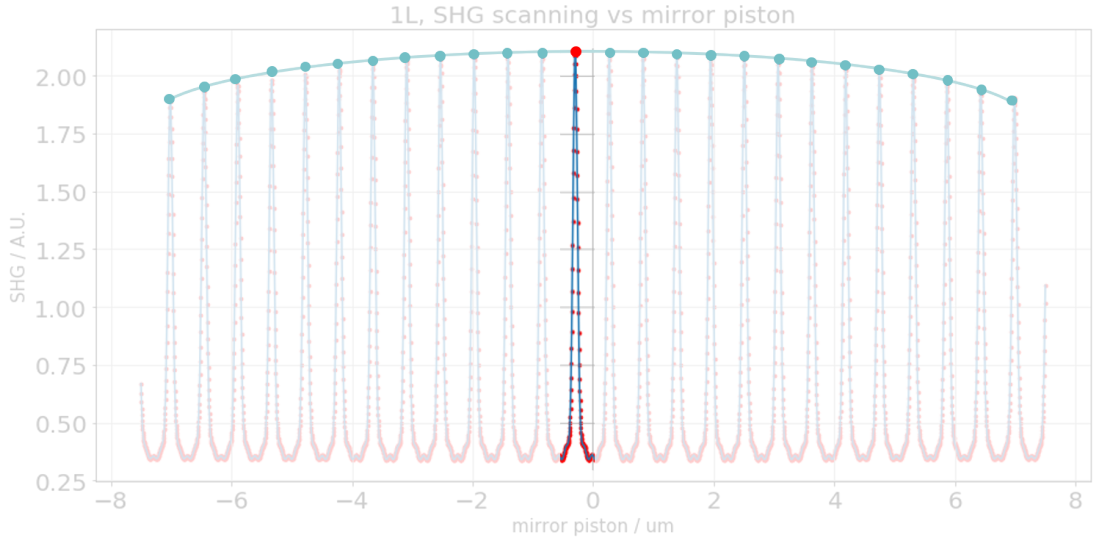

Figure 3.16: Full-range PZT motion scans the cavity roundtrip length by $\sim 30\mu m$. A mirror position that gives optimal cavity roundtrip length can be obtained.

from which optimal cavity roundtrip length can be retrieved. An alternative approach is to perform the same cavity scan but analyze spectral beating pattern instead. The exact choice of metric function is determined by the detection limit and the achievable resolution. At this stage, tilt error is minimized and piston error is eliminated, and all cavities can be unblocked to perform the stacking experiment.

This technique is built based on the following assumptions. First, tilt errors and piston errors are decoupled within $1\mu m$ of PZT motion. Second, the system provides

long-term stability in that mirror positions and input pulse train characteristics do not change over time. It is also required that all PZT knobs have identical and linear response, but realistically their voltage response can be different, and hysteresis can cause cavities to build up alignment errors over time. Therefore further development of the technique and automated processes shall consider these corrections during stacking operation.

3.5 Adaptive optimization control

We have discussed that the uncertainties in the CPSA system prevents the exact prescription of the pulse burst upfront to achieve high fidelity stacking. Due to the flexibility to modify modulation signal enabled by FPGA controls, we can adaptively change EOM modulations to compensate for system uncertainties. Here we implement a two-loop SPGD algorithm to take care of both stabilization and optimization, and we prove that the system performance increases over time using this approach.

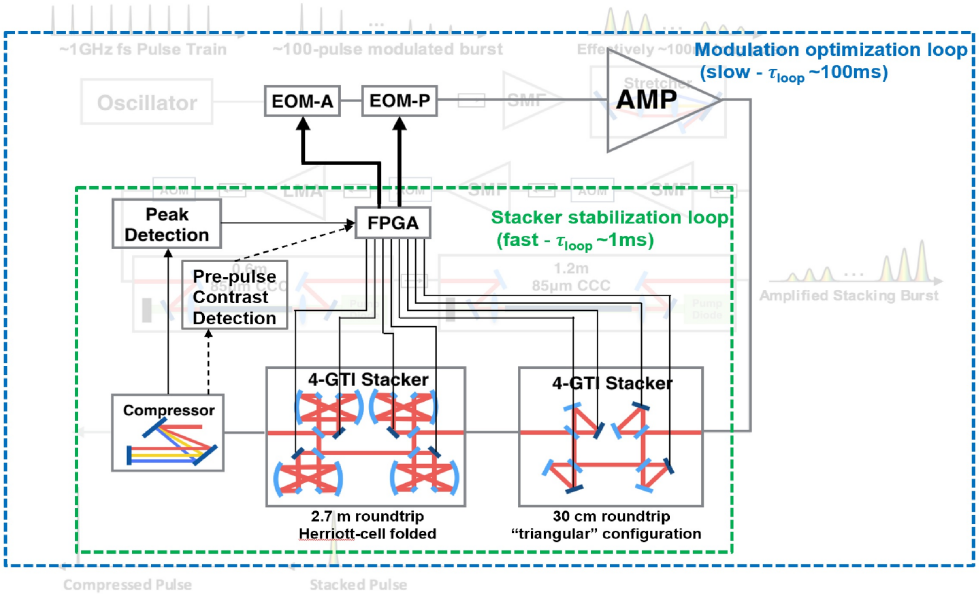

Figure 3.17: Adaptive stabilization and optimization using two-loop SPGD algorithm.

As shown in Fig.3.17, the inner loop constantly stabilizes the coherent pulse stack-

ing by adjusting GTI cavity phases through PZT mirrors, and it is running at 100Hz - 1kHz loop speed to compensate for phase drifting and slow phase noises. On top of that, the outer loop adjusts the pulse burst modulation and evaluate the corresponding stacked pulse peak power to improve upon, and this loop runs at two orders of magnitude slower speed than the inner loop to allow stabilization algorithm to converge, since only the stabilized peak power reading provides one valid data point for the optimization loop. The exact algorithm is described below:

Algorithm 2: Two-loop SPGD algorithm for CPSA stabilization and optimization.

---

initialize pulse burst modulation ${}^0\vec{\psi}$, specify perturbation depth d, gain g;

repeat

  repeat

    measure peak power $J({}^k\vec{\delta})$;

    perturb cavity phases randomly by ${}^k\Delta\vec{\delta} = \Delta\delta_{random}d$;

    measure peak power $J({}^k\vec{\delta} + {}^k\Delta\vec{\delta})$;

    change cavity phase to ${}^{k+1}\vec{\delta} = {}^k\vec{\delta} + g\frac{J({}^k\vec{\delta}+{}^k\Delta\vec{\delta})-J({}^k\vec{\delta})}{J({}^k\vec{\delta}+{}^k\Delta\vec{\delta})}{}^k\Delta\vec{\delta}$; n++

  until *stabilized*;

  measure peak power $J(\vec{\psi})$;

  if *modulation updated* **then**

    perturb pulse burst modulation randomly by ${}^n\Delta\vec{\psi} = \Delta\hat{\psi}_{random}d$;

  else

    change pulse burst modulation to ${}^{n+1}\vec{\psi} = {}^n\vec{\psi} + g\frac{J({}^n\vec{\psi}+{}^n\Delta\vec{\psi})-J({}^n\vec{\psi})}{J({}^n\vec{\psi}+{}^n\Delta\vec{\psi})}{}^n\Delta\vec{\psi}$;

  end

  n++;

until *optimized*;

Simulation of the two-loop optimization algorithm as shown in Fig.3.17 have

demonstrated that starting with loading a non-optimized stacking profile that yields 50% of theoretically expected optimum stacking efficiency, it converges to an optimized stacking profile that yields >95% of the theoretically expected optimum efficiency. The convergence speed is dependent on the number of pulses to be stacked: assuming that stabilization of 4-GTI cavities takes ∼500 fast loop actions or ∼0.5s and stabilization of 4+4 GTI cavities takes ∼1000 fast loop actions or ∼1s, then the estimated convergence time for the two cases are ∼5min and ∼30min, respectively. This requires that during this period of time, the CPSA system runs without any uncompensated drifts to reach convergence in the end.

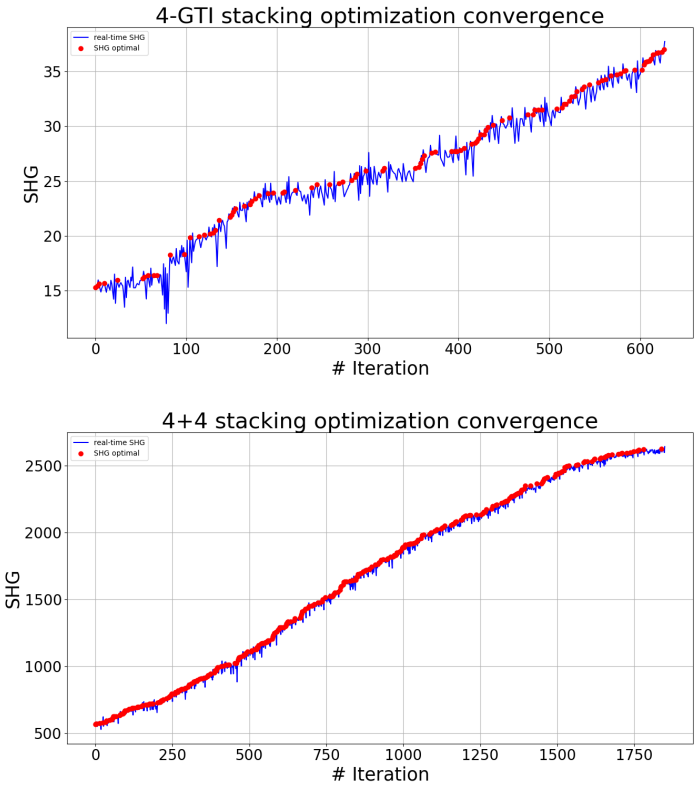

Figure 3.18: Convergence of two-loop optimization algorithm in (up) 9-pulse, 4-GTI stacking and (down) 81-pulse, 8-GTI stacking.

Another key feature enabled by extended pulse train and its optimization is high pre-pulse contrast. The basic idea is to engineer post pulses to enable arbitrarily high pre-pulse contrast for any arbitrarily-prescribed stacking profile, at a cost of

sacrificing stacking efficiency by a small amount, as shown in Fig. 3.19.

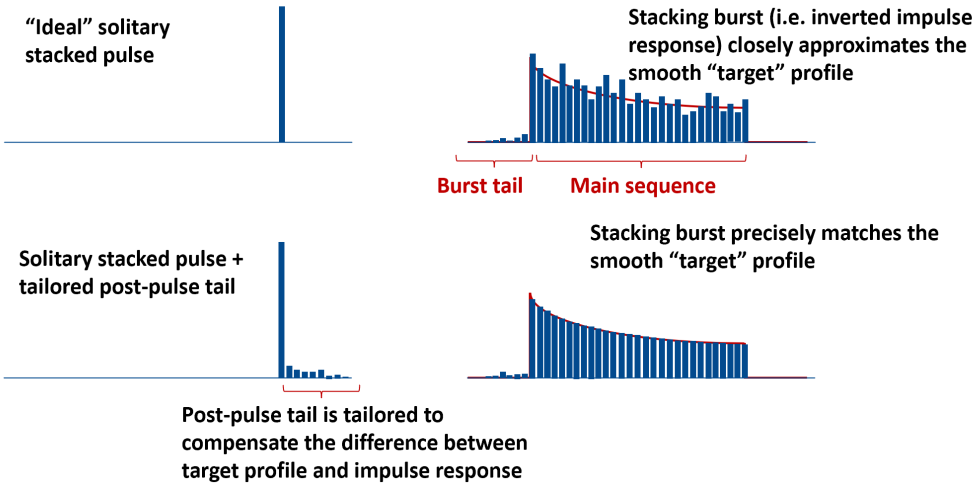

Figure 3.19: Demonstration of increasing pre-pulse contrast via post-pulse control [9].

3.6 Effects of GTI cavity layout designs on CPSA

The physical design of GTI cavities need to consider both supporting high efficiency stacking and compact overall footprint. As the number of pulses increases, the longer GTI cavities need to be folded one way or another. One common approach is to use Herriott-cell beam folding, which involves curved mirrors, as depicted in Fig. 3.20.

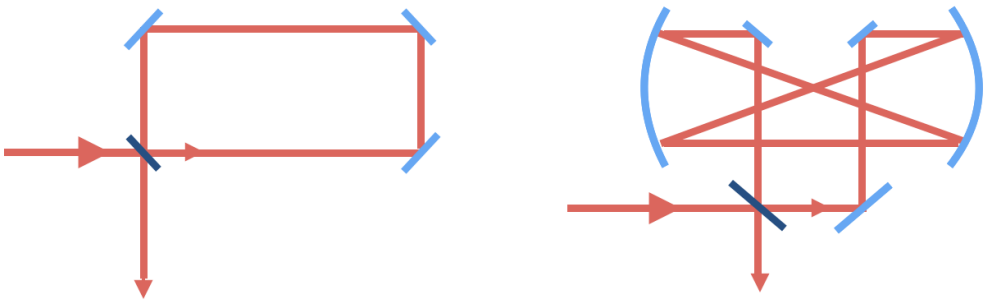

Figure 3.20: Schematic of a GTI cavity based on (left) flat mirrors with no beam folding and (b) Herriott cell design with curved mirrors and beam folding.

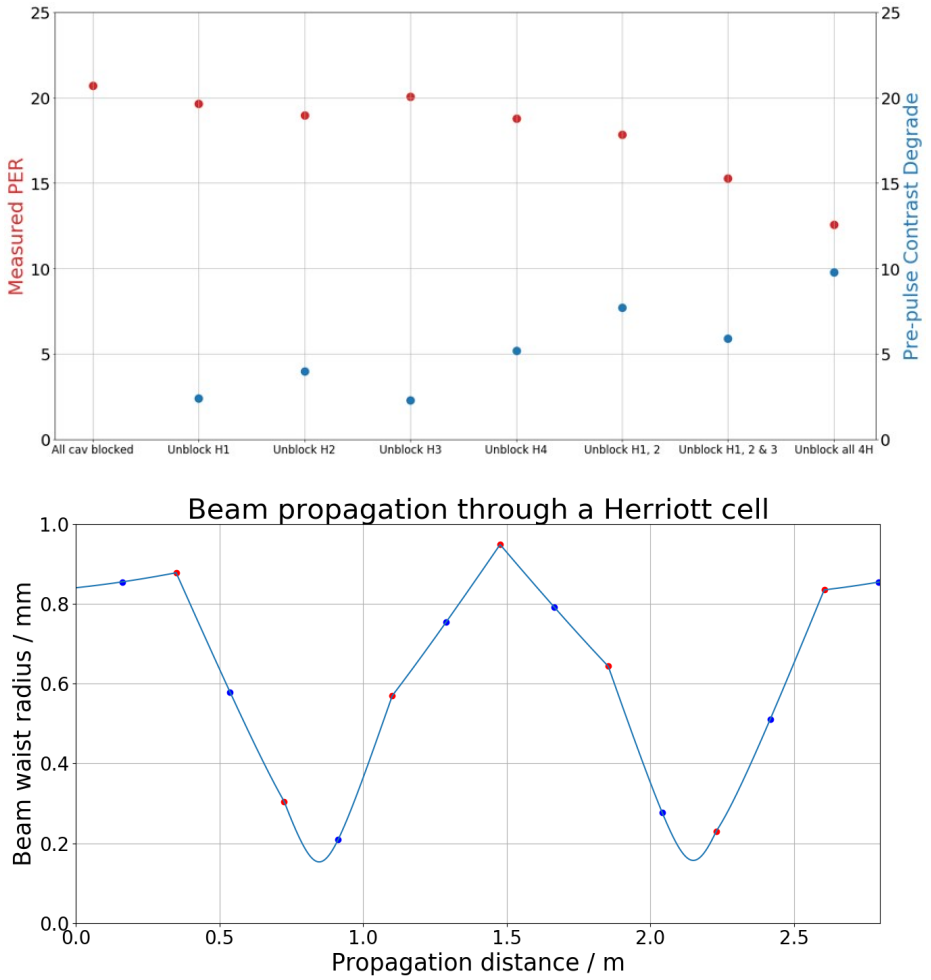

Figure 3.21: Herriott cell design in a GTI cavity design has drawbacks on (up) experimentally measured polarization degradation and (bottom) beam size variation as the Gaussian beam propagates through the cavity.

While Herriott cells have very compact footprint per single cavity, they suffer from polarization rotation per roundtrip that degrades achievable stacking fidelity, and at the same time its beam path focuses and defocuses multiple times per roundtrip as illustrated in Fig. 3.21, which reduces spot size on the mirror surface and requires higher damage threshold mirrors to tolerate high energy pulses. Therefore a new physical layout design based on flat mirrors is developed in Fig. 3.22. It has comparable overall physical footprint than 4+4 GTI design with Herriott-cells while eliminating polarization rotation.

Table 3.2 shows that given same roundtrip length, a flat-mirror GTI is compatible

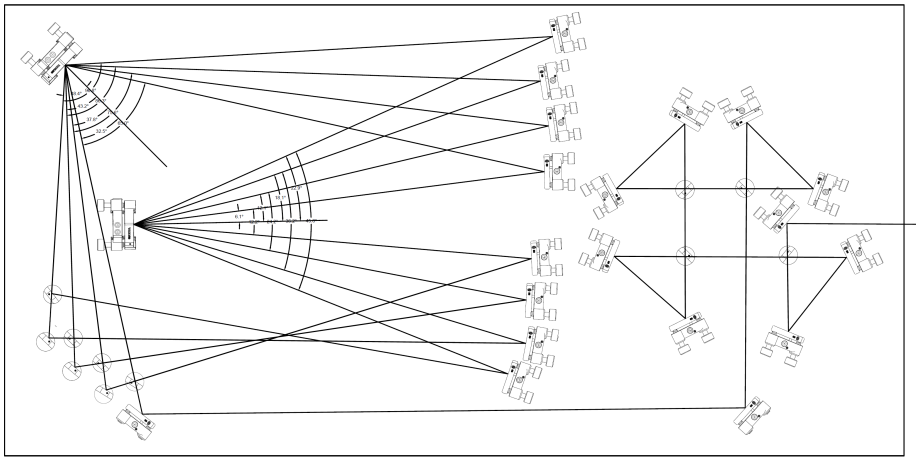

Figure 3.22: A 4+4 GTI layout design based on flat mirrors.

with a much larger beam size and correspondingly higher energy capability. Here the damage threshold requirement is calculated assuming 100mJ input burst energy, and the current damage threshold is calculated based on BB1-EO3 with damage threshold specification of 0.5 J/cm^2 (1064 nm, 10 ns, 10 Hz, spot diameter 0.433 mm). It is worth noting that Herriott cell remains a space-efficient solution to a long cavity design, and further scaling of the current coherent pulse stacking system may utilize the accumulated knowledge base on Herriott cell eigenmodes and other key properties.

	9-ns flat-mirror GTI	9-ns Herriott-cell GTI
Beam diameter (at waist)	5.8 mm	Down to 0.4 mm
Required Damage threshold	0.04 J/cm^2	Up to 4.0 J/cm^2
Current damage threshold	0.5 J/cm^2	

Table 3.2: Damage threshold requirements in two different GTI cavity designs

3.7 Experimental setup and results

The experimental setup is demonstrated in Fig.3.23. The NPE oscillator produces pulses with $68fs$ transform-limited pulse duration and $28nm$ bandwidth at the repetition rate of $\sim 1GHz$ [33]. These pulses first propagate through FPGA-

controlled amplitude and phase EOMs to be carved into bursts of 81 pulses, then they are stretched to ∼1ns pulses in the stretcher with 9nm spectral bandwidth. At this point, the pulses overlap into each other to produce an effectively-long 81ns pulse that propagates through several SMF fiber amplifiers and an AOM to be downcounted and amplified with amplified burst energy of $4\mu J$ before entering the GTI cavity set. The GTI cavities are designed such that their roundtrip length equals integer times that of the oscillator, and let's define that integer as m. The GTI cavity set consists of four $m = 1$ GTIs and four $m = 9$ GTIs in a cascading and multiplexing configuration, and in each cavity there is one PZT-mirror whose 3 knobs are controlled independently by the FPGA to control cavity phases and enable piston and tilt motions with 16-bit resolution.

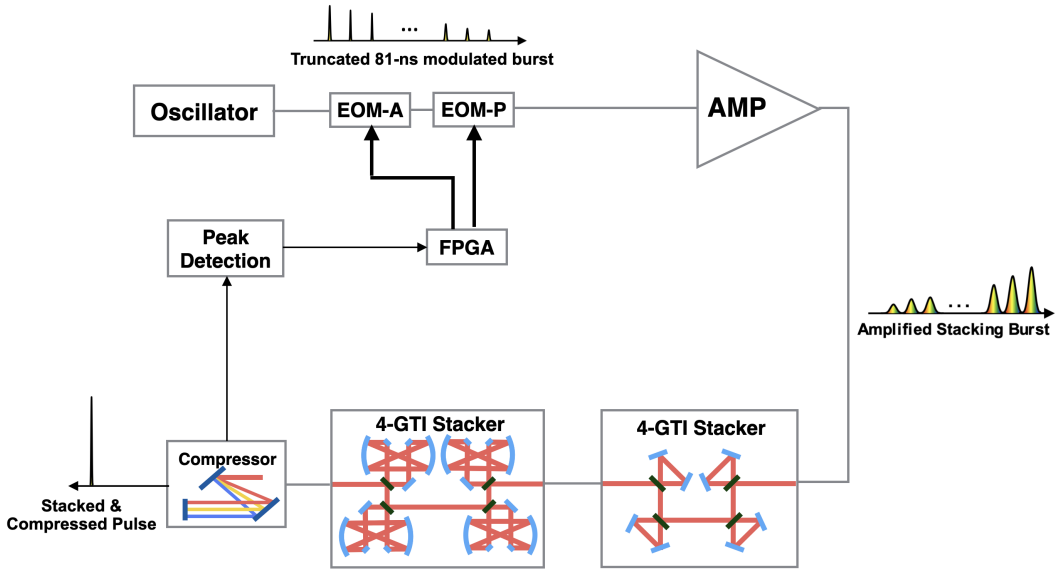

Figure 3.23: Schematic of experimental setup of 81-pulse coherent pulse stacking with stabilization and optimization.

After the burst of pulses is stacked into a single pulse through interference in the GTI cavity set, it is compressed into a femtosecond pulse and generates second harmonic signal through BBO crystal, which is monitored by the FPGA as the merit function both for stabilization and optimization. FPGA control system was developed with collaborative effort to adjust key CPSA system parameter including pulse

modulations and GTI cavities [34], and is continuously further developed with more high-precision control functionalities.

Since the combination of cavity phases to stack 81 pulses is in 8-dimensional phase space with $\sim 100mrad$ width in each dimension. A direct search in 8-dimensional phase space will encounter the "curse of dimensionality" and will take up to a few hours to find a single set of valid parameters. Taking advantage of long-term phase stability in the system, a 2-stage Lissajous scan is dispatched to lower the phase-searching time to $\sim 1min$, as shown in Fig. 3.24.

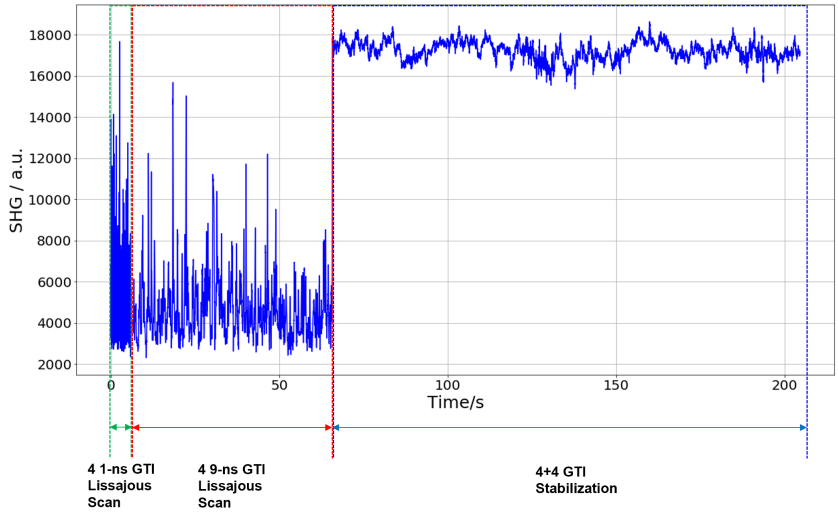

Figure 3.24: Experimental demonstration of 2-stage Lissajous scan retrieving the combination of cavity phases to stack 81 pulses in $\sim 1min$.

A two-loop stabilization/optimization algorithm is implemented as described in the previous section to control both cavity phases and pulse burst modulation. 24 PZT knobs in the 8 GTI cavities are simultaneously controlled to stabilize the pulse stacking, and a long-term stability of $\sigma = 1.4\%$ peak power rms was achieved in over 10 minutes. Stacking efficiency of 70.5% was obtained.

At time of this particular experiment, with the help of high precision stacking technique, the tilt error has been improved to $\sim 10\mu rad$, and piston error has been reduced to $\sim 3\mu m$. However, the oscillator repetition rate is not actively stabilized,

and it is experimentally measured to be drifting at $\sim 10kHz$ or $\sim 250nm$ in oscillator cavity length. Taking all these experimentally conditions into the model yields an average achievable stacking efficiency of 76%. Due to drifting oscillator f_{ref} and EOM bias voltage affecting the absolute reading of peak power detection over time, the optimization algorithm could not be run more than 5min and is not long enough to improve on the phase modulation, so in this recorded stacked pulse trace a burst of pulses with manually input phases are stacked in its as-is condition.

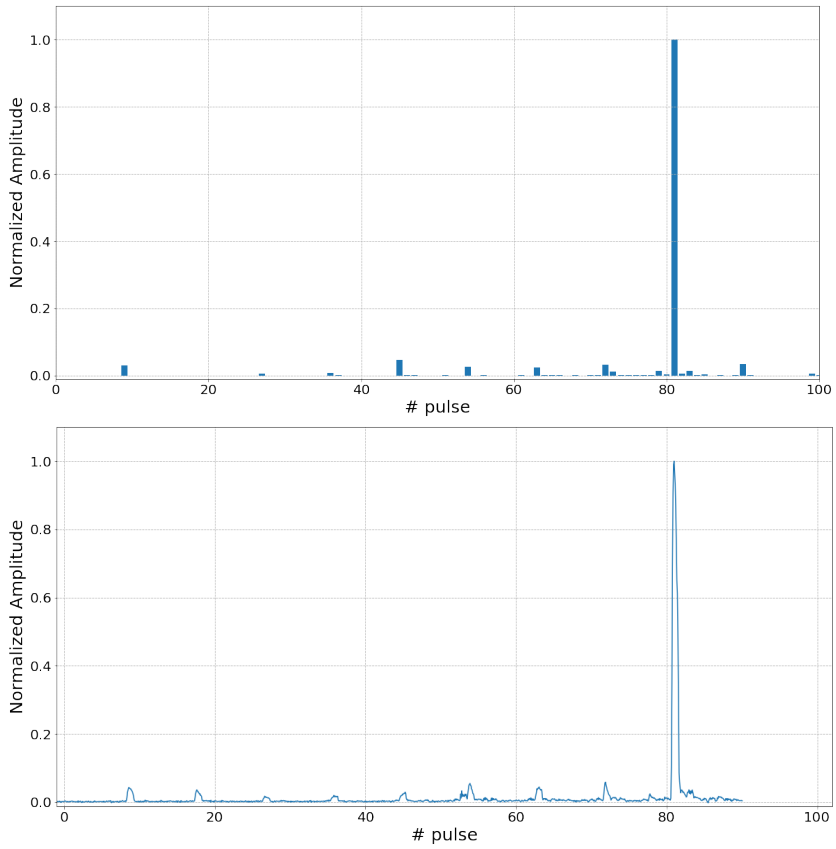

Figure 3.25: Stacked pulse train of 81-pulse coherent pulse stacking with stabilization in (up) simulated experimental condition that predicts 76% stacking efficiency and in (down) experimental result that measures 70.5%.

This result can be further improved with stabilized oscillator f_{rep} to eliminate free-drifting induced effective piston errors, further improvement on experimental piston error detection resolution, and optimization of the stacking burst modulation. The model predicts that with oscillator drifting eliminated and piston error reduced to

$\pm 1\mu m$, the stacking efficiency would improve to 85%, and complete elimination of piston error would further improve it to 90%.

CHAPTER IV

Near Complete Energy Extraction in 85μm core CCC Fiber Amplifier Using Coherent Pulse Stacking Amplification

4.1 Introduction

The scalability of an LPA collider driver architecture based on coherent temporal and spatial combining of fiber arrays is determined by the achievable pulse energy per parallel channel. The energy scaling from each fiber amplifier channel is limited by both transversal mode size in fiber and pulse duration. Correspondingly, the design of these parallel fiber amplifier arrays need to sufficiently scale in both mode field diameter and in effective pulse duration to deliver high energy pulses at the output with low nonlinearity.

As shown in Fig.4.1, given two typical mode field areas in large-core fibers along with the nonlinearity limits, self-focusing thresholds and optical damage thresholds, and assuming a small signal gain of $G_0 = 1000$, the energy extraction from fiber amplifiers is limited by the B-integral for shorter pulse durations and by the stored energy for larger pulse durations, before optical damage thresholds or self-focusing limits are reached [28]. With traditional grating-based stretchers and compressors, chirped pulse amplification can stretch an ultrashort pulse to $\sim 1ns$ pulsewidth with

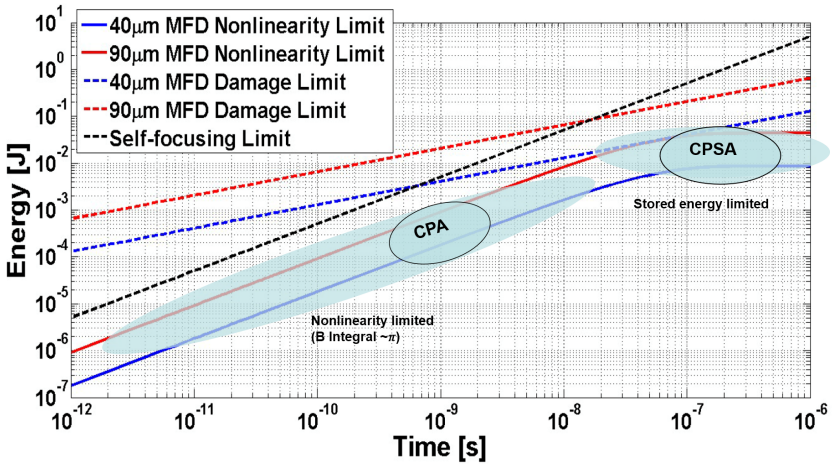

Figure 4.1: Energy scaling and limitations in fiber CPA and CPSA [28].

a 10cm grating. It scales linearly such that obtaining a $\sim 100ns$ long chirped pulse requires a 10m grating which is beyond practical manufacturing capabilities. Instead, the $\sim 100ns$ can be achieved via the coherent pulse stacking amplification technique.

CPSA is an "add-on" to FCPA, in that it produces stacking-pulse burst before the CPA amplifier, and then stacks this burst at the system output (either before or after the pulse compressor). CPSA is compactly implemented at the front of a system by "carving out" the required amplitude and phase profile of the stacking-pulse burst directly from a high repetition rate mode-locked oscillator, using a pair of fiber-pigtailed fast EO modulators. At the end of the system pulse stacking is achieved in a free-space arrangement of roundtrip-stabilized GTIs, each consisting of partially reflecting and HR mirrors. This architecture allows to completely control the amplified stacking-pulse burst amplitude profile, and to completely pre-compensate even severe energy-saturation effects in an amplifier, as well as to optimize and minimize the induced nonlinear phase.

4.2 Large-core Chirally-Coupled-Core fiber

It has been established that fibers used in power amplifiers arrays need to support large mode area, high output beam quality, high stored energy, and monolithic integration capabilities. Large-core Chirally-Coupled-Core (CCC) fiber is the key component in our high energy fiber amplifiers to amplify pulse bursts to $> 10mJ$ level.

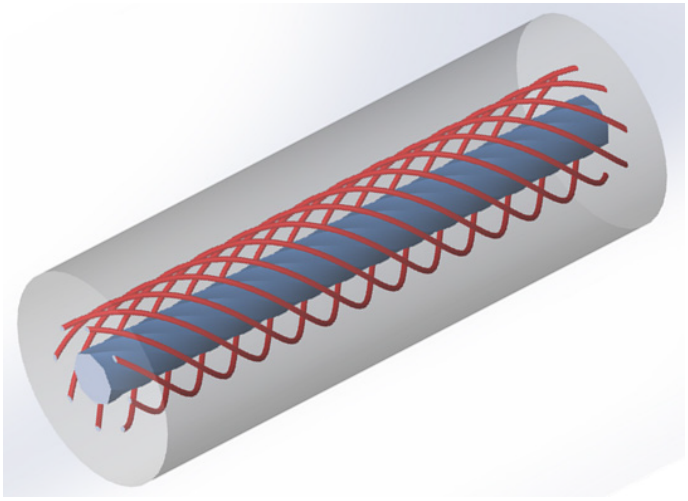

Figure 4.2: Polygonal-CCC fiber contains a polygonal-shaped on-axis central core and side cores positioned at the corners of the polygon [35].

CCC fibers are categorized as effectively single mode fibers, which selective leak higher order modes from the fiber core into its cladding, while transmitting the fundamental mode with a small loss at < 1 dB/m. The key structure of a large-core CCC fiber consists of an on-axis central core and several side cores that helically spin around the central core, as shown in Fig.4.2. CCC fiber has the following key advantages:

(1). **Effectively single mode**. The helically-perturbed structure couples all central core higher order modes (HOMs) into cladding, while preserving the fundamental mode at a practically negligible loss [35, 36]. This prevents degradation of pulse quality due to modal interactions and ensures good beam quality at the output

of the fiber.

(2). **Low ASE**. Since CCC fiber suppresses higher order modes, the spontaneous emission is only captured by the fundamental mode. Therefore amplified spontaneous emission (ASE) in CCC is much lower as compared to same-size core multi-mode fibers. This prevents inter-burst ASE from building up.

(3). **High stored energy**. Reduced ASE facilitates higher inverted-ion population of the fiber and thus more stored energy compared to multi-mode fibers.

(4). **Flexible and all-glass**. The flexible nature of CCC fiber enables monolithic integration and robust operation, especially as compared to rod materials like photonic crystal fiber (PCF).

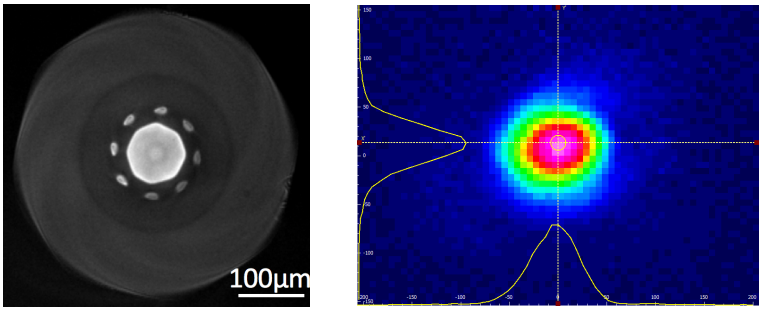

Figure 4.3: (Left) Section view of a $85\mu m$ core CCC fiber and (right) its output mode.

The particular CCC fiber we use in our experiments is a $85\mu m$ core CCC fiber. Its intersection and output mode is shown in Fig.4.3. The exact fiber and mode parameters are given in Table 4.1.

Core diameter	$85\mu m$
Cladding diameter	$400\mu m$
Cladding NA	0.45
Core NA	0.067
# side cores	8
MFD @ $1.03\mu m$	$42.5\mu m$

Table 4.1: CCC fiber parameters

4.3 Optimum stacking profile envelope shape

The nonlinear phase shift in an amplifier can be expressed a B-integral

$$B = \frac{2\pi}{\lambda} \int n_2 I(z) dz.$$

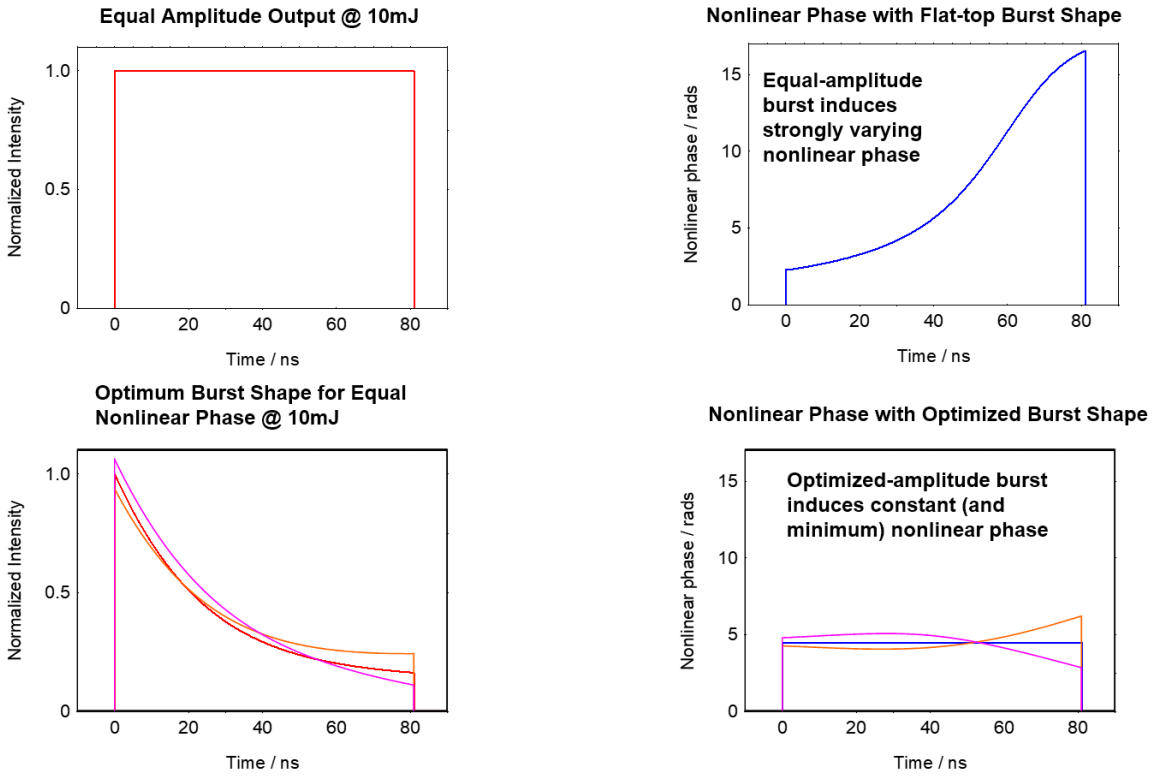

Figure 4.4: Optimum pulse burst envelope shape for equal nonlinearity [37]. The pink and orange curves in the lower graphs demonstrate that deviation from the optimum burst shape results in non-flat nonlinear phase across the burst and hence degrades stacking fidelity.

Due to saturation effects in a fiber amplifier, the front pulses of the burst will deplete gain and lower the gain for the back pulses of the burst. For individual pulses, the nonlinear phase can be expressed as

$$\phi_{NL} = \frac{2n_2 L_{\text{eff}}}{\lambda_c w_0^2} P_{peak},$$

$$L_{\text{eff}} = \frac{1 - e^{-\alpha L}}{\alpha},$$

where w_0 denotes effective mode radius and L_{eff} denotes effective propagation length in the gain medium. If the pulses are equal amplitude at the fiber amplifier output, they will therefore accumulate different nonlinear phases as the front of the burst has lower effective length. To ensure flat nonlinear phase across the burst, the burst envelope needs to be carefully carved, as shown in Fig.4.4.

4.4 Experimental setup and results

The experimental setup is shown in Fig.4.5.

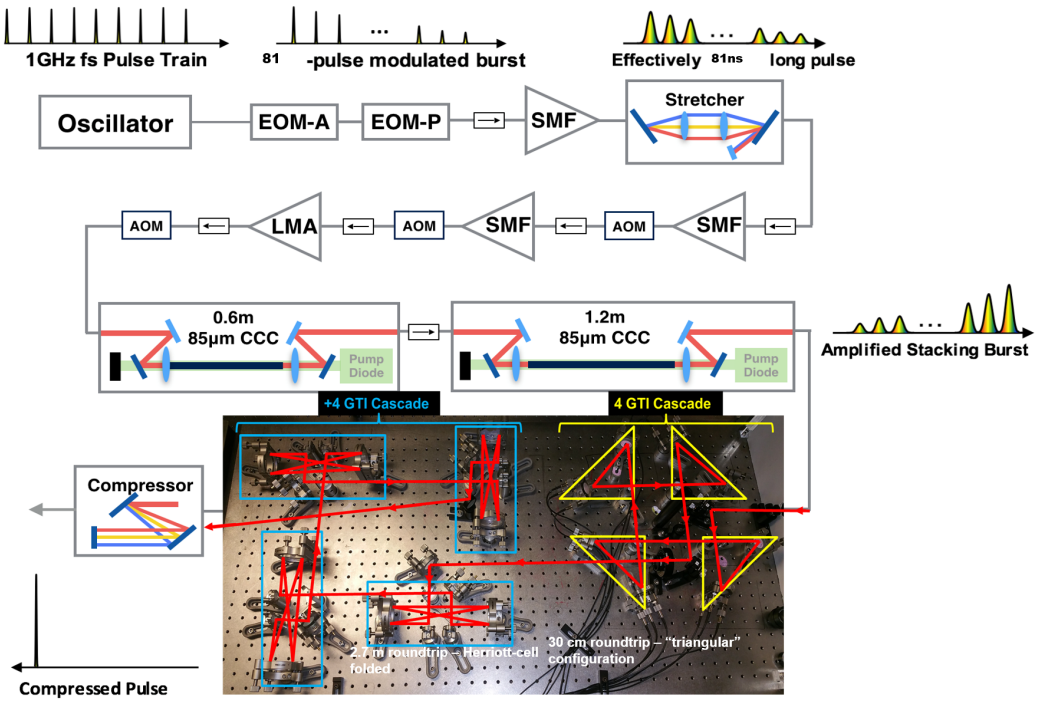

Figure 4.5: Experimental setup of the Coherent Pulse Stacking Amplification system based on Yb-doped 85μm core CCC fibers

In our experimental implementation we use a 1 GHz repetition rate mode-locked fiber oscillator. The corresponding repetition period of 1ns matches the stretched-pulse duration of slightly less than 1ns from a conventional 10-cm diffraction-grating based pulse stretcher. Such matching allows minimizing the required GTI stacker round-trip lengths, and maximizing their compactness and robustness. Therefore,

the 81-pulse stacking burst used in this CPSA implementation corresponds (after the stretcher) to a quasi-continuous 81ns pulse. This burst is amplified in a chain of single-mode fiber pre-amplifiers, followed by an Yb-doped $25\mu m$ core PM-LMA fiber pre-amplifier, and two Yb-doped $85\mu m$ core CCC fiber amplifiers. AOM gates between the stages suppress the ASE buildup, and control the burst repetition rate. The amplified pulse burst then propagates through a set of 4+4 multiplexed GTI cavities consisting of 4 sets of 1ns-roundtrip cavities followed by 4 sets of 9-ns roundtrip cavities to coherently stack into a single pulse and be compressed to femtosecond pulsewidth using diffraction-grating pulse compressor. The cavities are stabilized using FPGA-based SPGD algorithm, which maximizes the stacked-pulse peak power by constantly adjusting cavity lengths via PZT mirrors [37].

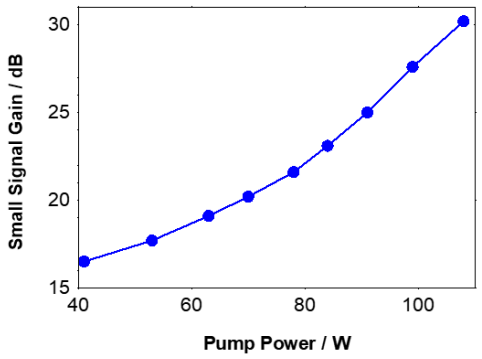

(a) Small signal gain vs pump power

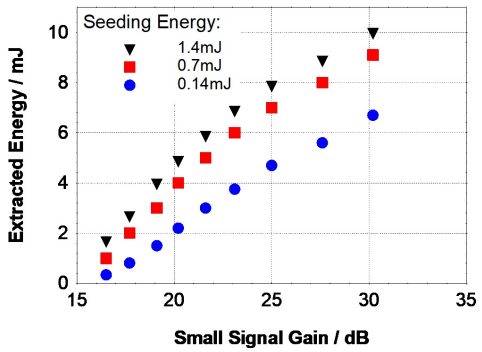

(b) Output energy vs small signal gain

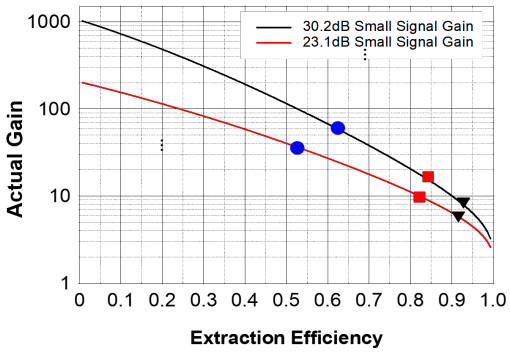

(c) Gain vs extraction efficiency

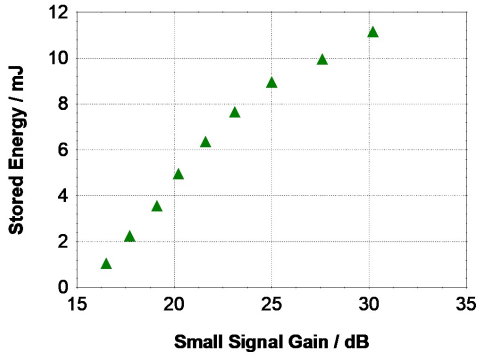

(d) Stored energy vs small signal gain

Figure 4.6: Energy storage and extraction measurements in $85\mu m$ CCC fiber.

The energy extraction results are shown in Fig. 4.6. By measuring small-signal gain G_0 at different pump powers, and the corresponding large-signal gains for different seed energies, we were able to use the Frantz-Nodvik model to relate G_0 to the stored fiber-amplifier energy. Fig. 4.6a shows measured small-signal gain as a function of pump power for a 1.2m long $85\mu m$ core Yb-doped CCC fiber (with 400 μm pump cladding). Fig. 4.6b shows amplified pulse-burst energy as a function of small signal gain. Knowing the small signal gain at a given pump power level and the actual pulse burst amplification gain under the same condition, we applied Frantz-Nodvik equations in Fig. 4.6c to effectively measure the stored energies as a function of small signal gain in Fig. 4.6d. It is evident from this that 10mJ extraction (at the 108W pump power) corresponds to 11mJ stored and thus to ∼90% extraction efficiency.

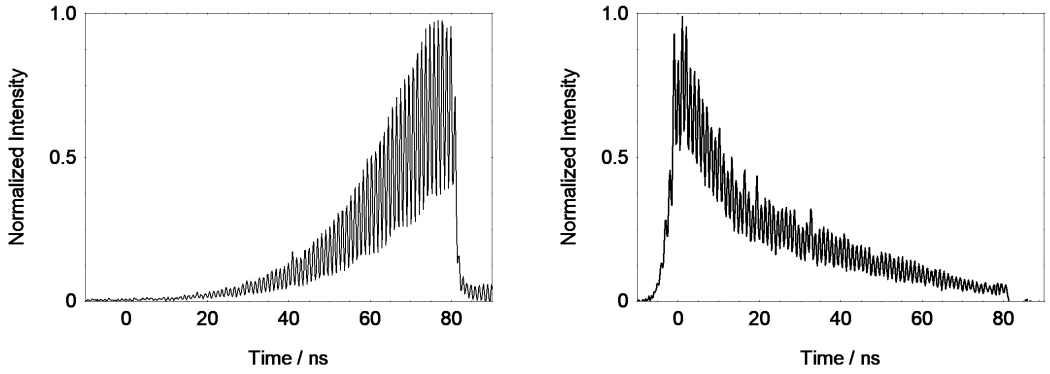

(a) Input burst (b) Output burst @ 10mJ

Figure 4.7: Gain saturation effect in CPSA [37].

This leads to extreme amplifier saturation. Pre-compensation was achieved by the 81-pulse stacking burst profile having the in-burst front-to-tail contrast of ∼30dB. The shape of this profile was numerically calculated to equalize the nonlinear phase shift between all the pulses, and it accounts that the burst front has an effectively shorter propagation distance and less accumulated nonlinear phase than the burst back, since the front sees significantly more gain.

The amplified multi-mJ burst of 81 pulses is coherently stacked into one pulse in

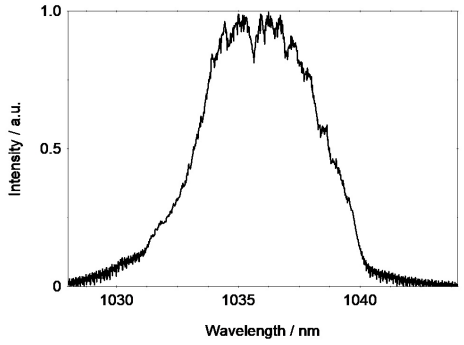

(a) Output pulse spectrum

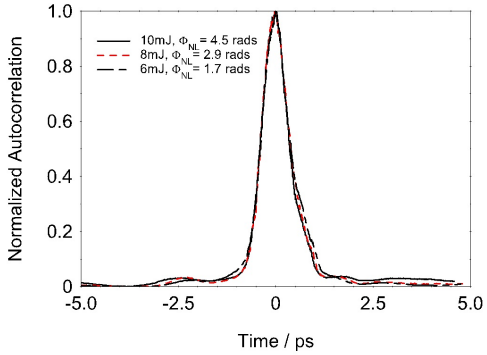

(b) Autocorrelation trace

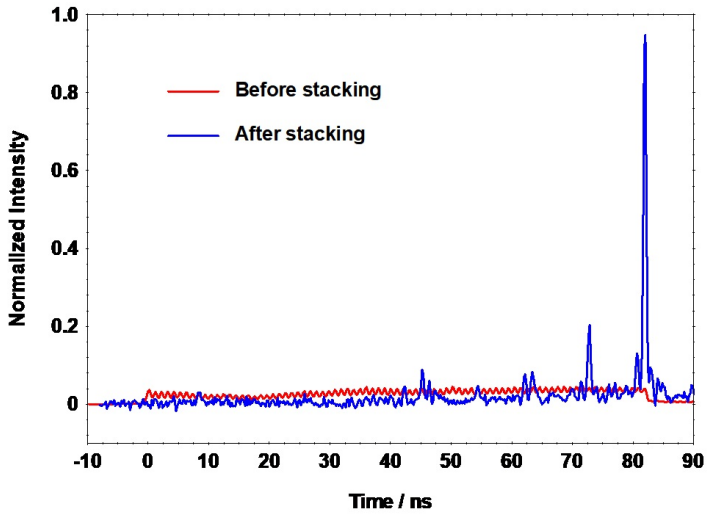

(c) 4+4 GTI stacking of 81 pulses

Figure 4.8: 4+4 GTI Cascade stacking of 81 pulses and autocorrelation.

4+4 multiplexed GTI cavities consisting of 4 sets of 1ns-roundtrip cavities followed by 4 sets of 9-ns roundtrip cavities. While its 7nm spectral bandwidth which corresponds to ∼450fs transform-limited compressed pulse duration, the stacked pulse is compressed to <540fs using diffraction-grating pulse compressor, and the autocorrelation trace is shown in Fig. 4.8.

4.5 Summary

>90% efficient energy extraction from a 1.2m Yb-doped 85 μm core CCC fiber has been achieved using CPSA technique. The 10mJ amplified 81-pulse burst with 4.5 radians of nonlinear phase is compressed to <540fs pulse. CPSA enables generation of multi-mJ femtosecond pulses with one fiber amplifier channel. Ongoing work includes further improvement of stacking fidelity, extending amount of energy extracted out of a single fiber, and implementation of an FPGA-based control system for real-time adjustment of cavity and pulse phases, and pulse-burst amplitude profile.

CHAPTER V

Summary and Future Work

5.1 Summary

To summarize, this dissertation has accomplished the theoretical study and experimental demonstration of coherent pulse stacking amplification in the following three aspects:

1. Long-term stability in coherent pulse stacking amplification. CPSA system phase noise bottlenecks have been identified, characterized and eliminated. Coherent stacking of 81 pulses into a single pulse with high stacking efficiency and robust long-term stability using CPSA technique was demonstrated.

2. High fidelity coherent pulse stacking using high-precision stacking technique and adaptive optimization. Simultaneous active stabilization and adaptive optimization of stacking profile was implemented and achieved using a FPGA-based control system and two-loop SPGD algorithm. Mathematical description of coherent pulse stacking based on transfer matrices and comprehensive theory and model to account for pulse train and cavity alignment errors was established.

3. Energy extraction in a large-core CCC fiber using CPSA technique. Extraction of 90% stored energy at >10mJ level from a large-core CCC fiber amplifier with low nonlinear phase values of 4.5 rads and 540fs compressed pulse duration was achieved.

5.2 Future Work

1. Complete implementation and further automation of high-precision stacking technique. The full stable operation of the CPSA system requires full stabilization of the oscillator to eliminate accumulation of effective piston errors in GTI cavities over time, which is currently the biggest bottleneck towards reaching theoretically possible stacking fidelity. The tilt error elimination in individual GTI cavities is semi-automated with optimizer algorithm at a resolution limit of 10μrad, and its compensation can be fully automated and streamlined with the addition of another PZT-controlled mirror mount in each GTI cavity and beam blockers.

2. Further intelligent system control and optimization. The FPGA-based control system takes over precision work like pulse burst modulation, cavity phase controls, and high-accuracy cavity alignment from human. In the past few years, algorithms and automated processes were continuously developed to steadily replace manual controls. This multi-variable system implementation opens gateway to exciting intelligent algorithms that provides high accuracy, fast convergence and high fidelity end results. While at the moment straightforward optimization algorithms remain the most efficient as compared to some of our collaborated machine learning algorithms efforts, as the system further scales up and pre-pulse contrast detection is implemented, this conclusion might need to be revisited.

3. Coherent temporal combining of spatially combined high energy pulses. Ongoing work on coherent spatial combining of parallel power amplifiers based on large-core CCC fiber shows promising potential for delivering combined pulse burst energy at 10's of mJ energy level, with per channel energy of currently ∼10mJ that can be further scaled up. With the current single channel delivering up to ∼30GW peak power at 10mJ, with spectral and dispersion controls and coherent spatial combining of mJ channels, TW peak power is within reach in a CPSA system.

BIBLIOGRAPHY

BIBLIOGRAPHY

[1] Toshiki Tajima and John M Dawson. Laser electron accelerator. *Physical Review Letters*, 43(4):267, 1979.

[2] Victor Malka, Jérôme Faure, Yann A Gauduel, Erik Lefebvre, Antoine Rousse, and Kim Ta Phuoc. Principles and applications of compact laser–plasma accelerators. *Nature physics*, 4(6):447–453, 2008.

[3] Wim Leemans and Eric Esarey. Laser-driven plasma-wave electron accelerators. *Phys. Today*, 62(3):44–49, 2009.

[4] Sébastien Corde, K Ta Phuoc, Guillaume Lambert, R Fitour, Victor Malka, Antoine Rousse, A Beck, and E Lefebvre. Femtosecond x rays from laser-plasma accelerators. *Reviews of Modern Physics*, 85(1):1, 2013.

[5] RD Edwards, MA Sinclair, TJ Goldsack, K Krushelnick, FN Beg, EL Clark, AE Dangor, Z Najmudin, M Tatarakis, B Walton, et al. Characterization of a gamma-ray source based on a laser-plasma accelerator with applications to radiography. *Applied Physics Letters*, 80(12):2129–2131, 2002.

[6] C Zulick, F Dollar, V Chvykov, J Davis, G Kalinchenko, A Maksimchuk, GM Petrov, A Raymond, AGR Thomas, L Willingale, et al. Energetic neutron beams generated from femtosecond laser plasma interactions. *Applied Physics Letters*, 102(12):124101, 2013.

[7] Hiroyuki Daido, Mamiko Nishiuchi, and Alexander S Pirozhkov. Review of laser-driven ion sources and their applications. *Reports on progress in physics*, 75(5):056401, 2012.

[8] Felicie Albert, Marie-Emmanuelle Couprie, Alexander D Debus, Mike Downer, Jerome Faure, Alessandro Flacco, Leonida A Gizzi, Thomas E Grismayer, Axel Huebl, Chandrashekhar Joshi, et al. 2020 roadmap on plasma accelerators. *New Journal of Physics*, 2020.

[9] John Ruppe, Hanzhang Pei, Morteza Sheikhsofla, Siyun Chen, Russel Wilcox, Wim Leemans, John Nees, and Almantas Galvanauskas. Coherent pulse stacking amplification–extending chirped pulse amplification by orders of magnitude. In *CLEO: Science and Innovations*, pages SM4I–1. Optical Society of America, 2017.

[10] Arno Klenke, Michael Müller, Henning Stark, Marco Kienel, Cesar Jauregui, Andreas Tünnermann, and Jens Limpert. Coherent beam combination of ultrafast fiber lasers. *IEEE Journal of Selected Topics in Quantum Electronics*, 24(5):1–9, 2018.

[11] Henning Stark, Joachim Buldt, Michael Müller, Arno Klenke, Andreas Tünnermann, and Jens Limpert. 23 mj high-power fiber cpa system using electro-optically controlled divided-pulse amplification. *Optics Letters*, 44(22):5529–5532, 2019.

[12] Henning Stark, Michael Müller, Marco Kienel, Arno Klenke, Jens Limpert, and Andreas Tünnermann. Electro-optically controlled divided-pulse amplification. *Optics Express*, 25(12):13494–13503, 2017.

[13] Henrik Tünnermann and Akira Shirakawa. Deep reinforcement learning for coherent beam combining applications. *Optics express*, 27(17):24223–24230, 2019.

[14] Tong Zhou, Qiang Du, Tyler Sano, Russell Wilcox, and Wim Leemans. Two-dimensional combination of eight ultrashort pulsed beams using a diffractive optic pair. *Optics letters*, 43(14):3269–3272, 2018.

[15] Qiang Du, Tong Zhou, Lawrence R Doolittle, Gang Huang, Derun Li, and Russell Wilcox. Deterministic stabilization of eight-way 2d diffractive beam combining using pattern recognition. *Optics letters*, 44(18):4554–4557, 2019.

[16] Ihsan Fsaifes, Louis Daniault, Severine Bellanger, Matthieu Veinhard, Jerome Bourderionnet, Christian Larat, Eric Lallier, Eric Durand, Arnaud Brignon, and Jean-Christophe Chanteloup. Coherent beam combining of 61 femtosecond fiber amplifiers. *Optics Express*, 28(14):20152–20161, 2020.

[17] J Le Dortz, A Heilmann, M Antier, J Bourderionnet, C Larat, I Fsaifes, L Daniault, S Bellanger, C Simon Boisson, J-C Chanteloup, et al. Highly scalable femtosecond coherent beam combining demonstrated with 19 fibers. *Optics Letters*, 42(10):1887–1890, 2017.

[18] Chirped pulse amplification. `https://cuos.engin.umich.edu/researchgroups/hfs/facilities/chirped-pulse-amplification/`.

[19] Donna Strickland and Gerard Mourou. Compression of amplified chirped optical pulses. *Optics communications*, 56(3):219–221, 1985.

[20] Shian Zhou, Frank W Wise, and Dimitre G Ouzounov. Divided-pulse amplification of ultrashort pulses. *Optics letters*, 32(7):871–873, 2007.

[21] R Jason Jones and Jun Ye. Femtosecond pulse amplification by coherent addition in a passive optical cavity. *Optics letters*, 27(20):1848–1850, 2002.

[22] Sven Breitkopf, Stefano Wunderlich, Tino Eidam, Evgeny Shestaev, Simon Holzberger, Thomas Gottschall, Henning Carstens, Andreas Tünnermann, Ioachim Pupeza, and Jens Limpert. Extraction of enhanced, ultrashort laser pulses from a passive 10-mhz stack-and-dump cavity. *Applied Physics B*, 122(12):297, 2016.

[23] Tong Zhou, John Ruppe, Cheng Zhu, I-Ning Hu, John Nees, and Almantas Galvanauskas. Coherent pulse stacking amplification using low-finesse gires-tournois interferometers. *Optics express*, 23(6):7442–7462, 2015.

[24] F Gires and P Tournois. Interferometre utilisable pour la compression dimpulsions lumineuses modulees en frequence. *Comptes Rendus Hebdomadaires Des Seances De L Academie Des Sciences*, 258(25):6112, 1964.

[25] Toshiki Tajima, XQ Yan, and T Ebisuzaki. Wakefield acceleration. *Reviews of Modern Plasma Physics*, 4(7):7, 2020.

[26] Hanzhang Pei, John Ruppe, Siyun Chen, Morteza Sheikhsofla, John Nees, Yawei Yang, Russell Wilcox, Wim Leemans, and Almantas Galvanauskas. 10mj energy extraction from yb-doped 85μm core ccc fiber using coherent pulse stacking amplification of fs pulses. In *Advanced Solid State Lasers*, pages AW4A–4. Optical Society of America, 2017.

[27] Mikhail A Vorontsov. Decoupled stochastic parallel gradient descent optimization for adaptive optics: integrated approach for wave-front sensor information fusion. *JOSA A*, 19(2):356–368, 2002.

[28] John Ruppe. *Theoretical and experimental foundations of coherent pulse stacking amplification*. PhD thesis, The University of Michigan, 2017.

[29] Guoxiang Gu. *Discrete-time linear systems: theory and design with applications*. Springer Science & Business Media, 2012.

[30] Yifan Cui, Hanzhang Pei, John Nees, and Almantas Galvanauskas. Mode-locked oscillator phase stabilization using a gires-tournois interferometer. In *Advanced Solid State Lasers*, pages AM6A–15. Optical Society of America, 2018.

[31] Gregory D Goodno, Chun-Ching Shih, and Joshua E Rothenberg. Perturbative analysis of coherent combining efficiency with mismatched lasers. *Optics express*, 18(24):25403–25414, 2010.

[32] `https://stanford.edu/~shervine/teaching/cs-230/`.

[33] Chen Li, Yuxuan Ma, Xiang Gao, Fuzeng Niu, Tongxiao Jiang, Aimin Wang, and Zhigang Zhang. 1 ghz repetition rate femtosecond yb: fiber laser for direct generation of carrier-envelope offset frequency. *Applied optics*, 54(28):8350–8353, 2015.

[34] Yilun Xu, Russell Wilcox, John Byrd, Lawrence Doolittle, Qiang Du, Gang Huang, Yawei Yang, Tong Zhou, Wim Leemans, Almantas Galvanauskas, et al. Fpga-based optical cavity phase stabilization for coherent pulse stacking. *IEEE Journal of Quantum Electronics*, 54(1):1–11, 2017.

[35] Xiuquan Ma, Cheng Zhu, I-Ning Hu, Alex Kaplan, and Almantas Galvanauskas. Single-mode chirally-coupled-core fibers with larger than 50μm diameter cores. *Optics express*, 22(8):9206–9219, 2014.

[36] Cheng Zhu. *High Power Chirally-Couple-Core (CCC) Fiber Lasers for Coherent Combining Systems.* PhD thesis, The University of Michigan, 2014.

[37] Hanzhang Pei, John Ruppe, Siyun Chen, Morteza Sheikhsofla, John Nees, Yawei Yang, Russell Wilcox, Wim Leemans, and Almantas Galvanauskas. Near-complete stored energy extraction from fiber amplifiers in ultrashort¿ 10mj energy pulses using coherent pulse stacking amplification (conference presentation). In *Fiber Lasers XV: Technology and Systems*, volume 10512, page 1051209. International Society for Optics and Photonics, 2018.